A Study of Thermal and Nonthermal X-ray Structures in the Galactic Center Region

Atsushi Senda

Department of Physics, Graduate School of Science, Kyoto University
Kitashirakawa-Oiwake-cho, Sakyo-ku, Kyoto, 606-8502, Japan
senda@cr.scphys.kyoto-u.ac.jp

Reprinted from the doctoral thesis submitted to
the Department of Physics, Graduate School of Science,
Kyoto University
on January 5, 2005
in partial fulfillment of the requirements
for the degree of Doctor of Philosophy in physics.

Abstract

We present the result of an X-ray observational study of small scale structures in the central region of our galaxy. From the region, we resolved two discrete thermal X-ray structures (G0.570−0.018 and G359.8−0.3) and tenth of nonthermal X-ray structures for the first time mainly using *Chandra* X-ray Observatory.

G0.570−0.018 is a thermal source characterized by extraordinary high temperature ($kT \sim 6$ keV) and shell-like morphology with a small diameter (less than 1 pc at the 8.0 kpc). The observed ionization parameter suggests the X-ray emitting plasma is far from collisional ionization equilibrium. These unusual physical conditions are well understood if G0.570−0.018 is an extremely young supernova remnant (SNR) before reaching adiabatic expansion phase (Sedov phase). G359.8−0.3 is a nonthermal radio shell located at the ~ 30 pc south of the Galactic center. We successfully detected the thermal X-rays from the central region of the shell for the first time. X-ray spectrum of G359.8−0.3 obtained with *Chandra* and *XMM-Newton* exhibits strong line emissions from Si, S, Ar, and Ca. The physical properties deduced from observable parameters are consistent with the interpretation that G359.8−0.3 is middle-aged ($t \sim 10^4$ year) SNR. Furthermore, we revealed that the nature of G359.8−0.3 can be well explained in the framework of the "mixed-morphology" SNR.

In addition to these thermal structures, we discovered a number of nonthermal X-ray features within the central 40 pc $\times$ 40 pc region of the galaxy using archival data of *Chandra*. The series of *Chandra* data consists of 12 pointings and total effective exposure is ~ 600 ksec, which provides us with the finest quality of X-ray spatial information of the Galactic center(GC) so far. Eight of the discovered nonthermal X-ray structures exhibit knot-like features with characteristic scales similar to each other. In particular, radio counterparts are found to be associated with at least two of them. Moreover, we also found two rim-like nonthermal structures in the southeast region of the Galactic nucleus and a nonthermal clump embedded with the 6.4-keV clump in the north region. Photon indices of these nonthermal structures are determined to $\Gamma \sim 2$ or harder values. In the case of synchrotron emission, due to the extreme short lifetime (1–10 yr) of synchrotron X-rays under the strong magnetic field ($B \sim 1$ mG) of the GC, continuous energy injection by high energy particles is required to maintain the observed nonthermal structures. In other words, These X-ray knots should be the trace of the cosmic-ray accelerators at the GC. While other possible emission mechanism,

i.e. inverse Compton scattering or nonthermal bremsstrahlung, cannot be excluded as their origin so far.

Among them, the most outstanding features are the three X-ray knots which seem to be aligned on a straight line from Sgr A* to northwest direction. The X-ray properties of the knots indicate their origin is associated with high energy activities of Sgr A* in the recent past. These results are not only the discovery of the nonthermal structure closest to the Galactic nucleus ($d < 1$ pc), but also have a possibility of the first detection of jets ejected from the nearest super massive black hole.

Contents

List of Figures

List of Tables

Chapter 1

Introduction

As we all know, there are countless galaxies in the universe. Also as we know, our solar system belongs to one of them; the Milky Way Galaxy, hence the center of our Galaxy (abbreviated to the Galactic center, or the GC, afterward) is the closest center of all the galaxies. For example, the Galactic center is about one hundred times closer to us than the nearest spiral galaxy (M31; Andromeda Galaxy) and more than a thousand times closer than the nearest Active Galactic Nucleus (NGC 1068). In spite of its vicinity, we had not been able to know much about the GC for the long years, because of the heavy optical extinction of the interstellar medium which lie between the Solar system and the GC. Assuming the distance from us to the GC is 8.0 kpc (McNamara et al., 2000) and averaged number density of the galactic plane is 1 cm^{-3}, hydrogen column density from the GC to us is amount to 5×10^{22} cm^{-2}. Therefore, as is shown in Figure 1.1, we can see through the GC region with limited energy band; below $\lambda \simeq 2$ μm (radio and near-infrared) and above $E \simeq 2$ keV (hard X-ray and Gamma-ray).

Radio observations opened up the first window to see the GC region, In 1933, C. G. Jansky detected the first cosmic (extra-solar) radio emission and discovered that its intensity is increased toward the Galactic center (Jansky, 1933). In 1950's, the GC is identified as the radio source and named Sgr A (Piddington & Minnett, 1951; McGee & Bolton, 1954), which is the strongest radio emitting source in the whole sky. Until now, numerous higher spatial/spectral resolution radio observations have been performed. They have revealed that complex features are highly concentrated on a few hundred parsecs of the GC region.

Then near-infrared and X-ray observations have found a number of sources which may have possible relation to high energy activities of the GC region. In particular,

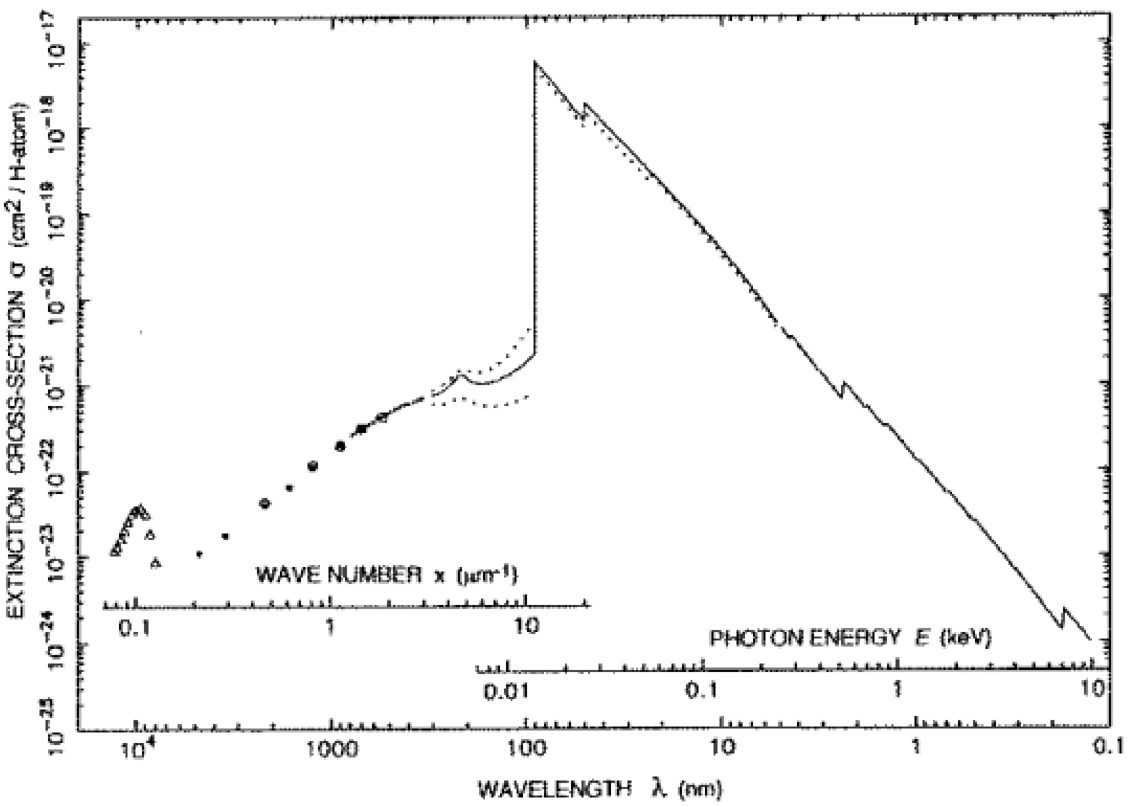

Figure 1.1: The extinction (absorption plus scattering) cross section by interstellar medium from the infrared (10 μm) to hard X-ray (0.1 nm) band (Ryter, 1996).

the Galactic nucleus (Sgr A*) must play a crucial role for the high energy activities of the GC. As will be mentioned in Chapter 2, many observational results have been accumulated to confirm that Sgr A* is a super massive black hole over this twenty years. With Near-infrared high-resolution observations, proper motions of near-infrared stars in the immediate vicinity ($\simeq$ 30 light days) of Sgr A* were successfully detected(Schödel et al., 2002). According to the recent measurement of Ghez et al. (2005), the shape of their Keplerian orbits indicates that $\sim 3.7\ (\pm\ 0.2) \times 10^6\ M_\odot$ is concentrated within the 45 AU at the position of Sgr A*. Recent high-resolution X-ray observations succeeded in detecting point-like X-ray emission at the position of Sgr A*. However, its X-ray luminosity is far dimmer than that expected from its enclosed mass (Eddington luminosity) by $10-12$ orders of magnitude (Baganoff et al., 2001; Goldwurm et al., 2003; Porquet et al., 2003).

On the other hand, strong 6.4-keV line emissions have been detected from giant molecular clouds near the GC. The most plausible explanation for the 6.4-keV line nature is provided by the X-ray reflection nebulae (XRNe) model: X-rays from past activities of Sgr A* have been irradiating the nearby GMCs and they are now emitting fluorescence of neutral iron and reflected X-rays (Koyama et al., 1996; Murakami et al., 2000, 2001a,b). The XRN model also suggest that Sgr A* is as luminous as 10^{39} ergs s^{-1} about 300 years hundred years ago. Thus, the nucleus of our Galaxy is far from static, but exhibits dynamic characteristic with closely interacting with nearby environment. These 6.4-keV features are not observed in the Galactic plane or bulge, but unique to the GC, hence the origin of the neutral iron line must have a close relation with the Galactic nucleus and/or its vicinities.

Another enigmatic feature within the central hundred parsecs region is a large scale diffuse X-ray emission, discovered with *Ginga* (Koyama et al., 1989; Yamauchi et al., 1990) and *ASCA* (Koyama et al., 1996). Assuming that the extended X-ray emission is thermal origin, the electron temperature is as high as $kT \sim 10$ keV and their total thermal energy should be up to $E_{\rm th} \sim 10^{54}$ ergs. The huge energy corresponds with explosion energy of 10^3 Supernovae. From the time scale of the diffuse hot plasma ((5–10) $\times\ 10^4$ year), the rate of SN must be 1 event / 50–100 year. However, such a large number of supernova remnants have not been found in the GC region so far. An alternative explanation is that some energetic explosion(s) of Sgr A* generate diffuse hot gas in the GC. In this case, some gradient of electron temperature and ionization parameter should be observed as a function of distance from the Sgr A*, however, we have not obtained such indications so far. Thus, its origin remains an open issue over the decade.

In contrast with the large thermal structures, a number of nonthermal radio emissions from linear filaments have been detected around the Galactic center (Yusef-Zadeh et al., 1984; Yusef-Zadeh & Barry, J., 1989; Morris, 1994; LaRosa et al., 2000, 2004). Their spatial distribution seems localized within only central hundred parsecs. Their emission must be originated from synchrotron radiation from high energy particles. Thus, these feature lead us to suspect that the Galactic center holds particle accelerators. In addition, it also suggests that the magnetic field strength around the GC is extremely strong ($B \sim 1$ mG) inferred from the extreme linearity of these filaments. Recently, the discovery of non-thermal X-ray filaments (NTXFs) has been reported with *Chandra* and *XMM-Newton* observations (Wang et al., 2002; Sakano et al., 2003; Lu et al., 2003), while their origins and connection of radio filaments are still unclear.

The origin of cosmic-ray is a long standing problem which has possible relation with the high energy activity of the Galactic center. This serious issue has been unsolved over a century since the discovery of cosmic-rays (Hess, 1911, 1912). Recently, X-ray and TeV Gamma-ray observations have found robust evidence that shock fronts of several young supernova remnants accelerate particles. So far, supernova shock fronts are the first and the only case that a site of cosmic-ray acceleration is spatially identified (e.g., SN1006 (Koyama et al., 1995; Tanimori et al., 1998), RX J1713.7−3946 (Koyama et al. , 1997; Enomoto et al., 2002) and RCW 86 (Bamba et al., 2000a; Borkowski et al., 2001a)). On the other hand, The cosmic-ray spectrum has a significant break at the energy of $\sim 10^{15.5}$ eV, so called "knee energy". The origin of cosmic rays under the knee energy, at least, is thought to be Galactic, because an average magnetic field strength of a galaxy is sufficient to confine them. It is no doubt that the GC region has the deepest gravitational potential field in the Galaxy, hence we suspect that the GC harbors the highest cosmic-ray accelerator in our Galaxy.

The objective of this thesis is to unveil the origin of high energy activities in the GC region. More specific, to answer questions as shown below;

- What injects the huge energy to the large scale X-ray diffuse emission; multiple

supernovae occurred within the recent past or the energetic explosion(s) of the central massive black hole ?
- What is the origin of the radio/X-ray nonthermal structures ?
- Is the Galactic center region the site of cosmic-ray acceleration ?
To give answers to these long standing problems, we think it is the best strategy to focus attention on the X-ray diffuse structures resolved high spatial resolution observations. Hard X-ray observation is essential for tracing high energy activities of the Galactic center in the following reasons;
- An X-ray photon energy is higher than that of radio and infrared by an order of 6−9.
- Recent technical advance can enable us to carry out high resolution X-ray imaging ($\Delta\theta \sim 0.5''$) and spectral ($E/\Delta E \sim 50$) study.
- At the GC, only hard X-ray band can cover both thermal emission from the hot gas and nonthermal emission from the high energy particles.
Thermal structures may be relics of some heating process occurred in the past hundreds-thousands years. On the other hand, the nonthermal X-ray structures can be the direct evidence for the cosmic-ray accelerations. Hence we used archival data of *Chandra* in main and performed systematical search for thermal and nonthermal X-ray structures near the GC region.

The road map of this thesis is as follows. In Chapter 2, We at first review the GC sources which have close relation with high energy activities at the Galactic center. Chapter 3 is devoted to summarize the basic characteristics of science instruments of *Chandra* X-ray Observatory. In Chapter 4, we present the results of X-ray analyses of thermal features which we discovered in the Galactic center region; G0.570−0.018 and G359.8−0.3. The origins of these sources are also discussed in the chapter. In Chapter 5, We present the data analyses of the deepest exposure observations of *Chandra*. Then we report the discovery and the X-ray properties of nonthermal X-ray features. In Chapter 6, possible relations between thermal/nonthermal features and high energy activities of the GC as well as the nature of the nonthermal structures are discussed. Finally, we briefly summarize our work in Chapter 7.

Chapter 2

Review : The Center of our Galaxy

Since too many components are concentrated within the deep gravitational potential of the Milky Way; central massive black hole, HII regions, massive star clusters, supernova remnants, cold molecular clouds, diffuse hot gas, nonthermal sources, and etc, we cannot cover all of these features in the limited space. Fortunately, we can find several good reviews about the past study of GC region (Mezger et al., 1996; Morris & Serabyn, 1996). Therefore, in this chapter, we briefly review the selected sources/structures which are thought to be closely related to our work.

2.1 Sgr A*: The Nucleus of our Galaxy

Many galaxies are thought to harbor super massive black holes ($M_{\rm BH} \geq 10^6\ M_\odot$) at their dynamical centers. Sgr A* is not only the nearest galactic nucleus, but the highest probable super massive black hole candidate. Note that detailed reviews of Sgr A* are provided by Genzel et al. (1994) and Melia & Falke (2001), hence here we give a brief summary for the past results and mention in details only for recent observational results.

2.1.1 Discovery of Sgr A*

Sgr A* was discovered by Balick & Brown (1974) as a bright (brightness temperature $\geq 10^7$ K), compact ($\theta \leq 0.''1$) radio source. A position of the source is in the direction of the inner 1 pc core of a dynamical center of our Galaxy. Ever since Sgr A* has been the primary candidate for the nucleus of our Galaxy. In fact, radio luminosity of Sgr A*($\sim 10^{34}$ ergs s^{-1}) is within range with the nuclear radio sources of other nearby normal galaxies such as M31.

2.1.2 Evidence for a super massive black hole

A strong evidence for mass concentration at the position of Sgr A* has been provided by proper motion measurements of nearby stars. According to Eckart & Genzel (1997) and Ghez et al. (1998), stellar speeds in excess of 1000 km s^{-1} at a distance of 0.015 pc from Sgr A* indicate a central dark mass of $\sim 2.6 \times 10^6\ M_\odot$ confined to a volume of at most 10^{-6} pc^{-3} . The huge mass concentration within such a compact region is consistent with a model that Sgr A* is associated with a super massive black hole. Its non-thermal radio spectrum(Serabyn et al., 1997) and extremely slow proper motion(Backer & Sramek, 1999; Reid et al., 1999) also support the model.

Recently, Schödel et al. (2002) reported a result of high-resolution near-infrared observations which have been tracing a proper motion of the closest star (named S2) around Sgr A* for about 10 years. The positional data of S2 trace two-thirds of a closed elliptical orbit and robustly explained by the Keplerian orbit around a central point mass located at the position of Sgr A*(Figure 2.1). An orbital period and a pericenter distance of S2 are determined to be 15.2 years and 17 light hours ($\sim$ 124 AU), respectively. This proper motion measurement strictly constrains a mass distribution of Sgr A*. As shown in Figure 2.2, pericenter data of S2 probes the mass concentration within 2100 times schwarzshild radius of $3 \times 10^6\ M_\odot$ black hole. The best fit mass distribution model for all observational data shown in Figure 2.1 is that $(2.6 \pm 0.2) \times 10^6\ M_\odot$ point-like mass plus a stellar cluster of central density $3.9 \times 10^6\ M_\odot$ pc^{-3} (solid curve in Figure 2.2).

At the stage, alternative models which have been previously discussed (dense cluster of dark stellar objects or massive degenerate fermion ball) are excluded for the mass origin of Sgr A*.

2.1.3 X-ray observations of Sgr A*

Poor spatial resolution had prevented us from estimating an intrinsic X-ray luminosity of Sgr A* for a long time. In 1990's, *ASCA* achieved a hard X-ray imaging spectroscopy with moderate spatial resolution ($\theta \sim 3'$) for the first time. However, no clear X-ray counterpart can be found with *ASCA*, because of a serious contamination from nearby variable hard X-ray source AX J1745.6−2901, which was turned out to be a low mass

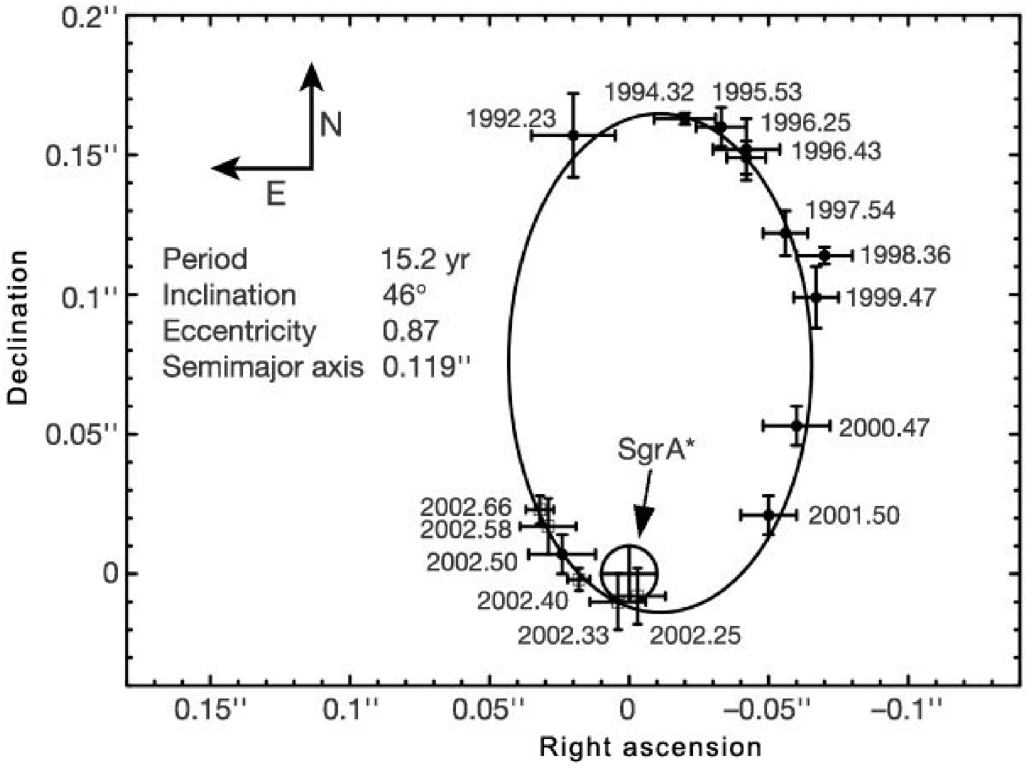

Figure 2.1: Orbit of nearby star (S2) around Sgr A* for about 10 years. Data points between 1992-2001 and 2001.50 are obtained with SHARP camera on the ESO NTT, while 2002.25, 2002.33, 2002.40, 2002.58 and 2002.66 are with CONICA/NAOS on the ESO VLT (Schödel et al., 2002).

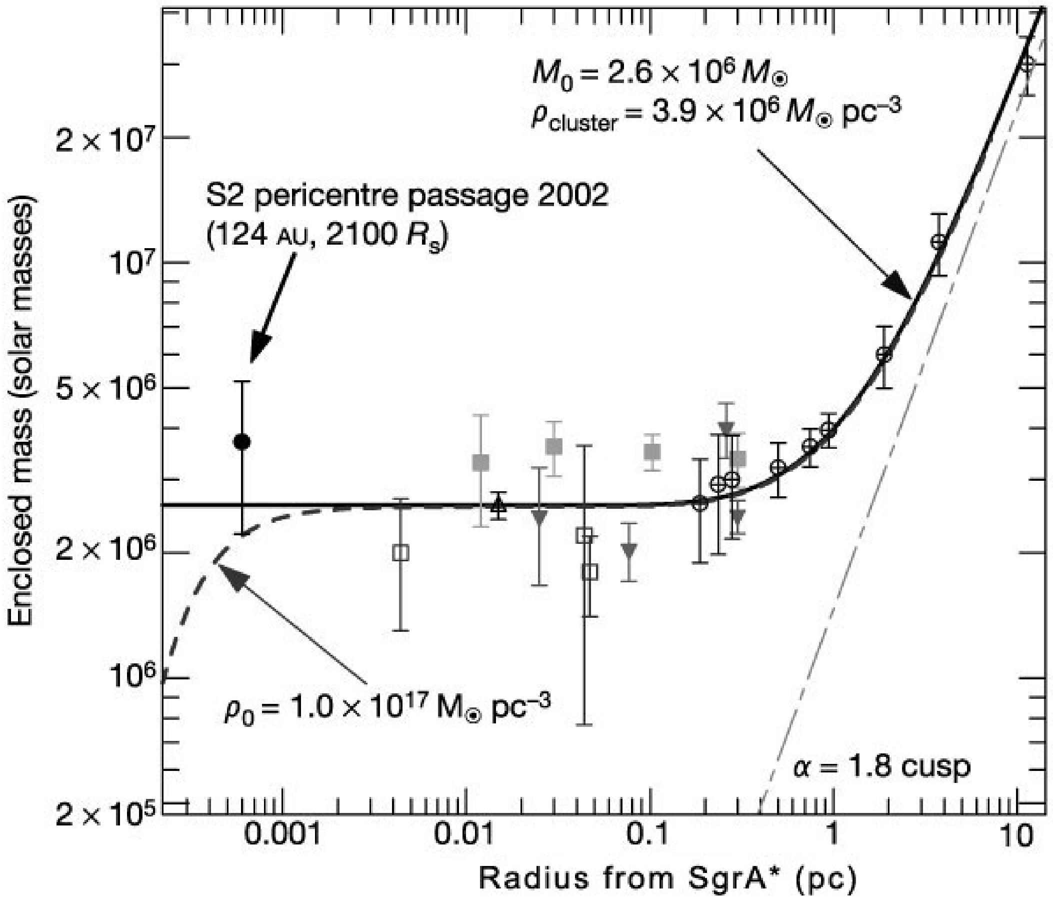

Figure 2.2: Enclosed mass as a function of projected distance from Sgr A* Schödel et al. (2002). An upward-pointing rectangle obtained from proper motions observed Keck Observatory Ghez et al. (1998). Gray filled rectangles and open circles are mass estimates by Genzel et al. (2000). Open rectangles is taken from a result of Chandran (2001).

X-ray binary located at $\sim 1.'5$ southwest of the position of Sgr A* (Maeda et al., 1996). An upper limit of an X-ray luminosity of Sgr A* inferred from *ASCA* observations is 3×10^{35} ergs s^{-1} in 2−10 keV band (Maeda, 1998; Sakano et al., 2002). This value is consistent with the result of a *Beppo-SAX* measurement Sidoli & Mereghetti (1999).

After 2000, thanks to an excellent angular resolution of *Chandra*, an X-ray source was resolved at the position of Sgr A* for the first time(Baganoff et al., 2003). A coincidence between the X-ray source and the radio position of Sgr A* is within $0.''27$ (Figure 2.3).

In addition, X-ray flaring events from Sgr A* have been recently reported with *Chandra* (Baganoff et al., 2001) and *XMM-Newton* (Goldwurm et al., 2003; Porquet et al., 2003). Figure 2.4 shows a light curve of the first detected X-ray flare of Sgr A* (Baganoff et al., 2001). Although some differences exist between these flares, they seem to share basic properties; flare duration time-scales (10^3-10^4 sec) and luminosity ratios of a flaring state to a quiescent ($\sim$ 50−150). These X-ray features support the idea that Sgr A* is associate with a super massive black hole.

2.1.4 Emission mechanism of Sgr A*

A bolometric luminosity of Sgr A* is below 3×10^{-8} of its corresponding Eddington Luminosity of 3.4×10^{44} ergs s^{-1} (e.g. Melia & Falke (2001)), which is far fainter than those of typical extra-galactic AGNs. Moreover, An X-ray luminosity of Sgr A* is estimated to $\sim 2.4 \times 10^{33}$ ergs s^{-1} (2−10 keV) in a quiescent state (Baganoff et al., 2003) or $\sim 2.4 \times 10^{35}$ ergs s^{-1} even in the brightest flaring state so far detected (Porquet et al., 2003). These X-ray luminosities are fainter than its Eddington luminosity by about 9−11 orders of magnitude.

The weakness of emission from Sgr A* requires a lack of accretion matter, radiative inefficient accretion flow, or some other mechanisms. Various models of radiation mechanisms have been proposed to explain the spectral energy distribution (SED) of Sgr A* on the basis of radiative inefficient accretion flows (RIAFs); Bondi-Hoyle flows (Melia, 1992; Melia & Falke, 2001), advection dominated accretion flows (Narayan et al., 1996), RIAFs with non-thermal electrons(Yuan et al., 2003), etc.

On the other hand, alternative models have been proposed. They are constructed from the standpoint that not only accretion flows, but also outflows (such as a jet) play a significant part in the observed emission (Falke & Markoff, 2000), such as Jet-RIAF model (Yuan et al., 2002).

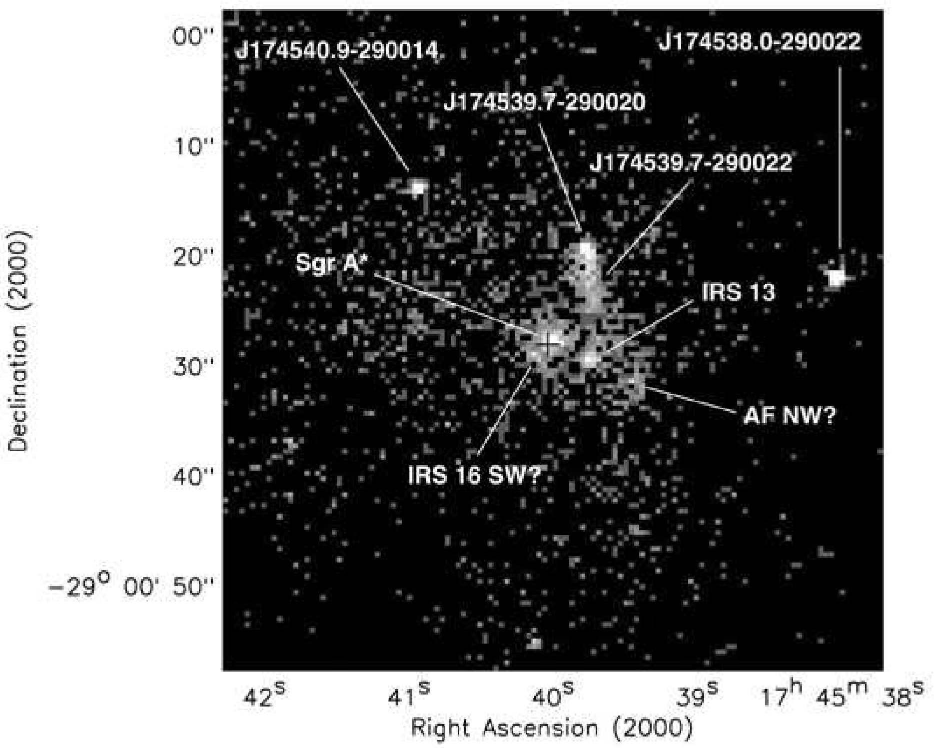

Figure 2.3: *Chandra* ACIS view of the central 1′× 1′ region of our Galaxy (Baganoff et al., 2003). Energy band is 0.5−7 keV. The black cross represents the radio position of Sgr A* determined by Reid et al. (1999).

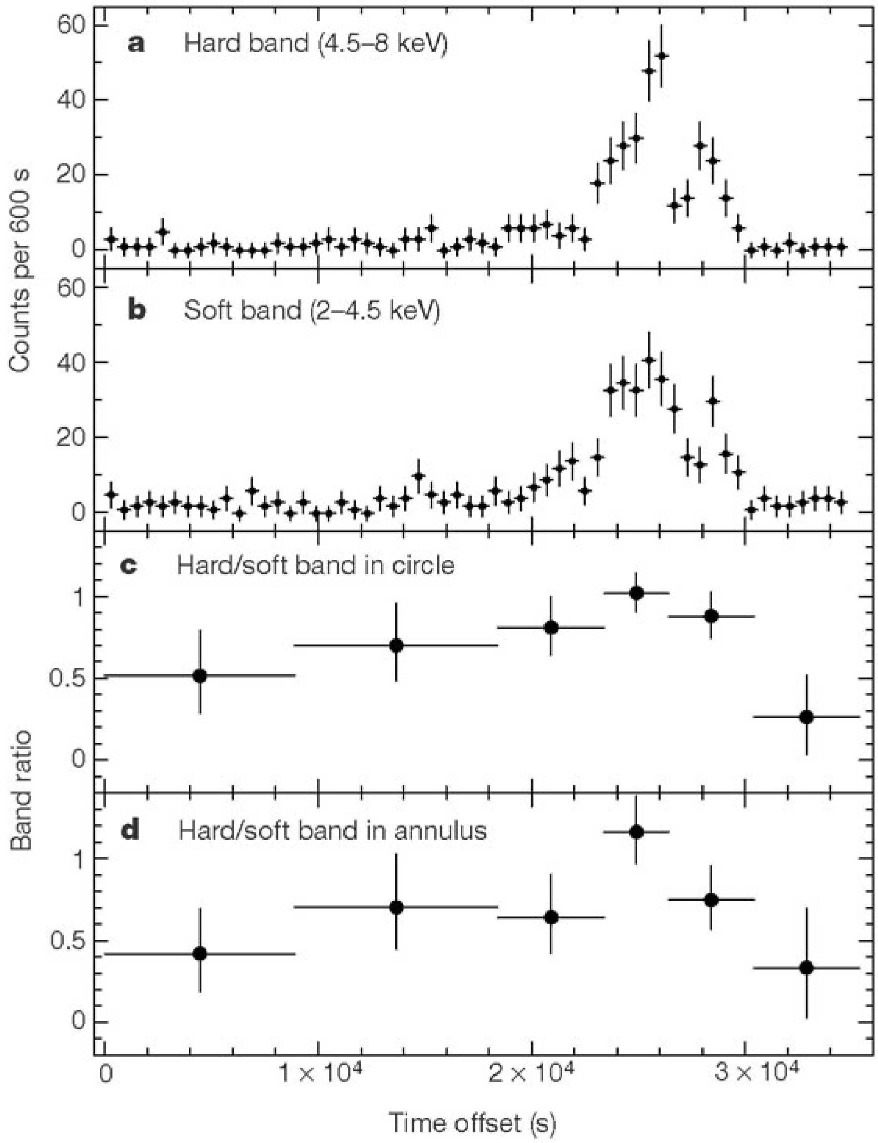

Figure 2.4: Upper two panels: Hard(a) and soft(b) band light curves of the X-ray flare obtained with *Chandra* ACIS on 26−27 October 2000. Both plots are constructed from counts accumulated within a radius of 1.″5 of Sgr A*. Lower two panels: Hard/soft band ratio within annulus of inner and outer radii 0.5″(c) and 2.5″(d). (Baganoff et al., 2001)

2.2 X-ray Diffuse Emission from the GC

2.2.1 Large scale hot plasma

The first X-rays from inner few degrees of the GC were discovered with *UHURU* satellite (Kellogg et al., 1971). However, the specific X-ray feature of the Galactic center region have not been debatable before 1980's because of technical difficulties of the hard X-ray imaging and spectroscopy. With *Ginga* satellite, Koyama et al. (1989) discovered diffuse X-rays with a strong iron line from an extended region near the Galactic Center. The total thermal energy is $\sim 10^{54}$ ergs with an electron temperature of $kT \sim 10$ keV.

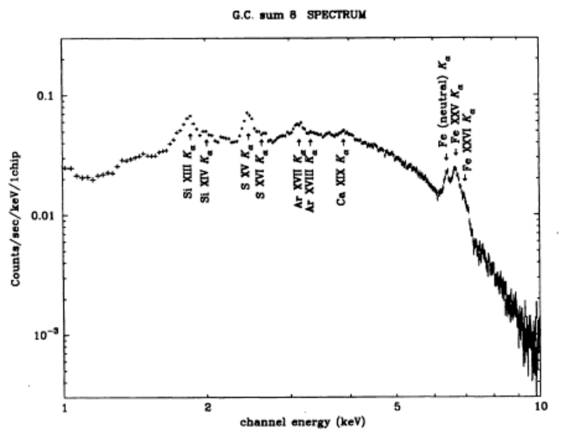

Figure 2.5: Spectrum of the diffuse emission from $1° \times 1°$ region of the GC obtained with *ASCA*. (Koyama et al., 1996).

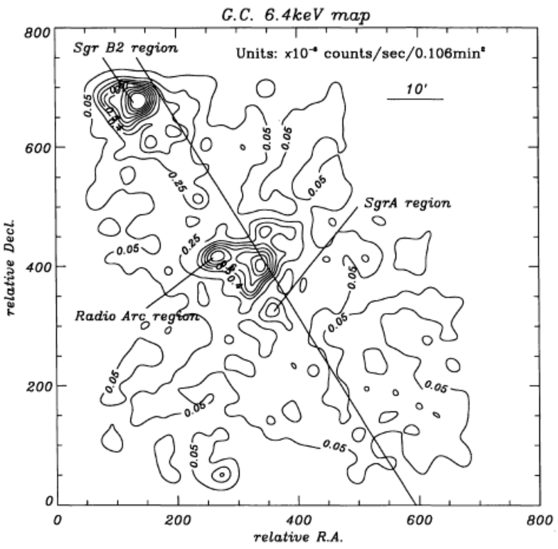

Figure 2.6: Surface brightness map of the 6.4-keV line emission. (Koyama et al., 1996).

The *ASCA* observations confirmed the *Ginga* result and revealed more detailed structures in the GC region (Koyama et al., 1996). As shown in Figure 2.5, The strong iron line in a $\sim 1° \times 1°$ region was resolved into [three lines at 6.9, 6.7, and 6.4 keV, which are attributable to H, He-like, and neutral irons, respectively. The former two are due to high temperature plasma, while the latter indicates the presence of cold gas in a strong X-ray field. The intensities of 6.9 and 6.7 keV lines suggest that the the plasma temperature is a few–10 keV, roughly consistent with *Ginga* result. Since such a high-temperature plasma cannot be bounded by the Galactic gravity, the plasma will expand. It takes 5×10^4 year for the X-ray emitting plasma to expand observed size ($\sim$ 80 pc) with the sound speed of 10 keV ($\sim$ 1600 km s^{-1}). This time-scale may be considered to be the age of the plasma. The total thermal energy equivalent with explosion energy of 10^3 supernovae. These huge energy and short escape time lead us to suspect that the Galactic center has experienced energetic explosion(s) of Sgr A* or multiple supernovae within the past 5 $\times$ 10^4 years. *Chandra* observation resolved a number of point sources were resolved in the GC region with its excellent spatial resolution, however, the contribution of the resolved point sources is less than 10 % of total Galactic center X-ray emission (Wang et al., 2002; Muno et al., 2003). Hence, the origin of the X-ray diffuse emission is still an open issue.

2.2.2 6.4-keV emission from giant molecular clouds

The "X-ray quiet" Sgr A* is in sharp contrast to the surrounding high temperature plasma represented by strong 6.9 and 6.7 keV line emissions. The 6.4-keV line emission can be a clue to connect the quiet Sgr A* and its violent surroundings. *ASCA* found that the 6.7-keV and 6.9-keV emission is uniformly distributed, while the 6.4-keV emission is not. As shown in Figure 2.6, the brightest regions are spatially coincident with the position of "Sgr B2 region" and "Radio Arc region", both are known to be the site of giant molecular clouds (GMCs). They both located in the positive galactic longitude. On the other hand, strong 6.4-keV emission has also found from Sgr C with *ASCA* (Murakami et al., 2001a), which is GMC located in the negative Galactic longitude, where the allmost mirror position of Sgr B2 with reference to the Galactic nucleus (Sgr A*).

Chandra has made it possible to study quantitatively the X-ray spectra and morphologies of these cold molecular clouds. Murakami et al. (2001b) revealed that diffuse X-rays from the Sgr B2 have a concave shape pointing to the GC direction as shown in Figure 2.7, then confirmed that the X-ray characteristics of Sgr B2 can well be explained by the "X-ray Reflection Nebula (XRN)" model; strong external X-rays from the GC direction hit a cold molecular cloud, then it reflects Thomson scattering X-rays and emit 6.4-keV line emissions via photo-electric absorption and fluorescence by cold (neutral) iron atoms (Figure 2.8).

One problem is that we can find no external X-ray source which is strong enough to explain the 6.4-keV from the XRNe. To explain the luminosity of Sgr B2 cloud, required luminosity of an irradiating source is $\sim 10^{39}$ ergs s^{-1}, which is larger than Eddinton luminosity of a neutron star. The most plausible scenario is that Sgr A* is

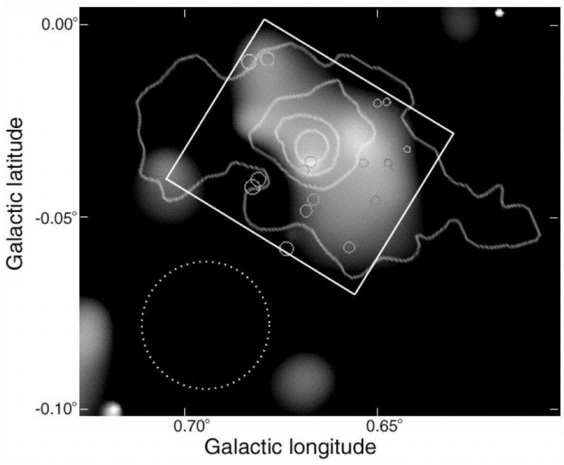

Figure 2.7: Adaptively smoothed X-ray image of Sgr B2 cloud with *Chandra* ACIS-I. Overlaid contours indicate ^{13}CO line flux. The positions of the resolved point sources are shown by small circles (Murakami et al., 2001b).

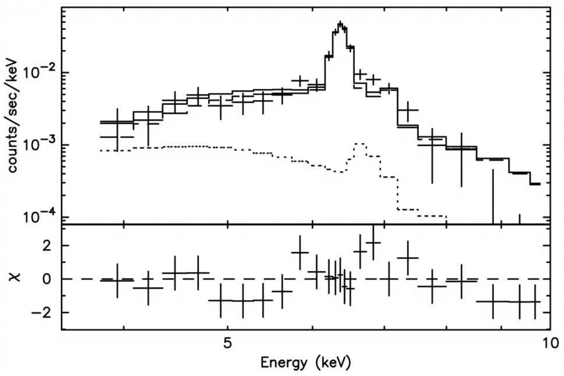

Figure 2.8: X-ray spectrum of Sgr B2 cloud. The source and background regions are shown in the rectangle and the dotted circle in Figure 2.7, respectively. Dashed line indicates the contribution of all the resolved point sources (Murakami et al., 2001b).

faint at present but was bright in the past equivalent with light traveling time from Sgr A* to each XRN. In this case, we are observing delayed X-rays, traveling extra distance from Sgr A* to the molecular clouds. Taking projected distance to the each XRNe into account, Sgr A* must be as bright as 10^{39} ergs s^{-1} until recent past of 100–300 years (Murakami et al., 2001b).

2.3 Sgr A East

Sgr A East is a bright, nonthermal, shell-like structure with a scale of $3.5' \times 2.5'$ just at the Galactic center (Ekers et al., 1975). As shown in Figure 2.9 and 2.10, in projection, Sgr A East include the radio structure Sgr A West, which contains the nonthermal point source Sgr A* and a three-arm spiral structure called the "mini spiral" which is thought to be orbit around Sgr A*. Although the center of the Sgr A East radio shell is offsetted from the position of Sgr A* and Sgr A West by about $\sim 50''$, a number of observations suggest that Sgr A* and Sgr A West is physically located very near or possibly embedded with Sgr A East (Yusef-Zadeh, 2000).

The radio morphological and spectral properties of Sgr A East can be explained in the context of SNR (Jones, 1974; Ekers et al., 1983). However, the proximity of Sgr

A East and Sgr A* evoke alternative interpretation of the origin; e.g. the remnant of an energetic explosion triggered by some gravitational interactions occurred in Sgr A* (Yusef-Zadeh & Morris, 1987a; Khokhlov & Melia, 1996).

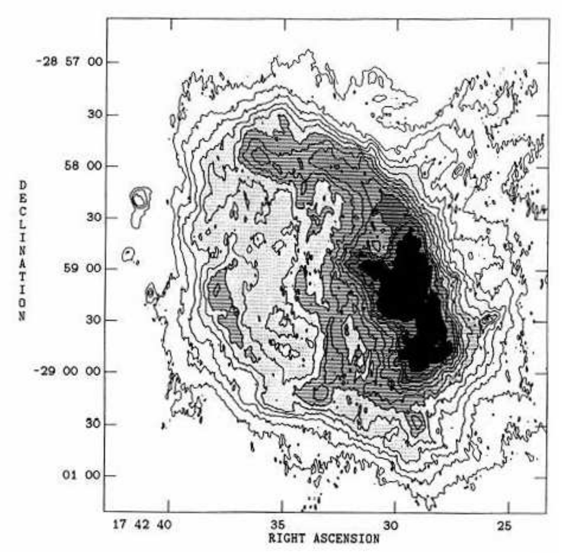

Figure 2.9: VLA 20 cm image of Sgr A complex with 1.3″ × 2.5″ resolution (Pedlar et al., 1989).

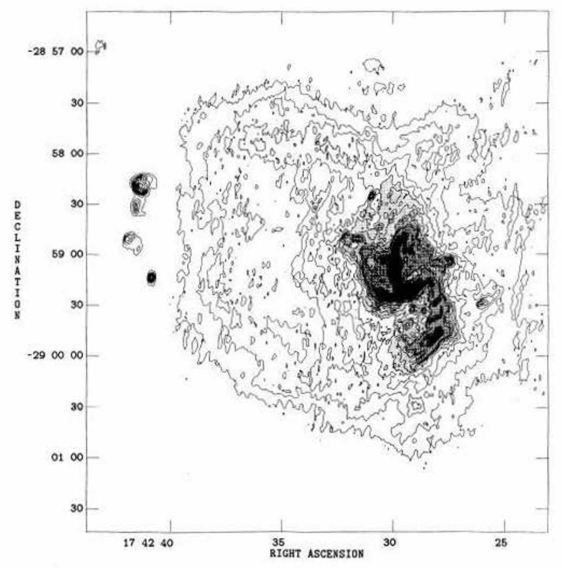

Figure 2.10: Same region of Figure 2.9 viewed with VLA 6 cm. Spatial resolution is 1.3″ × 2.5″ (Pedlar et al., 1989).

With the hard X-ray (2−10 keV) observation of *ASCA*, Koyama et al. (1996) remarked on an extended emission of 2′× 3′ oval-shaped region around Sgr A*. The surface brightness of the X-ray enhancement is higher than surrounding diffuse X-ray emission by a factor of about five.

With *Chandra* observation, Maeda et al. (2002) resolved diffuse X-rays which is clearly associated with Sgr A East from the other complex structures in the region for the first time. The X-ray emission from Sgr A East fills central ~ 2 pc of the nonthermal radio shell. Its X-ray spectrum exhibits strong Kα lines from highly ionized S, Ar, Ca, and Fe, which can be well reproduced by a thin thermal plasma model (MEKA) with an electron temperature and metal abundance of $kT_{\rm e} \sim 2$ keV and $Z \sim 4$ solar. From an emission measure, total mass of X-ray emitting gas is estimated to be $\sim 2\ \eta^{1/2} M_{\odot}$. The overabundance of heavy elements and the total gas mass support the hypothesis that Sgr A East is a remnant of single supernova, perhaps Type II SN of a 13−20 $M_\odot$ progenitor star.

The recent result of *XMM-Newton* observation implies multi-temperature thin thermal plasmas are coexist in Sgr A East, which can be approximated with two temperature components of 1 keV + 4 keV (Sakano et al., 2004). They also discovered a spatial distribution of metal abundances. The iron abundance Sgr A East is as high as $Z_{\mathrm{Fe}} \sim 4$ solar at the core region, while sub-solar at the outer region. On the other hand, the abundance of lighter elements (S, Ar, and Ca) stay at 1−3 solar at the entire region. Their interpretation for the origin of Sgr A East is a Type I SN or a Type II SN of relatively small progenitor mass, which is consistent in principle with the above *Chandra* result (Maeda et al., 2002).

2.4 Nonthermal Radio Structures

2.4.1 The Galactic Center Radio Arc (GCRA)

The Galactic Center Radio Arc (GCRA), discovered by Yusef-Zadeh et al. (1984) toward the ~ 50 pc ($= 20'$) northeast direction from the Galactic center, is one of the most distinguished radio structure in the central hundred parsecs of the Galactic center. The absence of radio recombination line emission and the presence of strong linear polarization indicate synchrotron emission from GCRA (e.g. Tsuboi et al. (1985, 1986); Sofue et al. (1987); Seiradakis et al. (1989)). The radio spectrum in the frequency range from 330 MHz to 43 GHz can be reproduced by a power law with a spectral index of $\alpha \sim 0.3$ (Lesch et al., 1988; Reich et al., 1988; Anantharamaiah et al., 1991; Tsuboi et al., 1995). Synchrotron emission indicates the presence of magnetic fields and high energy particles at the GCRA.

The GCRA may be also the part of even larger structure known as the GC Ω-lobe (Sofue & Handa, 1984; Sofue, 1985), which is a loop-like structure extended of ~ 200 pc diameter in the direction of the positive Galactic latitude. The GCRA is located at a foot point of the Ω-lobe, while another foot point coincides with a giant molecular cloud Sgr C, where a bright nonthermal filament (see next subsection) is embedded. However, a physical connection between these nonthermal radio filaments and Ω-lobe is still uncertain.

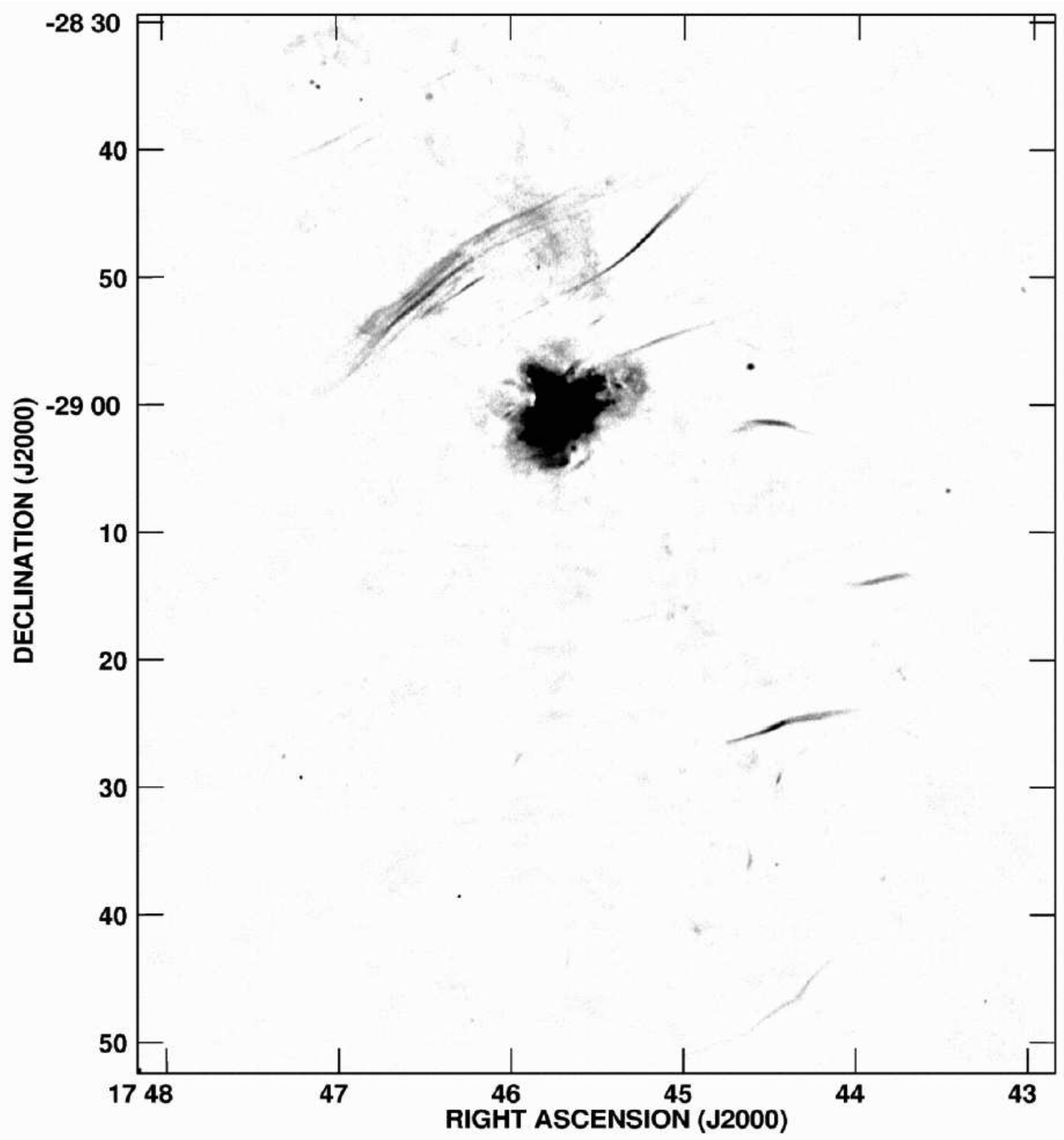

Figure 2.11: VLA 330 MHz (90 cm) image of the central $\sim 1.0^{\circ} \times 1.2^{\circ}$ region of the Galaxy. The beam size of the observation is $12'' \times 7''$ and the rms noise is 1.6 mJy beam^{-1}. Color scale is linear between -2 and 50 mJy beam^{-1} (Nord et al., 2004).

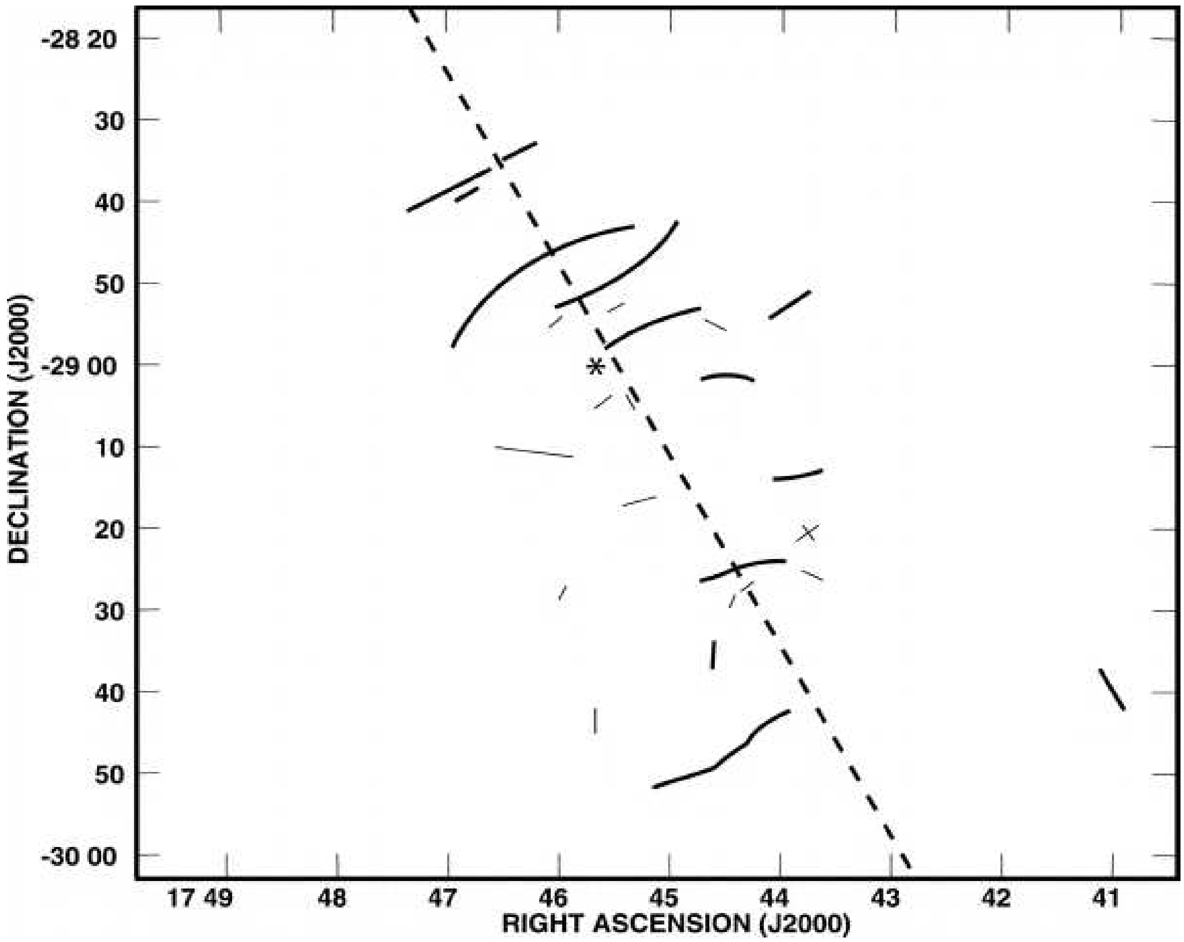

Figure 2.12: A schematic of the distribution of nonthermal radio filaments (NTRFs) near the Galactic center based on th VLA 90 cm wide-field image. A dashed line represents the Galactic plane and an asterisk represents the position of Sgr A*. Confirmed NTRFs are shown in Heavy dark lines, while NTRF candidates are shown in thin lines (LaRosa et al., 2004).

2.4.2 Nonthermal Radio Filaments (NTRFs)

After the discovery of GCRA (Yusef-Zadeh et al., 1984), a number of nonthermal radio filaments (NTRFs) have been resolved with high resolution observations performed by VLA; G0.08−0.15 and G259.96+0.09 named Northern and Southern threads (Morris & Yusef-Zadeh, 1985; Anantharamaiah et al., 1991), G359.1−0.2 so called the "Snake" (Gray et al., 1995), NTRF259.40−0.07 near the Sgr C (Liszt & Spiker, 1995), G359.54+0.18 (Yusef-Zadeh et al., 1997), and G358.85+0.47 called the "Pelican" (Lang et al., 1999).

The NTRFs are unique to the GC region within $\sim$ 150 pc and share the following characteristics; (1) extreme high length / width ratio with typically a few tens of parsecs for the length, yet less than 1 pc for the width, (2) orientation perpendicular to the Galactic plane within the angle of $\sim 20°$, (3) strong (up to $\sim 50\%$) linear polarization, (4) rather negative or flat spectral indices of $\alpha \sim -1.0$ to 0.5, (5) large rotation measures (grater than 1000 rad m^{-1}), and (6) alignment of the intrinsic magnetic field along the long axis of the filament.

Recently, LaRosa et al. (2000) successfully resolved a number of filamentary structures and small diameter sources from the region of the central $\sim$ 300 pc of the Galaxy with applying a new image restoration technique. In these sources, twenty sources are listed as candidates of new NTRFs based on the evaluation of their morphological feature (Nord et al., 2004). LaRosa et al. (2004) detected a linear polarization from some of these candidates with VLA 6 cm pointing observations. Now 9 NTRFs and 20 NTRF candidates are identified within the 300 pc of the GC region. Table 7.2 shows radio properties of NTRFs/NTRF candidates, while 90 cm radio image and schematics of their spatial distribution are shown in Figure 2.11 and Figure 2.12.

Although a few tens of NTRFs have been discovered, a number of issues remain unresolved and still debatable. Most fundamental of these is, what is the source of relativistic particle and the mechanism of their acceleration ? Then, what do the NTRFs suggest about the condition of magnetic field at the GC, and what can confine NTRFs within such a narrow structures.

2.4.3 Strength of the magnetic field

Several estimates for the strength of NTRF magnetic fields have been made. Based on radio continuum measurements, several NTRFs require a few tenths of a milligauss assuming energy equipartition of magnetic field and synchrotron emitting electrons (e.g. Gray et al. (1995), Lang et al. (1999)). On the other hand, The absence of any bending or distortion of the NTRFs against the strong ram pressure of the GC molecular clouds indicates field strength of NTRFs of $\sim$ 1 mG (e.g. Yusef-Zadeh & Morris (1987), Chandran (2001)).

Such field strengths of NTRFs are considerably strong by over two orders of magnitude comparing with a general interstellar magnetic field, which is no more than a few tens of μG. Thus, strong magnetic pressure of NTRFs must expand NTRFs beyond their observed width within the synchrotron lifetime of electrons unless they are confined by some comparable pressures. The confinement problem is not an issue if the 1 mG magnetic field are distributed among the GC region. In this case, NTRFs are explained as the flux tubes which are illuminated by high energy electrons generated from some local interactions of molecular clouds and ISM. If this is the case, energy density of magnetic field of the GC region should be consequently extremely high ($u_{\rm B} \sim 4 \times 10^{-8}$ ergs cm^{-3}) and total magnetic energy of the GC region is amount to $E_{\rm B} \simeq 6 \times 10^{54}$ ergs $(R/75\ \rm pc)^2 (L/300\ \rm pc)$. Alternatives to the pervasive magnetic field explanations have been proposed based on the idea that some local enhancement of field strength occur around the site of NTRFs (Shore & LaRosa, 1999; Yusef-Zadeh, 2003).

2.5 Gamma-ray Emissions from the GC region

2.5.1 Extended emission of 1.809 MeV ^{26}Al line

The COMPTEL instrument on-board *Compton Gamma Ray Observatory; CGRO* discovered 1.809 MeV ^{26}Al line emission from the GC region (Diehl et al., 1995). The emission seems extended along the Galactic plane at the scale of a few tens of degrees (Figure 2.13). The the lifetime of ^{26}Al$-^{26}$Mg decay process is short ($\tau_{1/2} \sim 7.2 \times 10^6$ year) and ^{26}Al is thought to be produced by a nucleosynthesis of massive stars. Therefore observed Gamma-ray line emission is originated from Type II supernovae (explosions of 12$-$30 $M_\odot$ stars) and/or stellar wind of Wolf-Rayet stars (>30 $M_\odot$ stars was evolved) (Diehl et al., 1995; Prantzos & Diehl, 1996; Naya et al., 1996). It also should be the evidence for a massive star formation occurred at the GC region no longer than a few million years ago. Recently, Diehl et al. (2003) reported a clear detection of ^{26}Al line at a significance of $5{-}7\sigma$ from a inner $l \sim \pm\ 30°$ and $b \sim \pm\ 20°$ region of the Galaxy with SPI spectrometer on *INTEGRAL* satellite, which confirms the COMPTEL result.

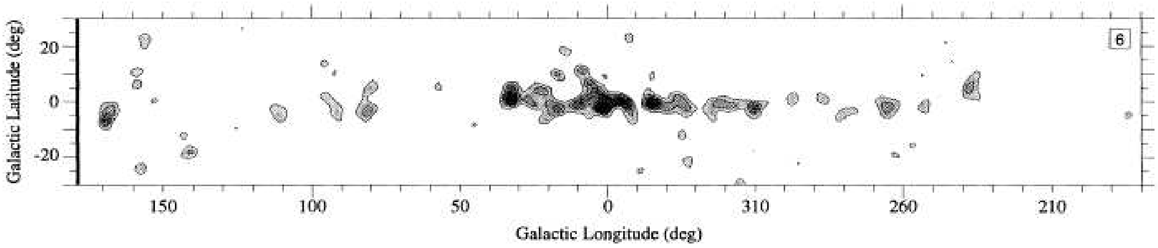

Figure 2.13: A ^{26}Al line (1.809 MeV) intensity map of the Milky Way. Continuum emission is subtracted (Diehl et al., 1995).

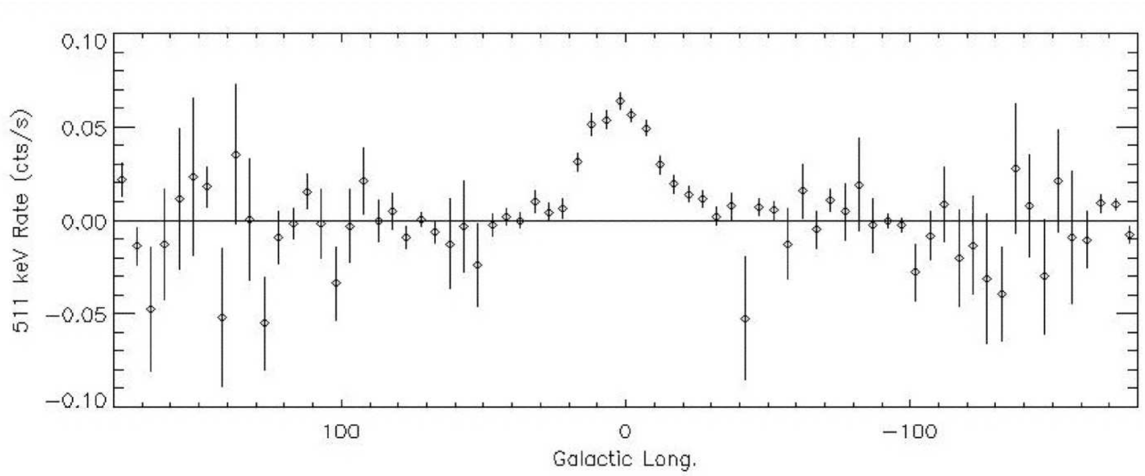

Figure 2.14: Background-subtracted 511 keV count rate map as a function of Galactic Longitude for the region $|b| < 20°$ obtained with *INTEGRAL*/SPI (Teegarden et al., 2004).

2.5.2 511 keV electron-positron pair annihilation line

An enhancement of electron-positron annihilation radiation in the direction of the Galactic center was first reported with balloon-borne experiments over 30 years ago (Johnson et al., 1972). In 1990s, OSSE experiment on the *CGRO* observed Galactic center region many times. These data are well described by bulge distribution plus disk component; a Gaussian of FWHM $\sim 5°$ plus an elongated Gaussian with a FWHM of $\sim 35°$ in longitude (Kinzer et al., 2001). Although early results of OSSE claimed a possible enhancement in the positive latitude, so-cold "annihilation fountain" (e.g. Purcell et al. (1997)), later analyses can found little or no evidence for the feature (Kinzer et al., 2001).

2.5.3 High Energy Gamma-rays from the GC region

The EGRET detector on-board *CGRO*, which have a sensitivity at the energy range of 30 MeV−100 GeV, detected high energy gamma-ray emission from the GC region (Mayer-Hasselwander et al., 1998). This source is extended in the scale of $\sim$ 85 pc (0.6°) at the peak position is within $\sim$ 30 pc (0.°2) from the position of Sgr A*. The source is listed as a unidentified EGRET source 3EG J1746−2851 in the third EGRET catalog (Hartman et al., 1999). The possible origin of the strong gamma-ray source are thought to be (1) a single or a few young pulsars ($t < 10^3$ yr), (2) an inverse Compton process between high energy electrons and FIR photons, and (3) neutralino annihilation of WIMP particles at the core of the Galaxy.

TeV gamma rays have been recently discovered in the direction of the GC with ground-based experiments using Imaging Air Cerenkov Telescopes (IACTs). CANGAROO-II group succeeded at a significant detection of sub-TeV gamma-rays with an energy threshold of 250 GeV (Tsuchiya et al., 2004). An Energy spectrum between 250 GeV−2 TeV is determined to be quite steep ($\propto E^{-4.6 \pm 0.5}$) and flux is lower than 0.1 Crab at 1 TeV. Although a peak position of the gamma ray excess is coincide with both Sgr A*, Sgr A East, and 3EG J1746−2851, the angular resolution of CANGAROO-II telescope ($\sim$0.°32) is not enough to decide whether its origin is. Using 26 hours data accumulated over a period of 1995−2003 with Whipple 10 m telescope, Kosack et al. (2004) reported an gamma ray excess of 3.7 σ significance above 2.8 TeV at the GC. The 95% confidence region is spatially extended about $15'$ which include the position of Sgr A*. Recently, H.E.S.S. group reported the detection of very high energy gamma-rays from the Galactic center (Aharonian et al., 2004). They resolved a point-like source within $1'$ of Sgr A*. The center position of the gamma-ray excess is RA = $17^{\mathrm{h}}45^{\mathrm{m}}41.3^{s} \pm 2.0^{\mathrm{s}}$ and Dec. = $29°00'22'' \pm 32''$ (Figure 2.15). An energy spectrum of the point-like sources can be reproduced by a power-law with a spectral index of $\alpha = -2.2 \pm 0.09 \pm 0.15$, which is significantly flatter than the result of

CANGAROO-II (Tsuchiya et al., 2004), as shown in Figure 2.16. A measured flux $(1.82 \pm 1.2) \times 10^{-7}$ m^{-2} s^{-1} above 165 GeV threshold is also differ from previous results.

In addition to the point-like source, Figure 2.15 exhibits some diffuse-like enhancement of significance along the Galactic plane, which is under investigation.

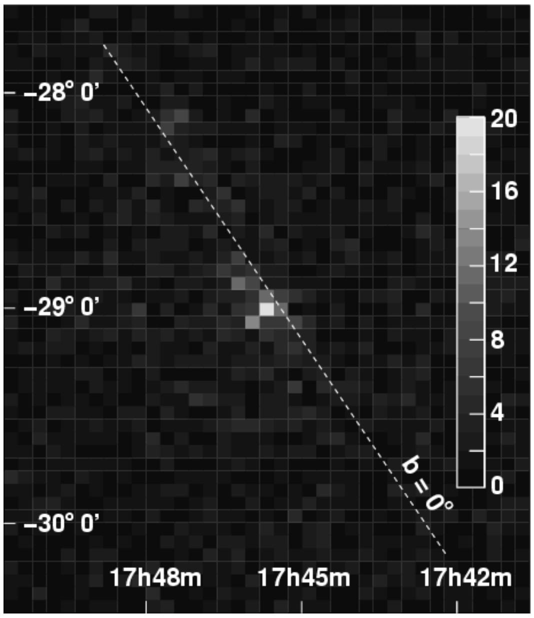

Figure 2.15: Gamma-ray significance map within 3° × 3° of the GC centered on Sgr A* obtained with the H.E.S.S. observation (Aharonian et al., 2004).

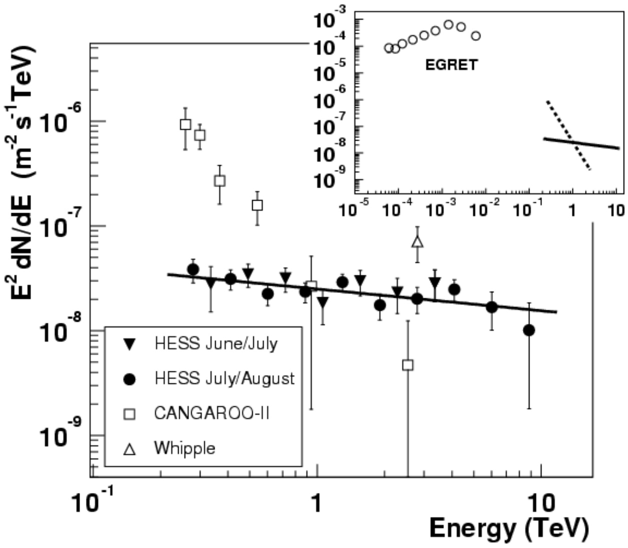

Figure 2.16: Energy spectrum of gamma-rays from the Galactic center (Aharonian et al., 2004).

Chapter 3

Instrumentation

3.1 *Chandra X-ray Observatory*

3.1.1 Mission Overview

The *Chandra* project, which is managed by NASA / MSFC (Marshall Space Fright Center), is casted as the X-ray component of NASA's four great observatories The other three are *Habble Spece Telescope* (Optical,NIR), *Compton Gamma Ray Observatory* (Gamma-ray), and *Spitzer* (IR). The *Chandra* Spacecraft is successfully launched by NASA's Space Shuttle Colombia on July 23, 1999.

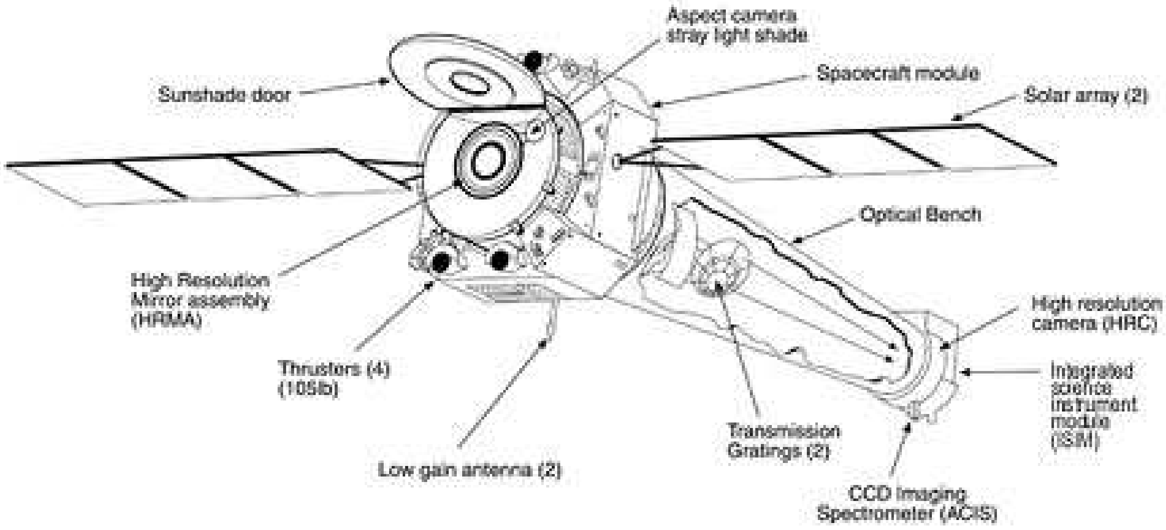

Figure 3.1: The overall view of *Chandra* X-ray Observatory. This image is credited to NASA/CXC/SAO. http://chandra.harvard.edu/resources/

The orbit of *Chandra* is highly elliptical and varies as time goes by. At the point of October 2003, The distance of the apogee and peregee from the earth was $\sim$ 132,000 km and $\sim$ 32,000 km. The orbit makes it possible to perform high efficiency observation because *Chandra* can spend $\sim$ 75% of its period above the radiation belt around the earth. Moreover, the long period ($\sim$ 63.5 hour) allow for continuous observations as long as 160 ksec.

Chandra is comprised of a spacecraft and a telescope / science-instrument payload. The spacecraft includes six subsystems; (1) structures and mechanical subsystem, (2) thermal control subsystem, (3) electrical and power subsystem, (4) communication, command, and aspect determination subsystem, (5) pointing control and aspect determination subsystem, and (6) integral propulsion subsystem. On the other hand, The principal element of the observatory is an X-ray telescope (HRMA), focal plane science instruments (SIs) and the objective transmission gratings (HETG and LETG). SIs consist of two types of X-ray detectors; CCD imaging spectroscopy arrays (ACIS) and micro channel plate imaging arrays (HRC). The position of each component is shown in Figure 3.1.

In the following subsections, we concentrate on describing HRMA and ACIS instrument. Detailed description of *Chandra* can be found in the *Chandra* Proposers' Observatory Guide (The latest version is 6.0, Dec. 15, 2003).

3.1.2 HRMA – High Resolution Mirror Assembly

The most distinguished feature of *Chandra* is its excellent angular resolution ($\Delta\theta \sim 0.5''$), which is the highest value among that of the other past and present X-ray satellites so far. High Resolution Mirror Assembly (HRMA) make it possible for *Chandra* to achieve the unprecedented spatial resolition.

HRMA represents a logical progression from the X-ray mirror of *Einstein* (Giacconi et al., 1979) and *ROSAT* (Trümper, 1983; Aschenbach, 1991). HRMA comprised of a nested set of four paraboloid-hyperboloid (Walter Type-I; Aschenbach (1985) reviews detailed of the X-tay optics) grazing-incidence X-ray mirror pairs. The eight mirrors are fabricated from Zerodur[1] glass, polished and coated with iridium on a binding layer of chromium. A schematic configuration of HRMA is shown in Figure 3.2. The Focal

[1] Zerodur is a glass ceramic with an extremely low thermal expansion coefficient produced by Schott AG.

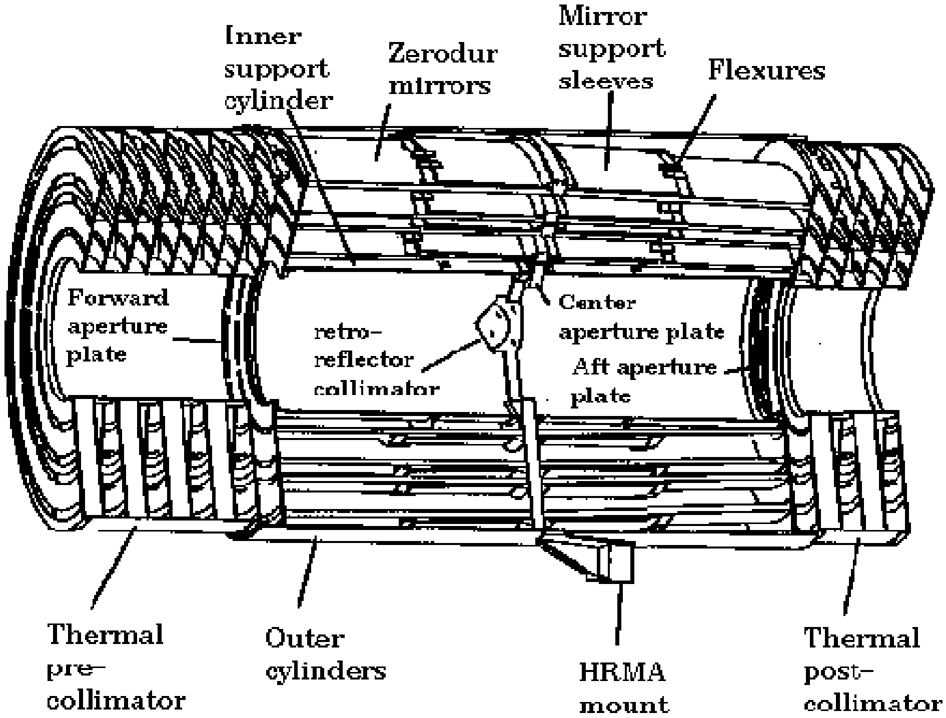

Figure 3.2: A cross-sectional view of HRMA mirror assembly. (*Chandra* Proposers' Observatory Guide 2003)

length of each mirror is $\sim$ 10 m and the pair diameters are range from $\sim$ 0.65 to 1.23 m.

HRMA Effective Area

The unobscured geometric clear aperture of HRMA is 1145 cm^2. Although supporting struts of the mirror nests obstruct the HRMA clear aperture, the effect is less than 10%. The HRMA throughput is a function of input X-ray energy and off-axis angle, because reflectivity on the mirrors depend on X-ray energy as well as grazing angle. Figure 3.3 represents an energy dependence of the on-axis HRMA effective area. The convolved effective areas; the product of HRMA effective area and quantum efficiencies of a focal plane instrument (ACIS or HRS), are also presented. Figure 3.4 describes the effects of off-axis vignetting on the effective area for the various energies. The plotted data are averages over the azimuthal angle.

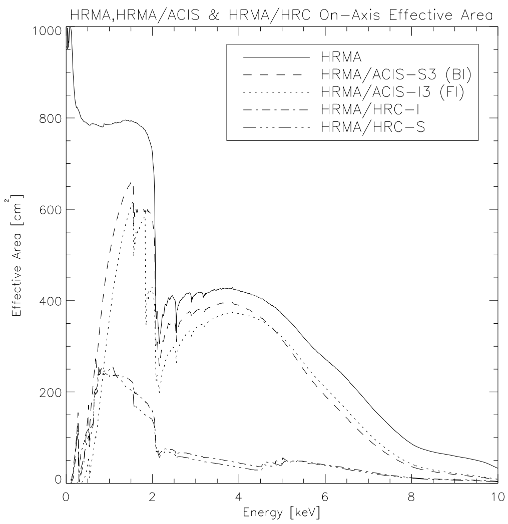

Figure 3.3: The HRMA, HRMA/ACIS, and HRMA/HRI effective areas as a function of X-ray energy (*Chandra* Proposers' Observatory Guide 2003)
.

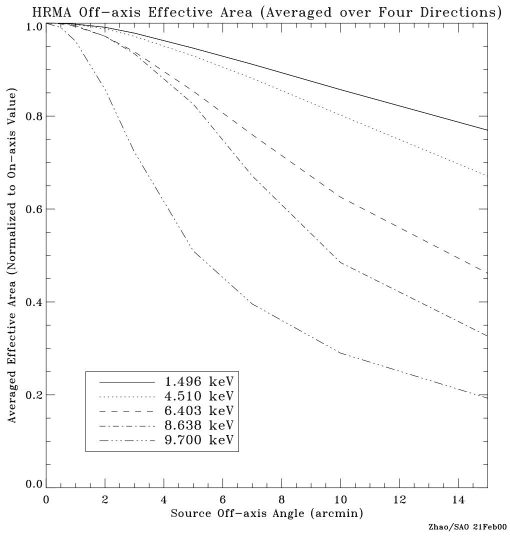

Figure 3.4: The HRMA effective area as a function of off-axis angle for selected energies. Data represents azimuthal averaged value and normalized to that of on-axis area for each energy (*Chandra* Proposers' Observatory Guide 2003).

Point Spread Function (PSF)

The point spread function (PSF) represents the distribution of accumulated X-ray photons on the focal plane instruments at a given energy. A shape of a PSF can be approximated with a two-dimensional Gaussian. One of the most useful parameters to evaluate the sharpness of the PSF is the encircled energy fraction as a function of radius from the PSF center. As shown in Figure 3.5 and 3.6, the PSF and encircled energy fraction depend upon incident X-ray energy and off-axis angle. The PSF broadens and encircled energy fraction decreases as the off-axis angle increases and as the incident X-ray energy increases. The former effect is due to mirror aberrations, while the latter is due to large X-ray scattering.

Note that the ACIS-I surfaces are not axially symmetric with respect to the HRMA optical axis, because the aim-point of HRMA is located at the inner corner of the one of the four ACIS-I array, ACIS-I3.

3.1.3 ACIS – Advanced CCD Imaging Spectrometer

The Advanced CCD Imaging Spectrometer (ACIS) is the focal-plane detector which has a capability of acquire high resolution images and moderate resolution spectra at the same time. ACIS can also be used in conjunction with the High Energy Grating Transmission (HETG) or Low Energy Grating Transmission (LETG) to obtain higher resolution X-ray spectra of point sources.

Figure 3.7 shows the configuration of the ACIS instrument. ACIS consist of 10 planer 1024×1024 pixels CCDs; four arranged in a 2×2 array (ACIS-I0, I1, -I2 and -I3) used for imaging, and six arranged in a 1×6 array (ACIS-S0, -S1, -S2, -S3, -S4, and -S5) used either for imaging or as a grating readout. The pixel size of the CCDs is 24.0 microns, equivalent to the angular scale of $0.492''$. Since the size of the chip boundaries is equivalent to 22 pixels for ACIS-I and 18 pixels for ACIS-S, the array size is 16.9×16.9 arcmin for ACIS-I and 8.3×50.6 arcmin for ACIS-S. The spatial resolution for on-axis imaging with ACIS is limited by the size of the CCD pixels and not the HRMA. All CCDs are utilized for Front Illuminated (FI) except for two Back Illuminated (BI) chips (ACIS-S1 and -S3).

Quantum Efficiency and Effective Area

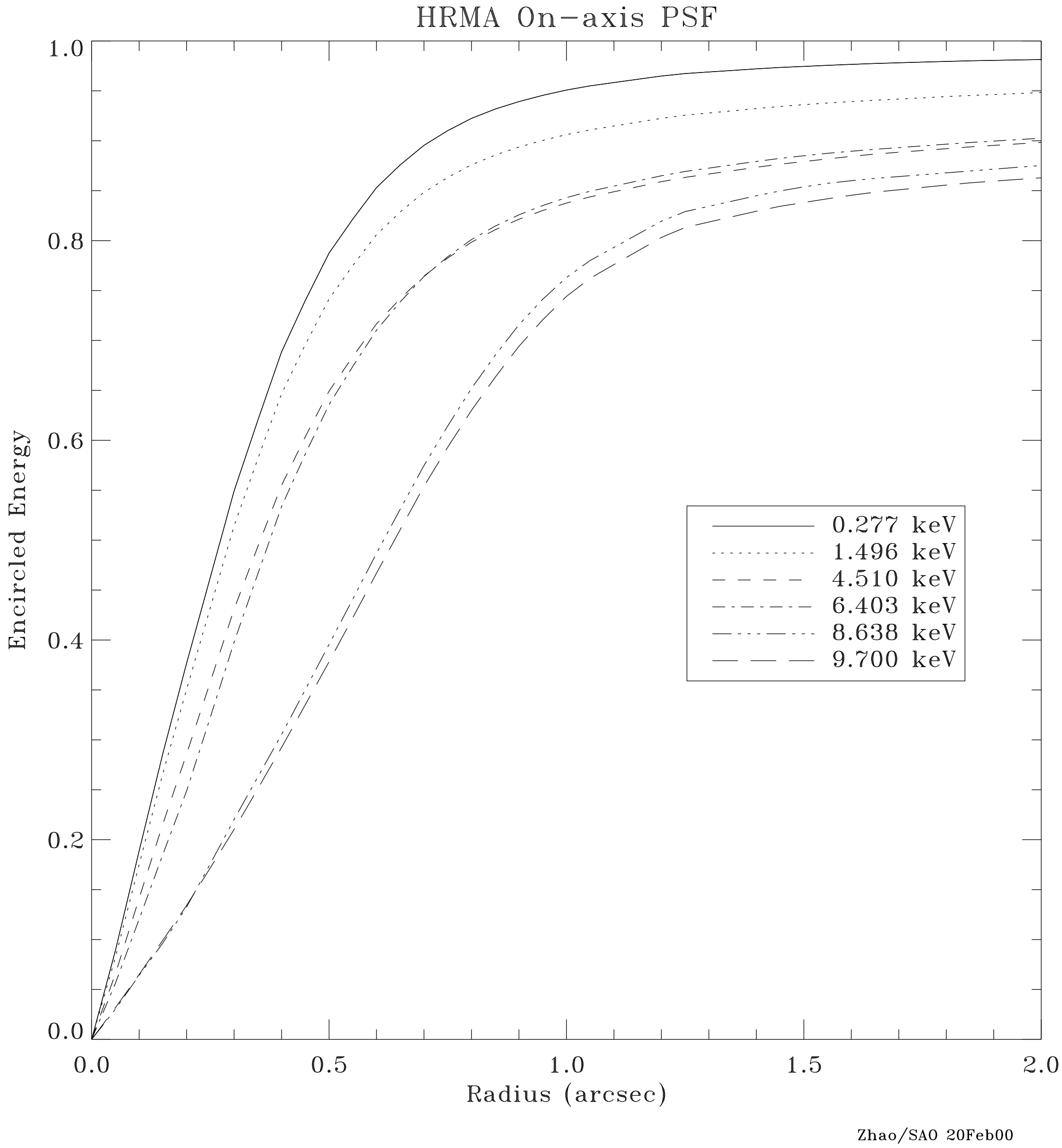

Figure 3.5: The *Chandra* HRMA on-axis PSFs of several representative incident X-ray energies. The fraction of the encircled energy as a function of angular radius is presented. (*Chandra* Proposers' Observatory Guide 2003).

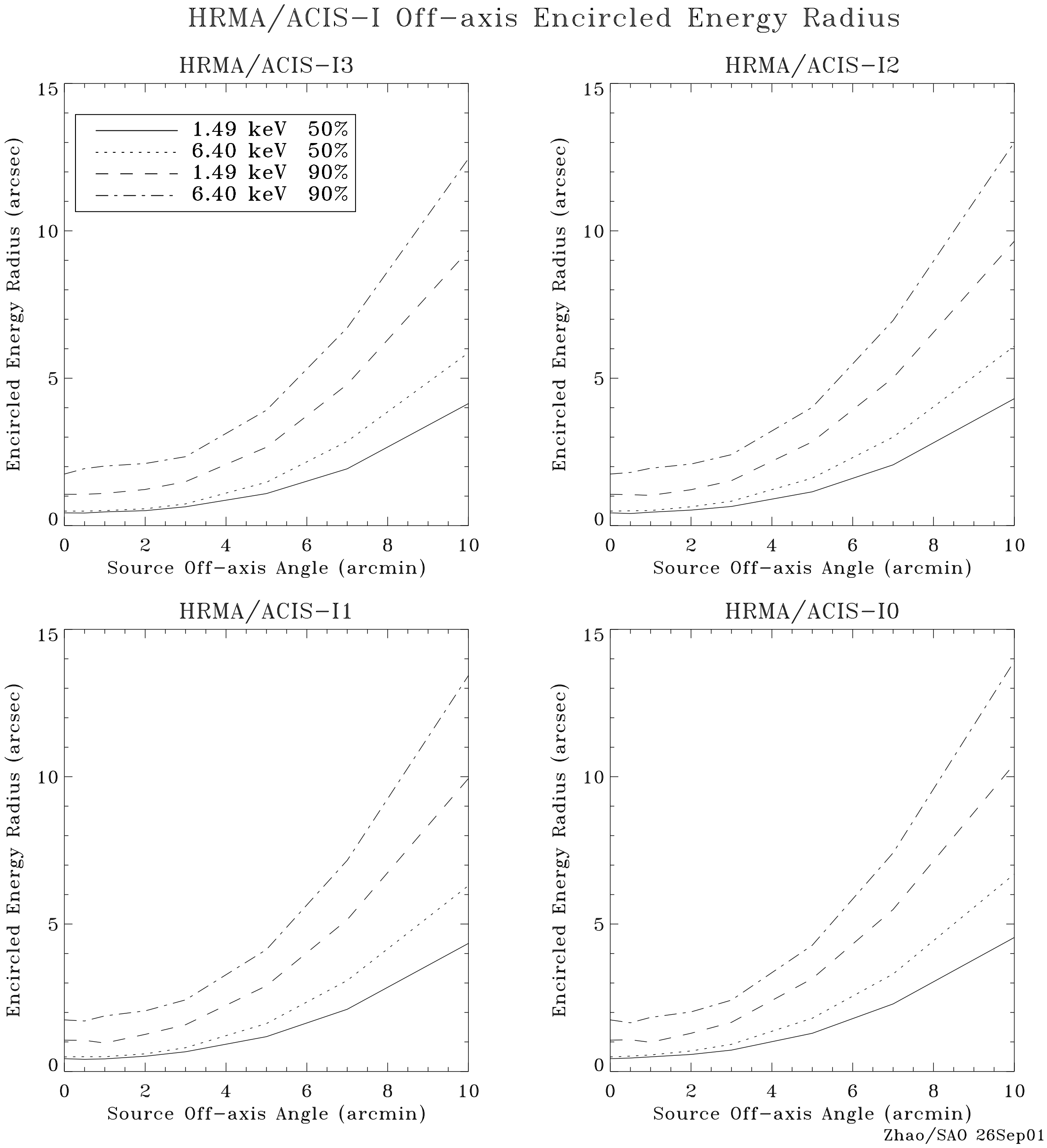

Figure 3.6: The dependences of the *Chandra* HRMA/ACIS-I PSF on off-axis angle for given incident X-ray energies. The 50% and 90% encircled energy radii as a function of off-axis angle at two incident X-ray energies (1.49 and 6.40 keV) are presented. (*Chandra* Proposers' Observatory Guide 2003).

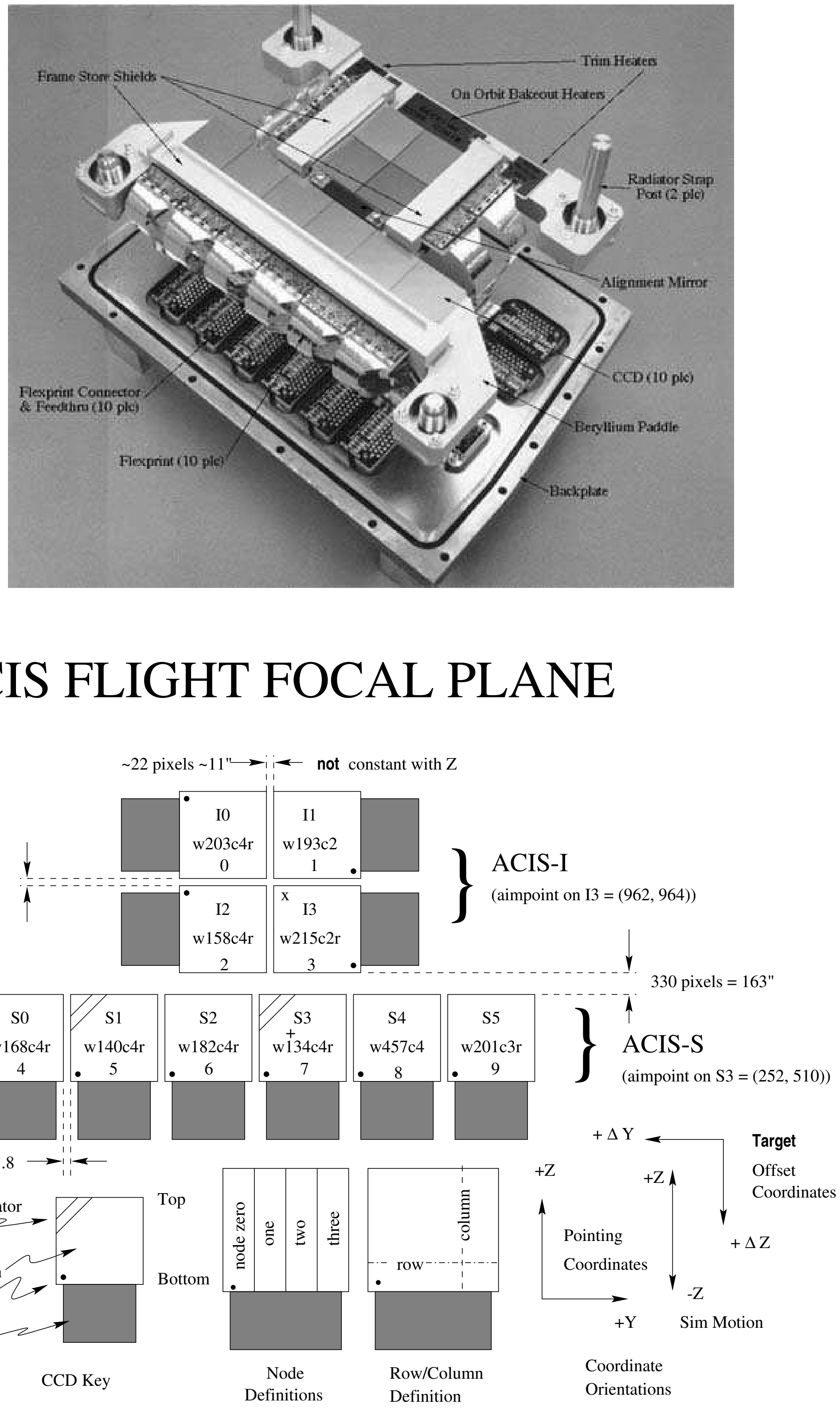

Figure 3.7: (Top) A photo of the whole view of the ACIS instrument. (Bottom) the configuration of the ACIS array on the focal plane. Insight to the terminology is given in the lower left (*Chandra* Proposers' Observatory Guide 2003).

The quantum efficiency (QE) for the FI chips varies somewhat with row number (not shown), and decreases by 5-15% farthest from the readout at energies above about 4 keV. This is due to the migration of good grades to bad grades produced by charge transfer inefficiency, which varies with row number. The QE variation with position for the BI chips is much smaller.

Figure 3.8 shows the vignetting (defined as the ratio of off-axis to on-axis effective area) as a function of energy at several off-axis angles. The detector was appropriately offset for each off-axis angle so that the data were obtained at the same focal position, minimizing the effects of any spatially-dependent variations in the CCD response.

Energy Resolution

The ACIS FI CCDs originally approached the theoretical limit for the energy resolution at almost all energies, while the BI CCDs exhibited poorer resolution. The pre-launch energy resolution as a function of energy is shown in Figure 3.9. However, subsequent to launch and orbital activation, the energy resolution of the FI CCDs has become a function of the row number, being near pre-launch values close to the frame store region and substantially degraded in the farthest row. The loss of energy resolution was due to increased charge transfer inefficiency (CTI) caused by low energy protons, encountered during radiation belt passages and reflecting off the X-ray telescope (HRMA) onto the focal plane. Subsequent to the discovery of the degradation, operational procedures were changed, the ACIS is not left at the focal position during radiation belt passages. Since this procedure was initiated, no further degradation in performance has been encountered beyond that predicted from pre-launch models. The BI CCDs were not impacted and this result is consistent with the proton-damage scenario - it is far more difficult for low-energy protons from the direction of the HRMA to deposit their energy in the buried channels of the BI devices, since the channels are near the gates and the gates face in the direction opposite to the HRMA . Thus the energy resolution for the two BI devices remains at their pre-launch values (the difference in energy resolution of the BI flight devices compared to pre-launch is < 1 ADU at the time of writing).

The position-dependent energy resolution of the FI chips depends significantly on the ACIS operating temperature. Since activation, the ACIS operating temperature has been lowered in steps and is now set at the lowest temperature thought safely and consistently achievable ($\sim -120°$C).

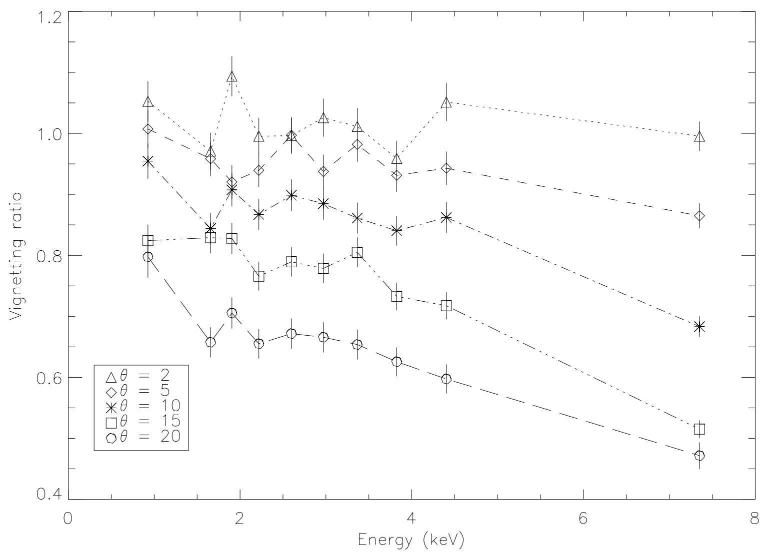

Figure 3.8: Vignetting effect(defined the ratio of off-axis to on-axis effective area) as a function of energy for several off axis angles in arcminutes.

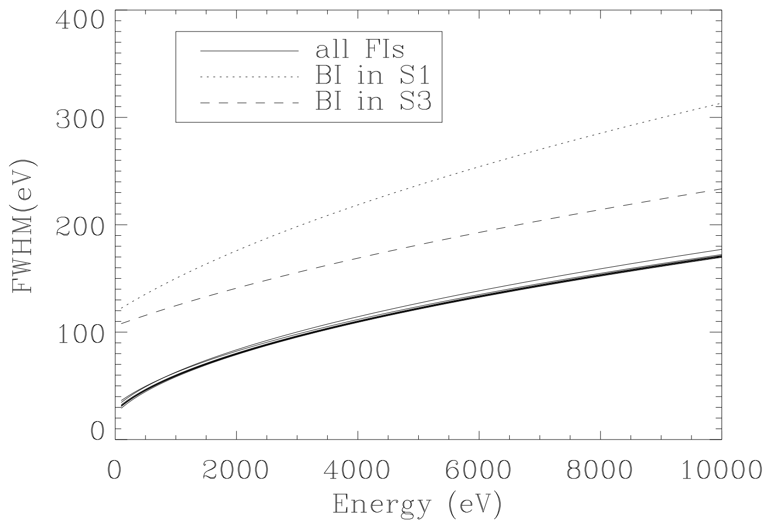

Figure 3.9: The ACIS pre-launch energy resolution as a function of incident X-ray energy.

On-Orbit Background and Sensitivity Limit

There are three components to the on-orbit background. The first is that due to the cosmic X-ray background (a significant fraction of which resolves into discrete sources during an observation with Chandra). The second component is commonly referred to as the charged particle background. This latter arises both from charged particles, photon and other neutral particle interactions that ultimately deposit energy in the instrument. The third component is the "readout artifact" which is a consequence of the "trailing" of the target image during the CCD readout.

Several "observations" were carried out with the ACIS in the stowed position, shielded from the sky by the SIM structure, collecting data in normal imaging TE VFAINT mode at -120C. Chips I0, I2, I3, S1, S2, S3 were exposed. The SIM position was chosen so that the on-board calibration source did not illuminate the ACIS chips. This allowed us to characterize the non-celestial contribution to X-ray background (i.e., from charged particles). The resulting spectra from different chips are shown in Figure 3.10. We have not observed any background flares in the stowed position. Therefore, the ACIS stowed background is a good representation of the quiescent non-X-ray background in the normal focal position and can be used for science observations.

In real observations, two more components to the background come into play. The first is the cosmic X-ray background which, for moderately long ($\sim$ 100 ks) observations will be mostly resolved into discrete sources (except for the diffuse component below 1 keV) but, nevertheless, contributes to the overall counting rate. The second is a time-variable "flare" component caused by any charged particles that may reflect from the telescope and have sufficient momentum so as not to be diverted from the focal plane by the magnets included in the observatory for that purpose, or from secondary particles.

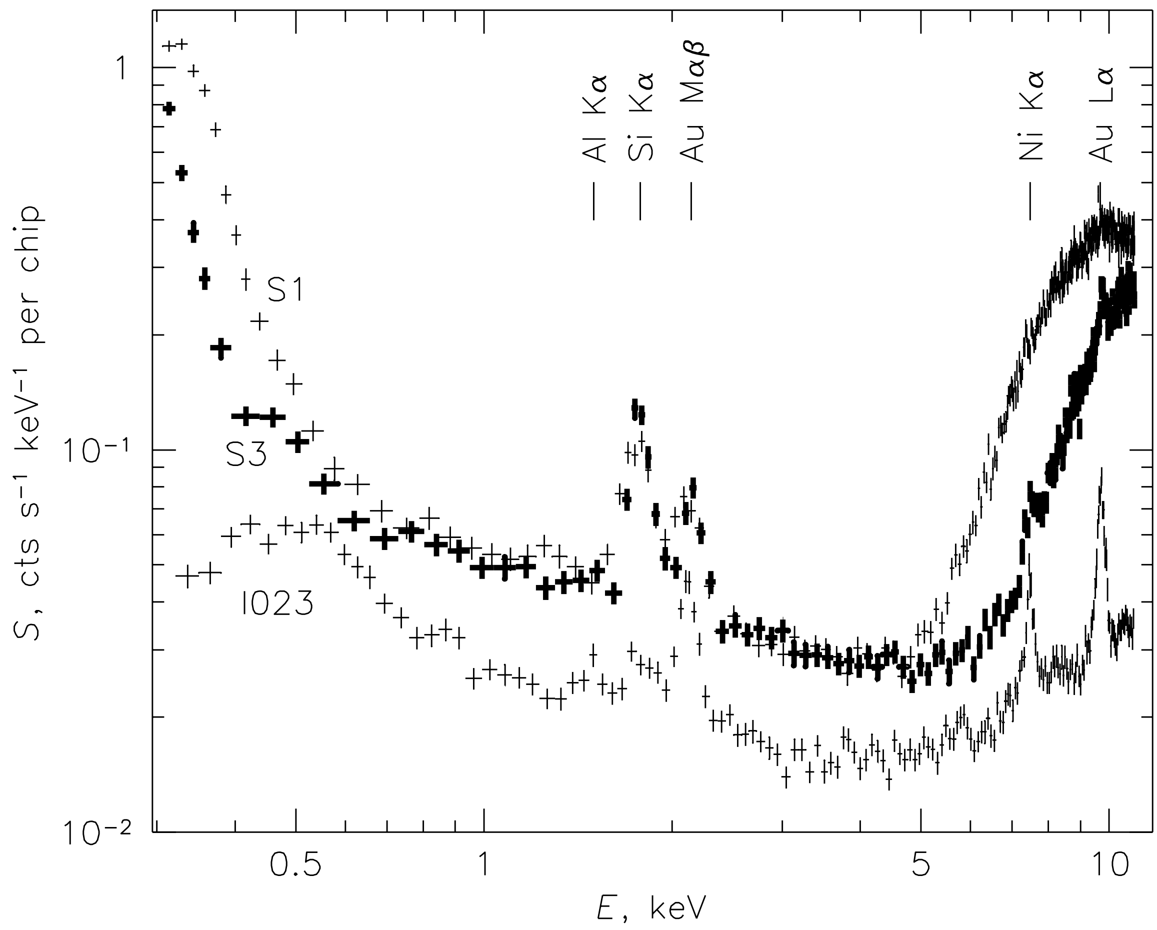

Figure 3.10: A Non X-ray Background (NXB) spectra taken by ACIS CCDs. Chip S2 is similar to the ACIS-I chips (denoted I023 in the figure) and not shown for clarity. Line features are due to fluorescence of material in the telescope and focal plane instrument.

Chapter 4

Thermal Structures in the GC region

4.1 X-ray Study of G0.570−0.018

In this chapter, we reports the X-ray analyses and discussion for the peculiar X-ray source, G0.570−0.018, located near a giant molecular cloud Sgr B2. Although existence of the X-ray source is recognized as a strong iron line emitting object with *ASCA* observation (Sakano et al., 1999), while the nature of G0.570−0.018 cannot be debated because of limited photon statistics and spatial resolution of *ASCA*. Using *ASCA* and *Chandra* data, we investigate the morphological and spectral properties of G0.570−0.018 for the first time.

4.1.1 Observations and data reductions

We both use *ASCA* GIS and *Chandra* ACIS data for the analyses of G0.570−0.018 presented in the following sections. The observation log is shown in Table 4.1.

As for *ASCA*, three pointings of GIS (GIS2 and 3) data are available. Unfortunately, G0.570−0.018 is placed on the center of the SIS detector, where there is the central gap of SIS CCDs, hence we cannot use SIS data for the analysis. For the data of GISs, nominal bit assignment of PH mode was used in the high and medium bit rate. After applying the standard data reduction, we finally obtained the effective exposure time of 17.5 ksec for the 1993 October observation and 80.0 ksec for the 1994 September observation, respectively.

As for *Chandra*, the data of ACIS-I field of Obs.ID=944 is used for the following analysis. The same method of Sgr B2 analysis (Murakami et al., 2001b) was applied for standard data processing in creating level=2 event file. In addition, G0.570−0.018 is placed at the furthest point of the detector readout of ACIS-I3 CCD, hence is heavily affected by a Charge Transfer Inefficiency (CTI). In order to minimize the degradation by the CTI effect, we applied the software to correct the CTI developed by (Townsley et al., 2000). We also corrected the energy gain using the instrumental emission lines from Ni-Kα (7.5 keV) and Au-Kα as calibration sources, then achieved an accuracy of < 0.5 % (90 % confidence).

Table 4.1: *ASCA* and *Chandra* observation log for G0.570−0.018

Sequence ID[a]	Obs. start time[b] (UT)	Nominal point (Ra, Dec)$_{J2000}$	Exposure (ksec)
ASCA GIS			
60011000	1993-10-01-21:16	17 47 09.58 28 32 24.0	19.9
52006000	1994-09-22-03:45	17 46 59.26 28 27 54.7	63.1
52006001	1994-09-24-02:05	17 46 59.26 28 27 54.7	25.0
Chandra ACIS			
944	2000-06-03-29-09:44	17 47 06.70 -28 26 47.29	98.9

[a] Corresponding with Observation ID in case of *Chandra*.
[b] Year-Month-Date-Hour-Minutes in UT.

4.1.2 X-ray morphology

In the *ASCA* GIS image pointed at the Sgr B2 cloud, we find a local excess in the west of Sgr B2. This excess is clearly seen if we limit the X-ray energy band of 6.0–7.0 keV, which include the iron K-shell transition line. Figure 4.1 gives an intensity map of 6.0–7.0 keV band X-ray photons obtained with *ASCA* GIS. The brightest source located at the northeast of the image is the giant molecular cloud Sgr B2 (Murakami et al., 2000). The second brightest excess located near the center of the image is a newly discovered X-ray source. Due to the limited photon statistics and spatial resolution of *ASCA* GIS, error of the peak position of the diffuse structure is rather large of $0^\circ.55 \leq l \leq 0^\circ.57$, $-0^\circ.02 \leq b \leq 0^\circ.00$.

In order to investigate the accurate position and fine spatial structure of this diffuse source, we inspect the hard X-ray image observed with *Chandra* ACIS. Thanks to the fine spatial resolution of *Chandra*, As is shown in Figure 4.2, we see a complex

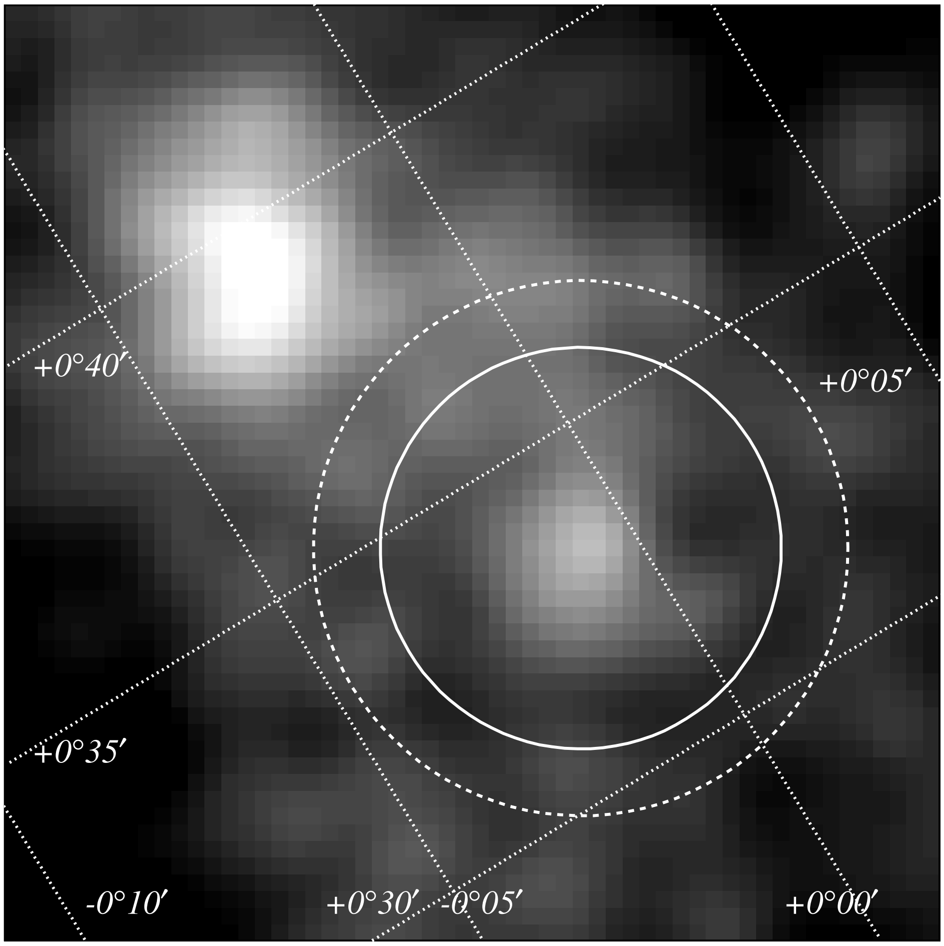

Figure 4.1: *ASCA* GIS image of G0.570−0.018 with 6.0−7.0 keV band. The spectrum is extracted within the 3′ circle (solid line), while the background is from the annulus between the solid and dashed circles ($3' < r < 4'$). The dotted lines are the Galactic coordinates with grid spacing of 5′.

X-ray structure with a ring of about $10''$ radius and an east-to-west tail from the ring. The center coordinate of the ring structure is determined to be R.A.= $17^{\mathrm{h}}47^{\mathrm{m}}02\mathrm{s}.6$, Dec= $-28°27'33''$ (epoch 2000), which corresponds to $(l,\ b)$ = $(0°.570,\ -0°.018)$, the same position of the *ASCA* diffuse source within the statistical error. We hence designate this source as G0.570−0.018/CXO J174702.6−282733. To investigate the statistical significance of the shell-like structure, we make a radial profile with the center at $(17^{\mathrm{h}}47^{\mathrm{m}}02^{\mathrm{s}}.6,\ -28°27'33'')_{\mathrm{J2000}}$.

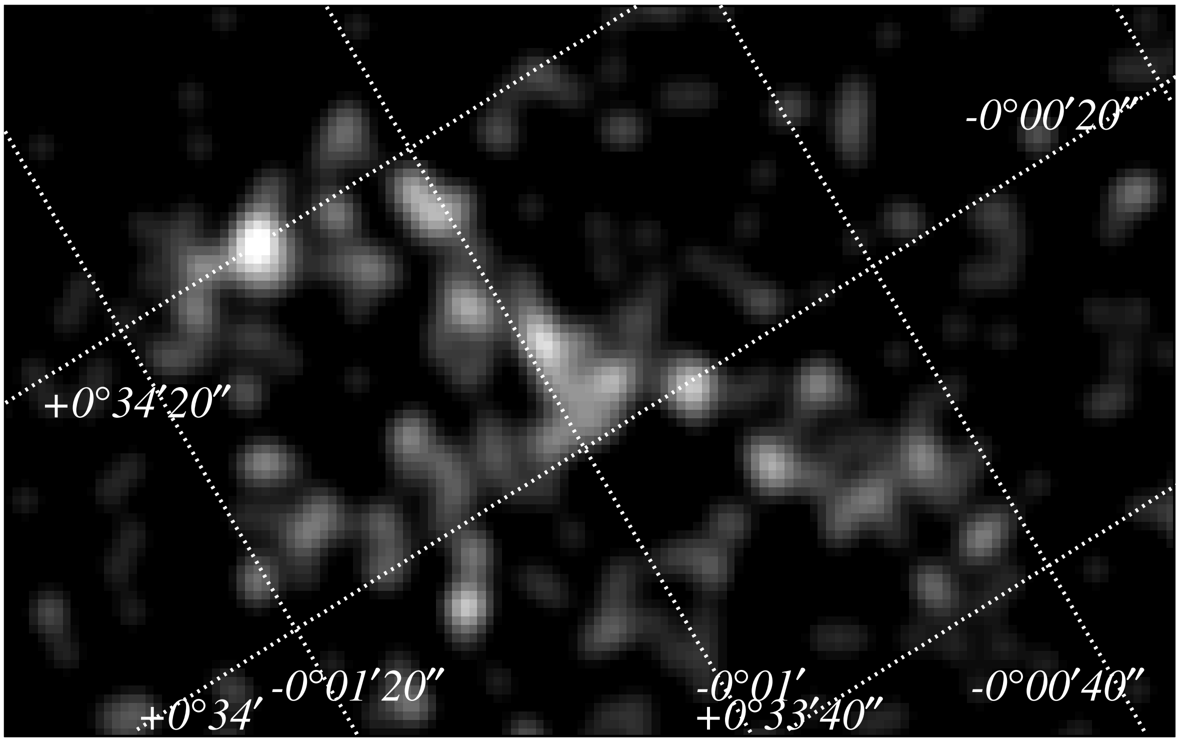

Figure 4.2: *Chandra* ACIS image of G0.570−0.018. The energy band is 4.0−7.0 keV. Gaussian smoothing of $\sigma = 2$ pixels is applied for the image.

Figure 4.3 shows the radial profile of the ring-like structure of G0.570−0.018 in the 4.0−7.0 keV band. The excess around $r \sim 10''$ is statistically significant, hence the ring-structure is real. On the other hand, a faint point-like structure at the shell center seen in Figure 4.2 is not significant because it contains only 3 photons. Unlike Sgr B2, no radio nor any other wave band counterpart is found for G0.570−0.018 (Oka et al., 1998a; Oka et ak., 1998b; Tsuboi et al., 1999; Lis & Carlstrom, 1994; Mehlinger et al., 1992, 1993; Seiradakis et al., 1989).

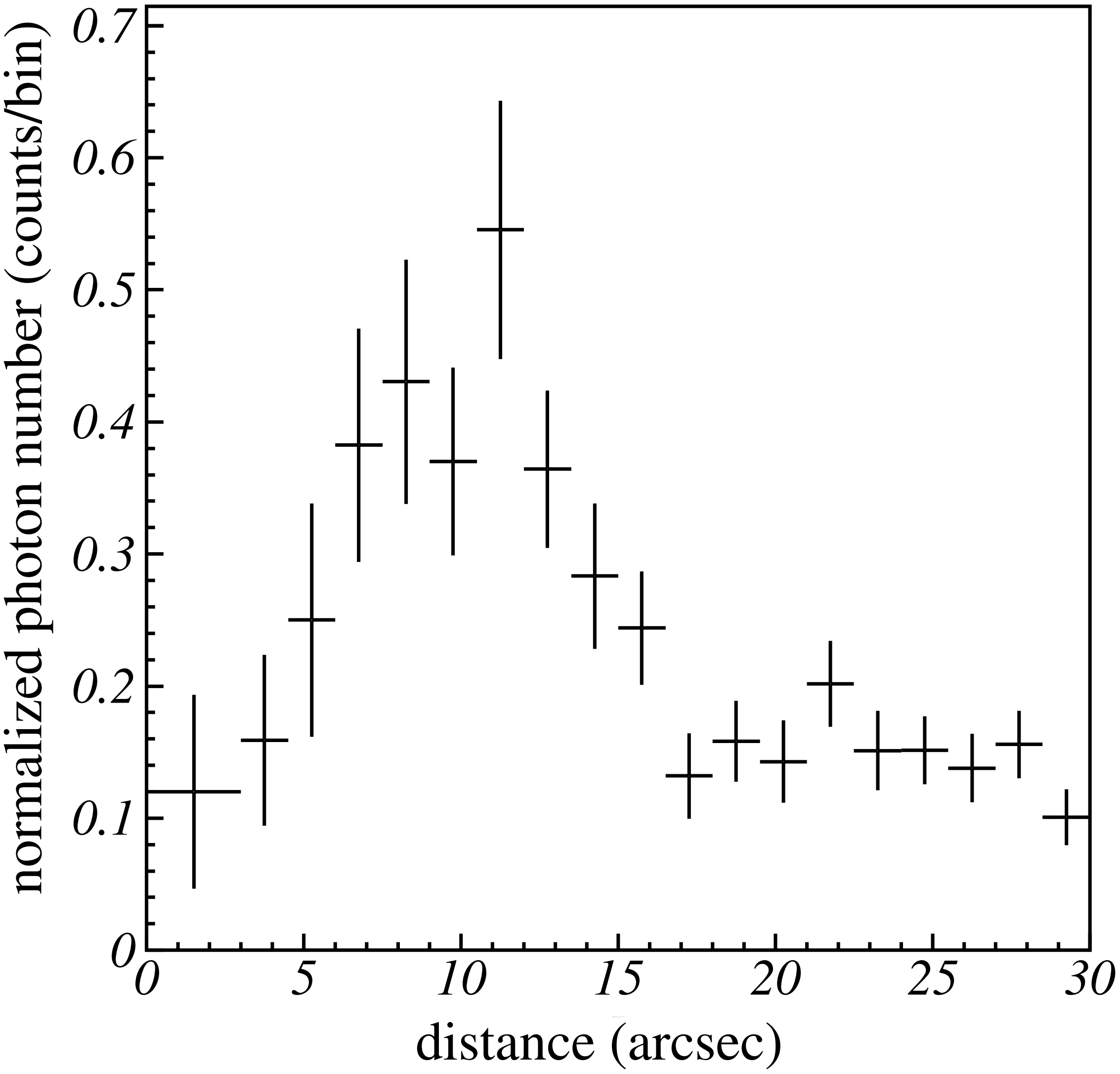

Figure 4.3: A radial profile of the ring-like structure of G0.570−0.018 resolved with *Chandra* ACIS. The center position of the profile is mentioned in the text.

4.1.3 X-ray spectra

The *ASCA* X-ray spectrum is made using the data in a circle of $3.0'$ radius and subtracting the background data in an annulus region of $3' < r < 4'$ as is shown in Figure 4.1. The spectrum exhibits prominent line at 6.0−7.0 keV and large absorption at low energy band. We then fit with a phenomenological model of a thermal bremsstrahlung plus a Gaussian line. The line energy is determined to be $6.60^{+0.12}_{-0.09}$ keV with an equivalent width of $3.7^{+3.0}_{-1.2}$ keV (here and after, errors are 90% confidence unless otherwise noted), indicating a K_α line from iron atoms with lower ionization states than helium-like (6.7 keV). An electron temperature is constrained to be higher than 2 keV. Therefore the equilibrium ionization state of iron should be helium or hydrogen like with the line energy of 6.7−6.9 keV. We thus conclude that the plasma is still in an ionizing phase or in a non-equilibrium ionization (NEI).

The *Chandra* X-ray spectrum is made from the same area as with *ASCA*, while the background spectrum is taken from a source-free region with the same CTI effect as the source region. The background-subtracted flux is 20400 counts and the spectrum shows a clear iron line as is already found with *ASCA*. In the diffuse source region, we also find many faint point-like sources. We hence execute the CIAO '*wavdetect*' software of a wavelet method (Freeman et al., 2002) and resolve 18 point sources. The integrated flux (2.0−10.0 keV) of all the point sources is 410 counts, which is only $\simeq 2\%$ of the diffuse X-rays. Therefore a contamination of the point-sources can be ignored practically. The *Chandra* spectrum is well fitted with the same phenomenological model as used for the *ASCA* spectrum, a bremsstrahlung plus a Gaussian line. The plasma temperature is constrained to be > 3.4 keV, while the line energy is $6.50^{+0.03}_{-0.03}$ keV with the equivalent width of $4.1^{+1.4}_{-1.0}$ keV. Thus the best-fit parameters are consistent with, and are more accurate than the *ASCA* results.

Since both the *ASCA* and *Chandra* spectra are fitted with the same model and the line center energy is consistent with an NEI plasma, we simultaneously fit the two spectra with a more realistic NEI plasma model (Borkowski et al., 2001). In addition to a conventional thin thermal plasma model, an NEI model includes another parameter, which is called the ionization parameter $\tau = nt$, where n and t are plasma density and elapsed time after the plasma is heated-up. As the parameter τ becomes larger than $10^{12} \sim 10^{13}$ cm^{-3} s, an NEI plasma approaches to a collisional ionization equilibrium (CIE) plasma. In addition to the strong iron line, the *Chandra* spectrum includes emission lines at the energies of K-shell transition of argon, calcium atoms. We

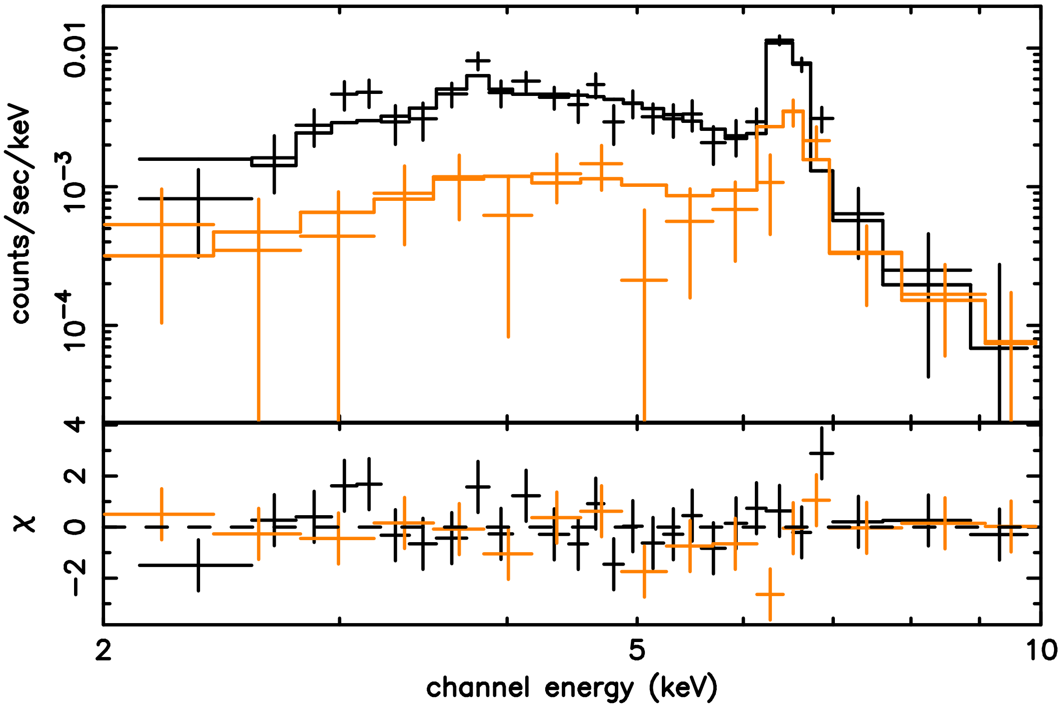

Figure 4.4: X-ray spectra of G0.570−0.018. Black crosses indicate the data point obtained with *Chandra*, while orange crosses indicate *ASCA* data.

Table 4.2: Best-fit parameters of G0.570−0.018 for NEI model obtained from the combined fitting of *ASCA* and *Chandra* spectra

Parameter	Unit	Value
kT	[keV]	6.1 (3.1–25.8)
Metal Abundances[a]	[solar]	4.5 (1.6–9.9)
$n_e t$	[cm^{-3} s]	1.7 (1.3–2.7) $\times$ 10^{10}
$N_{\rm H}$	[cm^{-2}]	13.9 (10.7–17.2) $\times$ 10^{22}
Flux[b]	[ergs cm^{-2} s^{-1}]	8.2 $\times$ 10^{-13}
Luminosity[c]	[ergs s^{-1}]	1.3 $\times$ 10^{34}
χ^2/d.o.f.	—	41.3/40

All the errors given in parentheses indicate the 90% confidence limits.
[a] Abundance ratio relative to the solar value (Anders & Grevesse, 1989).
[b] X-ray flux in 2.0–10 keV. Absorption is not corrected.
[c] The absorption corrected luminosity in 2.0−10 keV.

therefore vary the abundances of all the elements collectively fixing the relative ratio to be solar (Anders & Grevesse, 1989). Free parameters are the electron temperature (kT), the abundance (Z), the ionization parameter (nt), and interstellar absorption ($N_{\rm H}$). For the other free parameter, we allow one normalization factor to be fitted both the *ASCA* and *Chandra* fluxes simultaneously. The NEI fit is acceptable with the best-fit spectra and parameters shown in Figure 4.4 and Table 4.5. The data excess of *Chandra* and deficit of *ASCA* above and below the iron line are attributable to the gain uncertainty of these instruments. However this small systematic difference is not a serious problem in the present analysis. The ionization parameter of τ =1.7×10^{10} cm^{-3} s is very small, while the abundance is significantly larger than the solar value.

4.1.4 Physical parameters

ASCA discovered a diffuse X-ray source (G0.570−0.018) with a strong iron line near the Sgr B2 cloud, then *Chandra* found a ring-like structure of 10″-radius. The hydrogen column density is determined to be $N_{\rm H} = (13.9^{+3.3}_{-3.2}) \times 10^{22}$ H cm^{-2}.

Since the $N_{\rm H}$ value is nearly equal to those of the Galactic center sources of the same Galactic latitude (Sakano, 2000), G0.570−0.018 would be located near at the Galactic center region.

We hence assume the source distance to be 8.5 kpc. The X-ray luminosity is then estimated to be $\simeq 10^{34}$ ergs and the size of the ring radius is 0.4 pc. The spectra are well fitted with an NEI model with plasma temperature (kT) of 6.1 keV, ionization parameter (τ) of 1.7×10^{10} cm^{-3} s, and metal abundances (Z) of 4.5 solar. Therefore, together with the ring-like morphology, G0.570−0.018 is likely a young SNR, either in an adiabatic or a free expansion phase. We first apply a Sedov self-similar model assuming in an adiabatic phase. This model gives the emission measure ($E.M. = n^2V$), radius (R) and electron temperature (kT) as follows (Ostriker & McKee, 1988);

$$n^2V = 4\pi R^2(4n_{\rm a})^2(\frac{R}{12})\ [\mathrm{cm}^{-3}] \tag{4.1}$$

$$R = 5.0 \times (\frac{E}{10^{51}\ \mathrm{ergs}})^{1/5}(\frac{n_{\rm a}}{1\ \mathrm{cm}^{-3}})^{-1/5}(\frac{t_{\rm s}}{10^3\ \mathrm{years}})^{2/5}\ [\mathrm{pc}] \tag{4.2}$$

$$kT = 4.5 \times (\frac{E}{10^{51}\ \mathrm{ergs}})^{2/5}(\frac{n_{\rm a}}{1\ \mathrm{cm}^{-3}})^{-2/5}(\frac{t_{\rm s}}{10^3\ \mathrm{years}})^{-6/5}\ [\mathrm{keV}] \tag{4.3}$$

Where $t_{\rm s}$, $n_{\rm a}$ and E are the age of the plasma (in unit of year), ambient density (in units of cm^{-3}) and explosion energy of the supernova (in units of ergs), respectively. Using the observed values of $R = 0.4$ pc, $kT = 6.1$ keV and $E.M. = 8.1 \times 10^{56}$ cm^{-3}, we obtain t_s, n_a and E to be 70 years, 5.1 cm^{-3} and 3.5×10^{48} ergs, respectively. The swept-up mass is then calculated to be $n_{\rm a} \times 4/3\pi R^3 \simeq 0.03{\rm M}_\odot$, which is extremely smaller than that of the SN ejecta of a few M$_\odot$. The estimated explosion energy of G0.570−0.018 is also extremely small compared with a usual SNR. These indicate that only a tiny fraction of the explosion energy ($\sim 10^{51}$ ergs) and ejected mass (a few $\times M_\odot$) have been converted to the thermal plasma. These facts strongly indicate that G0.570−0.018 is not in an adiabatic phase but still in a free expansion phase.

4.1.5 The nature of G0.570−0.018

The X-ray ring structure of G0.570−0.018 is similar to that of SN 1987A (Burrows et al., 2000; Park et al,, 2002, 2004), where a strong stellar wind from a massive progenitor might produce a gas ring of sub-pc radius, and was heated by the collision of supernova ejecta. From the radial profile in Figure 4.3, the thickness of the ring (FWHM) is about 6″, or 0.2 pc, hence the plasma volume is 1.2×10^{55} cm^3. Since the X-ray flux from the ring is 67% of that of the whole area of G0.570−0.018, the emission measure ($E.M.$) from the ring is 5.5×10^{56} cm^{-3}. Then using the best-fit ionization parameter (nt) of 1.7×10^{10} cm^{-3} s, the plasma density (n) and ionization age (t) of the X-ray ring are estimated to be 6.7 cm^{-3} and 80 year, respectively. In Table 4.3, we compare the physical parameters of the ring of G0.570−0.018 with those of SN 1987A. The ring size and age are about 3−6 times larger than those of SN 1987A. Therefore G0.570−0.018 would be a "future SN 1987A" after a free expansion with the expected speed of $v = R/t \simeq 4900$ km s^{-1}.

Table 4.3: Comparison of the parameters between G0.570−0.018 and the X-ray remnant of SN 1987A

Source name	Distance [kpc]	Radius of X-ray shell [parsec]	Age [year]
G0.570−0.018	8.5	0.4	80
SN 1987A[a]	50	0.12	13

[a] The parameters are taken from Burrows et al. (2000).

One problem of this scenario for G0.570−0.018 is an additional X-ray structure, the east-to-west X-ray tail. We suspect that the structure would be made by some instability of dense stellar wind from progenitor, and was heated-up by the collision of the SN ejecta. In fact, the surface brightness of X-ray remnant of SN 1987A is not uniform and varying as time progresses (Figure 4.5). In this case, the front of free expanding ejecta would be about two times larger than the ring radius, hence the age of SNR is doubled. This age is still in a very young phase, thus the above discussion based on a free expansion phase is essentially not changed.

In the young SNR scenario, we expect nonthermal radio emissions associated with the thermal X-rays, However we see no significant radio continuum flux from G0.570−0.018. In general, if the X-ray emission is thermal origin, then the observed flux intensity is determined by the emissivity of the thermal bremsstrahlung. Hence X-ray flux is proportional to the square of electron density ($n_{\rm e}^2$), assuming that $n_{\rm e} \sim n_{\rm H}$. On the other hand, an intensity of radio continuum emission is determined by synchrotron emissivity, thus the flux density is proportional to the square of magnetic field, B^2. Assuming that magnetic field is proportional to the ambient gas density (the magnetic field is frozen to the ambient gas), the flux ratio between X-ray to radio is roughly constant among shell-like SNRs. Referring the radio and X-ray data of typical young shell-like SNRs, Cas A, Tycho and Kepler, we estimated the radio flux of G0.570−0.018 to be 0.1−1 Jy (except Cas A) at 1 GHz, using the X-ray flux of $\sim 10^{-12}$ ergs s^{-1}.

SN 1987A has almost the same X-ray flux as that of G0.570−0.018, and the radio flux density is ∼40 mJy at 4.7 GHz (Burrows et al., 2000). These radio flux density would be below the current detection limit of the radio SNRs located near the GC, where the radio background is extremely high (∼0.1−0.5 Jy). Thus we encourage more deep and fine spatial resolution search for radio emissions near at G0.570−0.018.

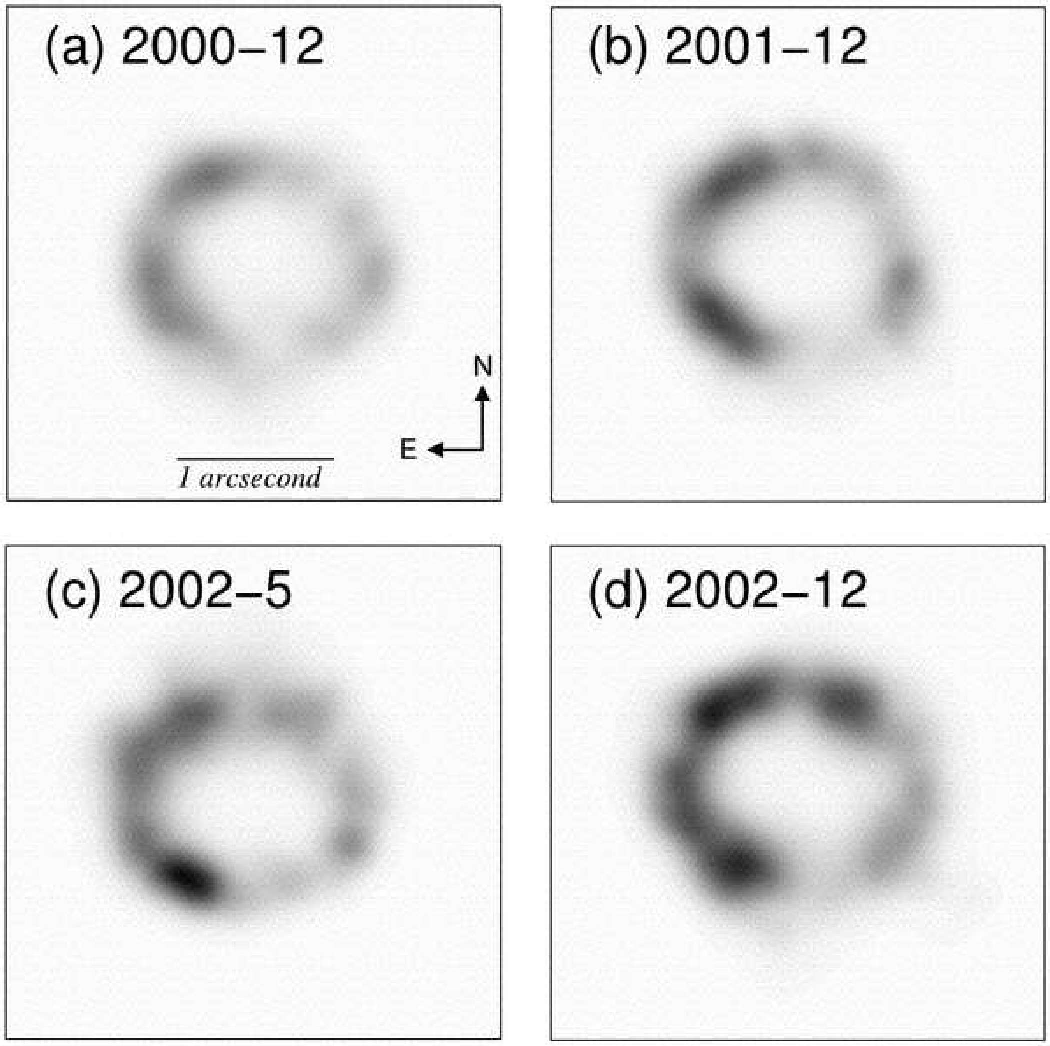

Figure 4.5: Morphological evolution of the X-ray remnant of SN 1987A from Dec. 2000 to Dec. 2002 with *Chandra*(Park et al,, 2004).

4.2 X-ray study of G359.8−0.3

4.2.1 Introduction

G359.8−0.3 is a nonthermal radio shell which is first detected at the 30 pc south of the Galactic center with the 10 GHz radio continuum survey performed by Nobeyama Radio Observatory (NRO) (Sofue , 1988). The diameter of the radio shell is about 30′ and it has a almost flat spectral index ($\alpha \sim 0.0$) at least between 5 to 10 GHz. Although a nature of the radio shell has been unclear, it is thought to be (1) extended HII region / stellar wind shell, (2) shell-type supernova remnant, or (3) a bubble structure caused by the Energetic activity of the GC.

Yusef-Zadeh et al. (1986) reported that jet-like structure emanating from the galactic nucleus with 160 MHz radio observation of Culgoora Circular Array. The low-frequency radio structure seems to lie along the rotation axis of the Galaxy and extend at least $\sim$ 30 pc toward negative galactic latitude. Sofue (1988) also claimed that the terminal point of the structure is coincide with G359.8−0.3 radio shell, hence the origin may have possible relation to the past activity of the nucleus of our Galaxy. From these radio continuum data only, however, it is impossible to further study of the source. X-ray observations should give crucial information as for the nature of G359.8−0.3.

4.2.2 Observations and data reductions

The western part of the G359.8−0.3 is covered with FOVs of *Chandra* observations, while the eastern part is covered with FOVs of *XMM-Newton*. Both observations have already performed and archived. We used two observations of the *Chandra* ACIS data which are the part of GC Survey (PI: Wang), and an observation of *XMM-Newton* EPIC data (PI: Turner). The detailed accounts of the each observation are shown in Table 4.4. Data acquisition from ACIS was made in timed-exposure faint mode with chip readout every 3.24 s. We carried out *Chandra* data reduction and analysis using *Chandra* Interactive analysis of Observations software package (CIAO; version 2.3). We used level 2 processed event file pipelined by Chandra X-ray Center.

From the *XMM-Newton* observation, we used and analyzed the EPIC data which consists of the two MOS cameras (Turner et al., 2001) and the pn camera (Struder et al., 2001). During the observation, Each camera was operated with full-frame mode and acquired with the medium filter and imaging mode. Tha Standard Analysis System (SAS version 5.4.1) was used for processing and analyzing the EPIC data. As a event list, we used pipe-line processing data distributed from ESA.

After performing high background periods rejection, total live time is amount to 8.3 ks, 7.7 ks, and 7.4 ks for MOS1, MOS2, and pn instrument, respectively. Moreover, we selected events with pixel pattern of 0−12 (single to quadruple) for MOS and 0−4 (single and double) for pn to the subsequent analysis.

Table 4.4: The observation log of G359.8−0.3

Obs. ID	Obs. Start Time (UT)	Nominal Point (Ra, Dec)$_{J2000}$	Exposure (sec)
Chandra/ACIS			
2282 (GCS13)	2001-07-18 11:13:58	17 46 22.90 -29 02 15.4	10625
2291 (GCS16)	2001-07-18 20:49:28	17 45 55.03 -29 12 15.1	10625
2293 (GCS17)	2001-07-19 00:01:18	17 45 09.10 -29 06 28.4	11118
2296 (GCS19)	2001-07-19 06:41:38	17 45 26.88 -29 22 33.6	11118
XMM-Newton/EPIC			
0112971001	2000-09-24 04:34:32	17 46 40.18 -29 13 12.7	17192

4.2.3 X-ray and radio morphology

With *Chandra* observations, an X-ray excess is clearly seen in the soft (1.5−4 keV) band. This can be resolved into two components. At the center of the Figure 4.6, diffuse emission is extended about 10′. On the other hand, there is another excess which is located in the south edge of the ACIS chip. Since it is on the edge of the FOV and its short exposure time, the *Chandra* observation could not determine whether this source is point-like or extended. Moreover, as shown in Figure 4.6, FOVs of *Chandra* GC survey covered the only western part of the radio shell of G359.8−0.3, hence an X-ray property of the eastern part cannot reveal with *Chandra* GC survey data. Fortunately, *XMM-Newton* EPIC Observation covered a complementary region as is shown in Figure 4.7.

Our analysis revealed that there is no significant X-ray excess seen in the eastern part of the radio shell. From the EPIC image (Figure 4.7, we also confirmed that the central excess has an extended feature while the southern excess is resolved into two point-like sources. From spectral analysis, we conclude that both of point sources is foreground object because the column densities of them are smaller than the expected value of GC source by factor 2−3. On the other hand, the observations of the both instruments (*Chandra* ACIS and *XMM-Newton* EPIC), the position of the central X-ray excess coincides with the center of radio 10 GHz continuum shell G359.8−0.3 reported by Sofue (1988). Figure 4.8 represents a X-ray photon intensity profile with reference to the peak position of X-ray surface brightness. Hereafter, we focused on analyzing the central excess and discussing its nature.

4.2.4 X-ray spectra

We extracted the spectra from the $6.8' \times 4.0'$ elliptical region of the X-ray north excess of the central radio shell. The background was taken from the same galactic latitude region. X-ray spectra obtained with *Chandra*/ACIS and *XMM-Newton*/EPIC are extracted from the same sky region to confirm the consistency of the result. The following spectral analyses are performed with XSPEC version 11.2.

Table 4.5: Best fit parameters of G359.8−0.3 for NEI and MEKAL model

Parameter	Unit	NEI	MEKAL
kT	(keV)	1.6 (1.3–1.9)	1.04 (0.98–1.11)
Abundance[a]	(solar)	1.0 (1.3–1.9)	1.3 (0.9–2.2)
$\log n_e t$	($\mathrm{cm^{-3}}$ s)	11.3 (11.1–11.5)	—
N_{H}	10^{22} ($\mathrm{cm^{-2}}$)	4.4 (4.1–4.7)	4.6 (4.3–4.8)
flux[b]	(ergs $\mathrm{cm^{-2}\ s^{-1}}$)	1.8×10^{-12}	1.6×10^{-12}
L_{x}^{c}	(ergs $\mathrm{s^{-1}}$)	1.6×10^{35}	2.6×10^{35}
χ^2/d.o.f.	—	204.0/181	220.4/182

All the errors given in parentheses indicate the 90% confidence limits.
[a] Abundance ratio relative to the solar value (Anders & Grevesse, 1989).
[b] X-ray flux in 0.5–10 keV. Absorption is not corrected.
[c] The absorption corrected luminosity in 0.5−10 keV, assuming a source distance of 8.0 kpc. (McNamara et al., 2000).

To check the consistency between *Chandra* ACIS and and *XMM-Newton* EPIC, we fitted them with a same physical model. We at first tried to reproduce the spectral data with a model of thermal plasma in collisional equilibrium (MEKAL; Mewe et al. (1985, 1986); Kaastra (1992); Liedehl et al. (1995)), but it could not yield an acceptable fit ($\chi^2/dof = 220.3/182$). Therefore we fitted the combined spectra with a single

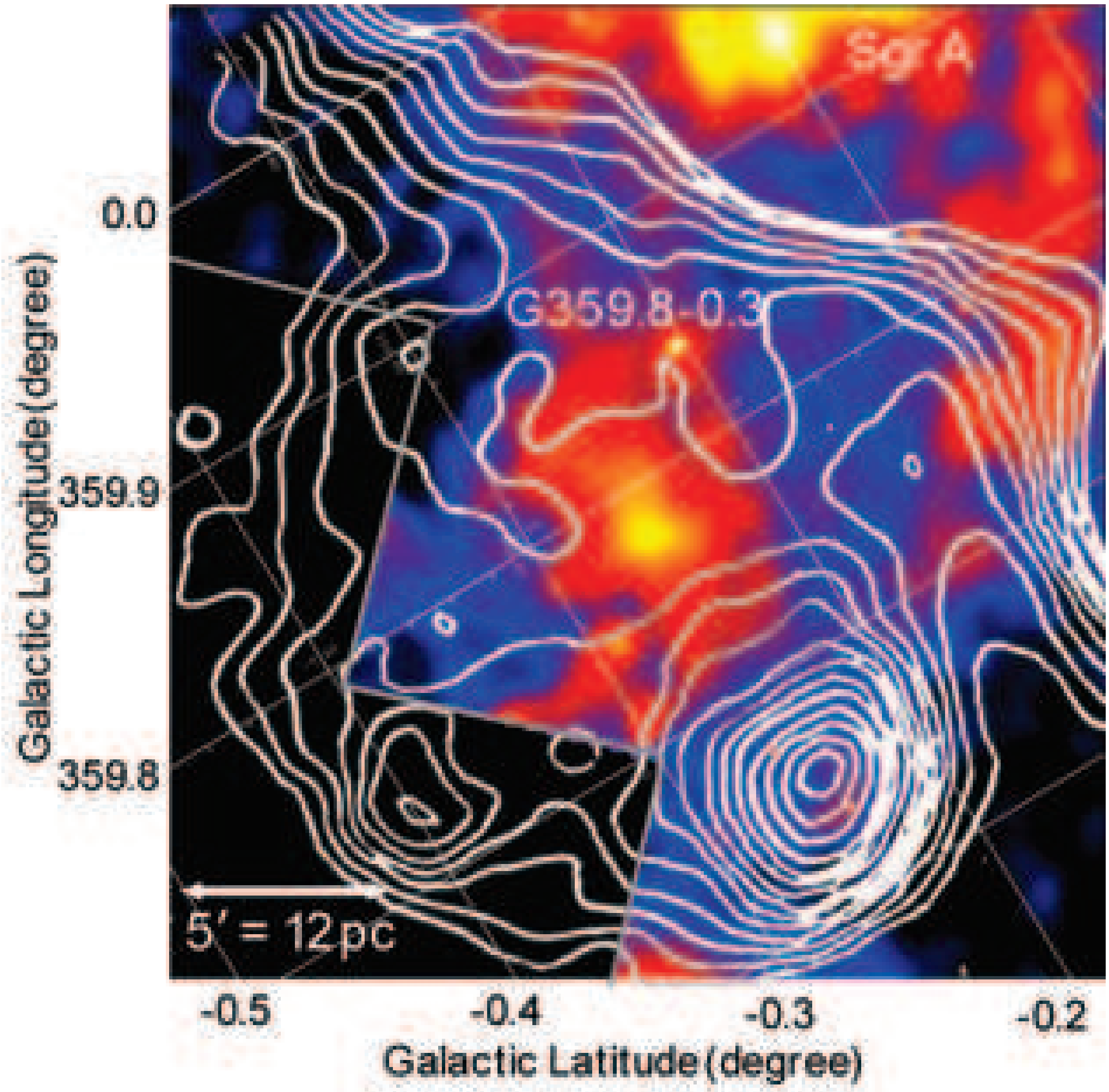

Figure 4.6: *Chandra* ACIS image of G359.8−0.3 (color map) with logarithmic scale. 1.5−4.0 keV photons are accumulated to construct the image. A solid gray zigzag line indicate the boundary of ACIS CCDs. White Contours indicate intensity of 10 cm radio continuum emission obtained with Nobeyama Radio Observatory (NRO).

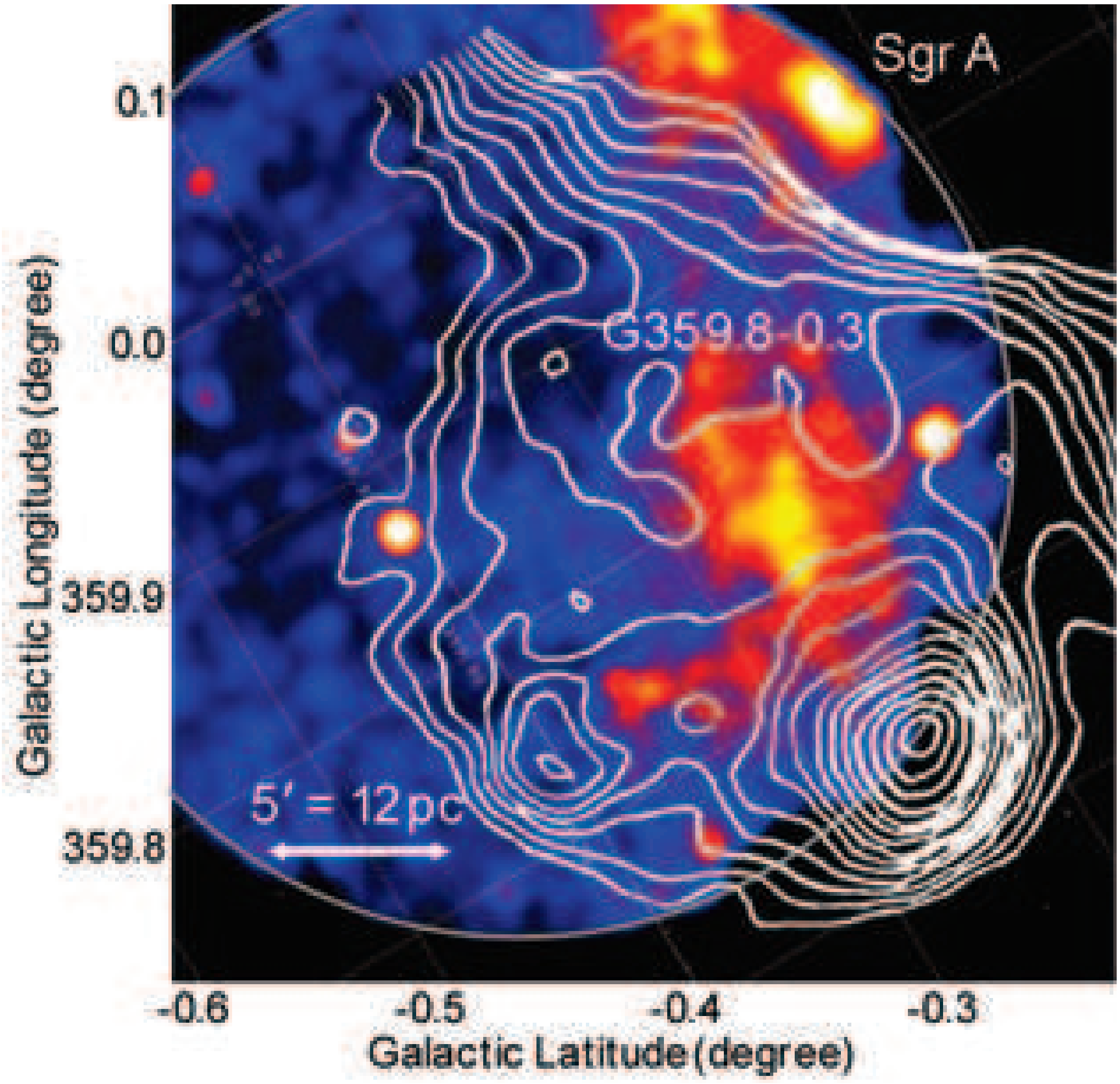

Figure 4.7: *XMM-Newton* EPIC image of G359.8−0.3 (color map) with logarithmic scale. X-ray photons detected from MOS1a MOS2 and pn detector are all combined to construct the image. Exposure and vignetting effect are collected. A solid gray circle indicates FOV of X-ray mirror of *XMM-Newton*. White Contours indicate intensity of radio 10 cm continuum emission obtained with NRO.

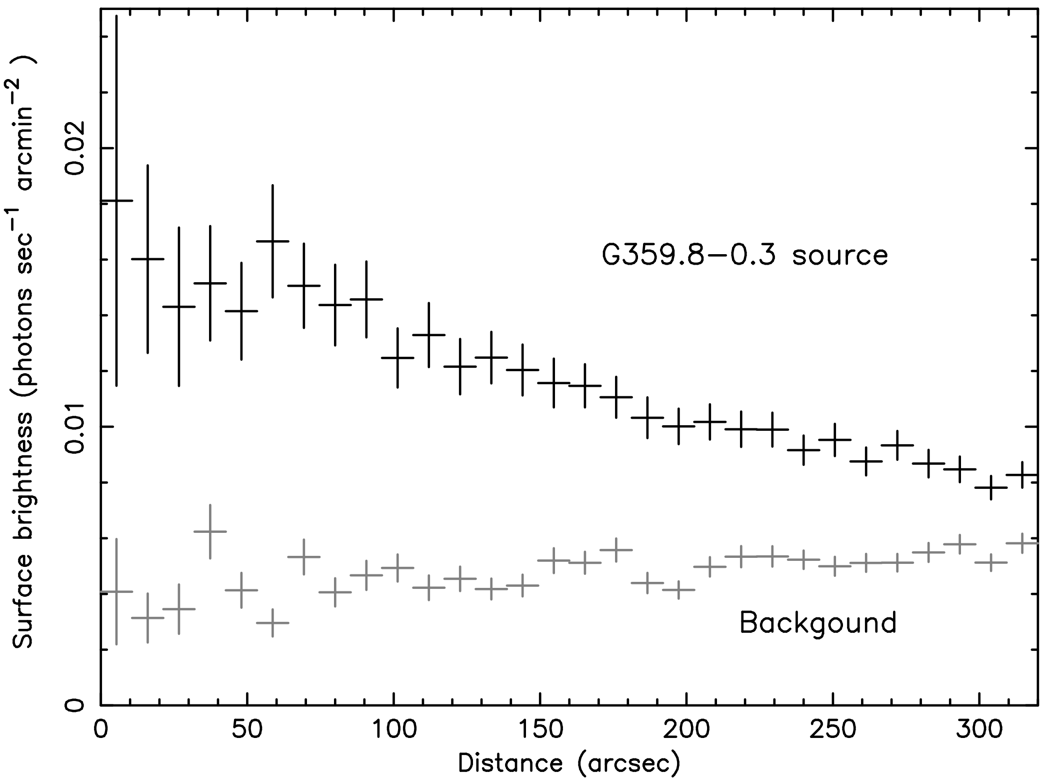

Figure 4.8: A radial profile of G359.8−0.3 obtained with *XMM-Newton* EPIC. 1.5−4.0 keV X-ray Photons accumulated with MOS and pn detectors are used to draw the profile. Exposure and vignetting effect are collected. Center position of the profile is at the peak point of the X-ray excess.

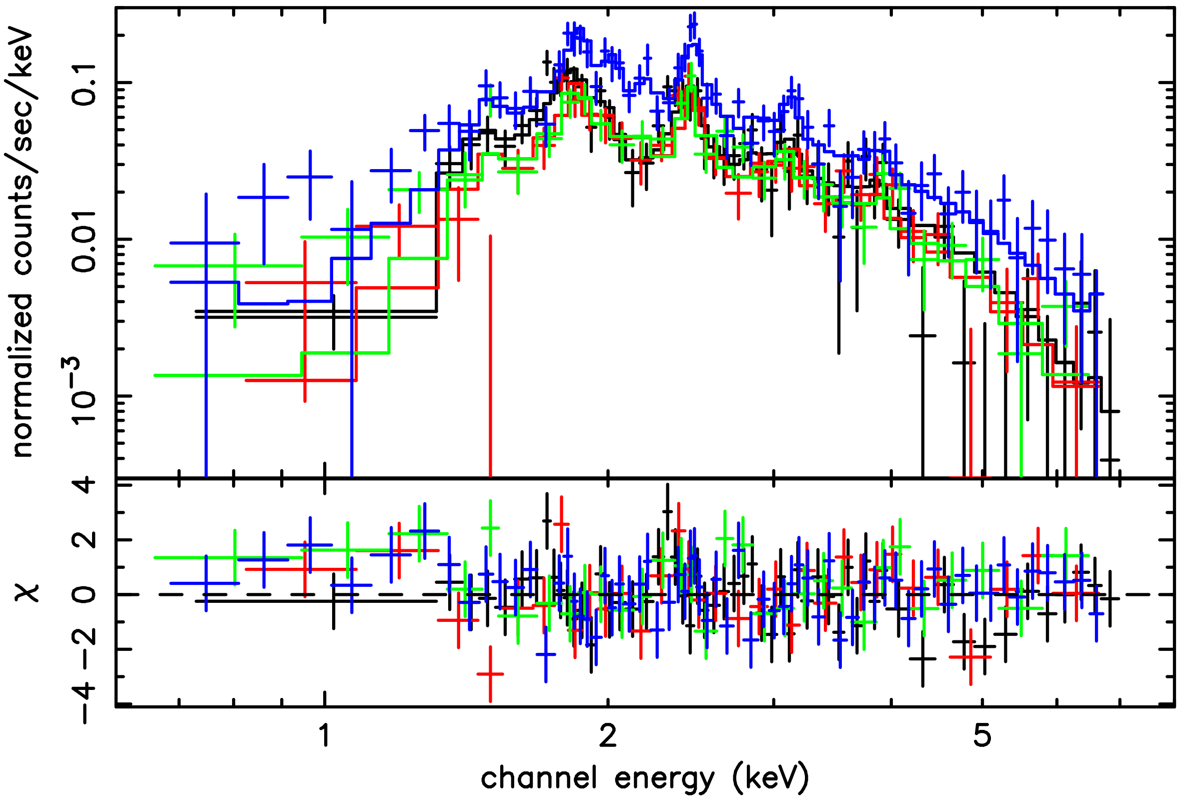

Figure 4.9: Upper panel: The X-ray spectrum extracted from the central region of G359.8−0.3. Black, red, blue, and green crosses represent data points obtained with *Chandra* ACIS, *XMM-Newton* EPIC MOS1, MOS2, and pn detector, respectively. Parameters of the Fitting model (NEI) are fixed to the same value for all data. The best-fit model is shown in solid lines. Lower panel: Residuals from the best-fit model.

temperature NEI model convolved with interstellar absorption. For the NEI model, we adopted the model version of 2.0 in *XSPEC*, which takes the emission lines from argon into account.

As a result, single-temperature thin-thermal NEI model with $kT \sim 1.6$ keV could well reproduced the combined X-ray spectra. The combined X-ray spectra obtained with *Chandra* and *XMM-Newton* and best-fit NEI model is shown in Figure 4.9. Best-fit parameters of the NEI model is shown in Table 4.5. The sufficiently large absorption column ($N_{\rm H} \sim 4 \times 10^{22}$ H cm^{-2}) indicated that G359.8−0.3 is located at the distance of the GC($D \sim$ 8.0 kpc; McNamara et al. (2000)). The value of NEI parameter is smaller than 10^{12} s cm^{-3}, by about an order of magnitude, which suggested that the plasma is not still reached thermal equilibrium.

4.2.5 The nature of G359.8−0.3

From the best fit value of an ionization parameter (log $nt \sim 11.3$ [cm s^{-1}]), and an emission measure ($n_{\rm H} n_{\rm e} V \sim 6.7 \times 10^{57}$ cm^{-3}), we estimated an electron density ($n_{\rm e}$) and an age (t) of the X-ray emitting plasma to be 0.5 cm^{-3} and 1.3×10^4 year, respectively. We assumed a density of Hydrogen ion is equal to that of an electron ($n_{\rm H} = n_{\rm e}$) and a shape of X-ray emitting plasma is spherical with a diameter of the source extracting region. The total thermal energy which is radiated by X-rays is estimated to be $E_{\rm thermal} = 3 n_{\rm e} k T_{\rm e} V \sim 1 \times 10^{50}$ ergs. Total mass of the X-ray gas was also determined to be $M = 1.4 m_{\rm H} n V \sim 16\ M_{\odot}$.

The morphology of G359.8−0.3; a shell-like structure in radio and the center-filled in X-rays, reminds us of the "Mixed-Morphology" SNRs (MMSNRs) proposed by Rho & Petre (1998). They pointed out common characteristics of MMSNRs as follows; (1) shell-like structure in radio band, (2) filled-center structure in X-rays, and (3) absence of a compact source in its center. The Radio and X-ray properties of G359.8−0.3 satisfy all of their criteria. In addition, the X-ray spectra of MMSNRs show thermal feature with several emission lines, which means the X-ray emission process is essentially different from the case of Crab-like . Thermal X-ray spectrum of G359.8−0.3 is also consistent with the MMSNR interpretation.

Table 4.6: Comparison between G359.8−0.3 and other MM SNRs near the Galactic center region

Parameter	Unit	G359.8-0.3	Sgr A East[a]	G359.1-0.5[a]
Size (radio shell)	(arcmin)	21 × 21	3.5 × 2.5	24 × 24
Size (X-ray)	arcmin	6.8 × 4.0	1.3 × 1.3	12 × 12
$N_{\rm H}$	10^{22} ($\rm cm^{-2}$)	4.4 (4.1–4.7)	11.4 (10.5–12.3)	5.9 (4.1–8.4)
kT_e	(keV)	1.6 (1.3–1.9)	2.1 (1.9–2.4)	0.6 (0.4–0.9) 4.4(2.2–13.2)[d]
X-ray flux[b]	(ergs $\rm cm^{-2}\ s^{-1}$)	1.8×10^{-12}	1.6×10^{-12}	1.4×10^{-12} [c]
n_e	($\rm cm^{-3}$)	0.5	6	0.5
t	(year)	1.3×10^4	1.0×10^4	1.8×10^4
E_{th}	(ergs)	1.0×10^{50}	2×10^{49}	

All the errors given in parentheses indicate the 90% confidence limits.
[a] Values are quoted from Maeda et al. (2002) for Sgr A East, and Bamba et al. (2000) for G359.1−0.5, respectively.
[b] X-ray flux in 0.5–10 keV. Absorption is not corrected.
[c] 0.7–10 keV flux. [d] Two thermal components (Bamba et al., 2000).

4.2.6 Distance of G359.8−0.3

So far, 231 Galactic SNRs are discovered in the all sky (Green, 2004). At least 8% of all Galactic SNRs and as much as 25% of X-ray-detected Galactic SNRs are possible MMSNRs (Rho & Petre, 1998). On the other hand,four SNRs were discovered within a central degree of the Galaxy (G359.1-0.5, Sgr A East, G0.3+0.0, and G0.9+0.0), three of them are detected with X-rays, and two of them (G359.1-0.5 and Sgr A East) are identified as MMSNRs. Table 4.2.5 shows a physical quantities of G359.8−0.3 derived from X-ray observations with applying MMSNR interpretation and compare them to that of the other MMSNRs located near the GC region.

On the other hand, Sofue (1988) reported that a radio spectral index of G359.8−0.3 is almost flat ($\alpha \sim 0.0$) at least between 5 to 10 GHz. Assuming the same spectral index can be extrapolated to the lower frequency band, an 1 GHz surface brightness of G359.8−0.3 is estimated to be $\Sigma_{\rm 1GHz} \sim 6 \times 10^{-21}$ W $\rm m^{-2}$ $\rm Hz^{-1}$ $\rm str^{-1}$. By applying $\Sigma - D$ relation (Case & Bhattacharya, 1998), a distance of G359.8−0.3 is determined to $D \sim 5$ kpc. The value is rather smaller than the distance of the GC (8.0 kpc). However, the uncertainty of the source distance derived from the $\Sigma - D$ relation is rather large, typically ~ 3 kpc, hence it is not inconsistent with our estimation of the distance We conclude that G359.8−0.3 is located at the distance of the GC.

Chapter 5

Nonthermal Structures in the GC region

Thanks to the high spatial resolution and good photon statistics of *Chandra* deep exposure observations, we have successfully resolved detailed diffuse structures at the central $17' \times 17'$ (40 pc $\times$ 40 pc) of the Galaxy for the first time. In this chapter, we focus on the nonthermal features located in the inner 20 parsecs of the Galactic center; Jet-like structure ejected from the Galactic nucleus (Section 5.2), Outflows in the southeast direction of Sgr A* (Section 5.3), A complex system of nonthermal–6.4-keV fluorescent clumps which we named "Fishhook" (Section 5.4), and a number of other nonthermal features (Section 5.5).

5.1 Observations and Data Reductions

To extract the results presented in the following sections, we use eleven *Chandra* ACIS-I observations as shown in Table 5.1 except for the observation of Obs.ID 1561b because the data is suffered from the contamination of the bright X-ray transient (probably GRS 1741.9−2853 (Pavlinsky et al., 1994)). All of these observations were performed in Timed-Exposure Faint mode except for Obs ID=242, which was worked on Timed-Exposure Very Faint mode.

The data reduction and analyses were performed on the platform of the *Chandra* Interactive Analysis of Observations (CIAO)[1].

We start to retrieve level=1 event files of the each observation provided by *Chandra* X-ray Center (CXC) to create level=2 event list of each data. Our data reduction process is as follows. First, we run the standard processing pipeline of *acis_process_events*

[1] http://cxc.harvard.edu/ciao/

then correct CTI and time dependency of the gain. Second, we select the events of *ASCA* 02346 grade as X-ray events. Third, we examined background particle flaring time, and excluded the flaring intervals. Finally, we obtain level=2 event list of each data with its effective exposure time is shown in Table 5.1.

Table 5.1: The observation log of the GC deep exposure with *Chandra*

Obs. ID	Obs. start time (UT)	Nominal point (Ra, Dec)$_{J2000}$	Exposure[a] (sec)
242	1999-09-21 02:43:00	17 45 39.32 -29 00 46.8	45923
1561a	2000-10-26 18:15:11	17 45 39.22 -29 00 46.1	35705
1561b	2001-07-14 01:51:10	17 45 39.22 -29 00 46.1	13504
2943	2002-05-22 12:25:04	17 45 40.78 -29 00 14.6	37978
2951	2002-02-19 14:27:32	17 45 40.48 -29 00 12.1	12370
2952	2002-03-23 12:25:04	17 45 40.55 -29 00 12.4	11859
2953	2002-04-19 10:39:01	17 45 40.61 -29 00 12.6	11785
2954	2002-05-07 09:25:07	17 45 40.65 -29 00 13.5	12455
3392	2002-05-25 15:16:03	17 45 40.78 -29 00 14.7	166691
3393	2002-05-28 05:34:44	17 45 40.78 -29 00 14.6	158026
3663	2002-05-24 11:50:13	17 45 40.78 -29 00 14.6	37959
3665	2002-06-03 01:24:37	17 45 40.78 -29 00 14.7	89928

[a] Effective exposure time after the GTI filtering is applied.

Figure 5.1 represents the spatial distribution of thermal and nonthermal diffuse components within central $17' \times 17'$ (40 pc $\times$ 40 pc) of our Galaxy. The procedures for constructing the "three-color" X-ray image is described below.

At first, we combined eleven level=2 event files made above analyses with reference to the position of Sgr A* (R.A.$_{J2000}$ = $17^h 45^m\ 40^s.0409$, Dec.$_{J2000}$ = $-29^\circ\ 00'\ 28''.118$, according to Reid et al. (1999)). Since we improved astrometry by correcting the known offset reported by CXC[2], a positional error should be smaller than $1''$. The total effective exposure of the combined event file is amount to 598 ksec.

Second, we run the point source searching script *wevdetect* (Freeman et al., 2002), which is designed on the basis of wavelet method. The searching wavelet radii are set to 1, $\sqrt{2}$, $2\sqrt{2}$, 4, $4\sqrt{2}$ pixels and the significance threshold was fixed to 10^{-7}. As the result, 1557 X-ray point sources are detected in the 0.5−8.0 keV band.

Third, we sliced the "hole-filled" event file into three different energy bands, then smoothed each image. We selected three energy band for constructing "three-color"

[2] http://cxc.harvard.edu/ciao/threads/arcsec_correction/

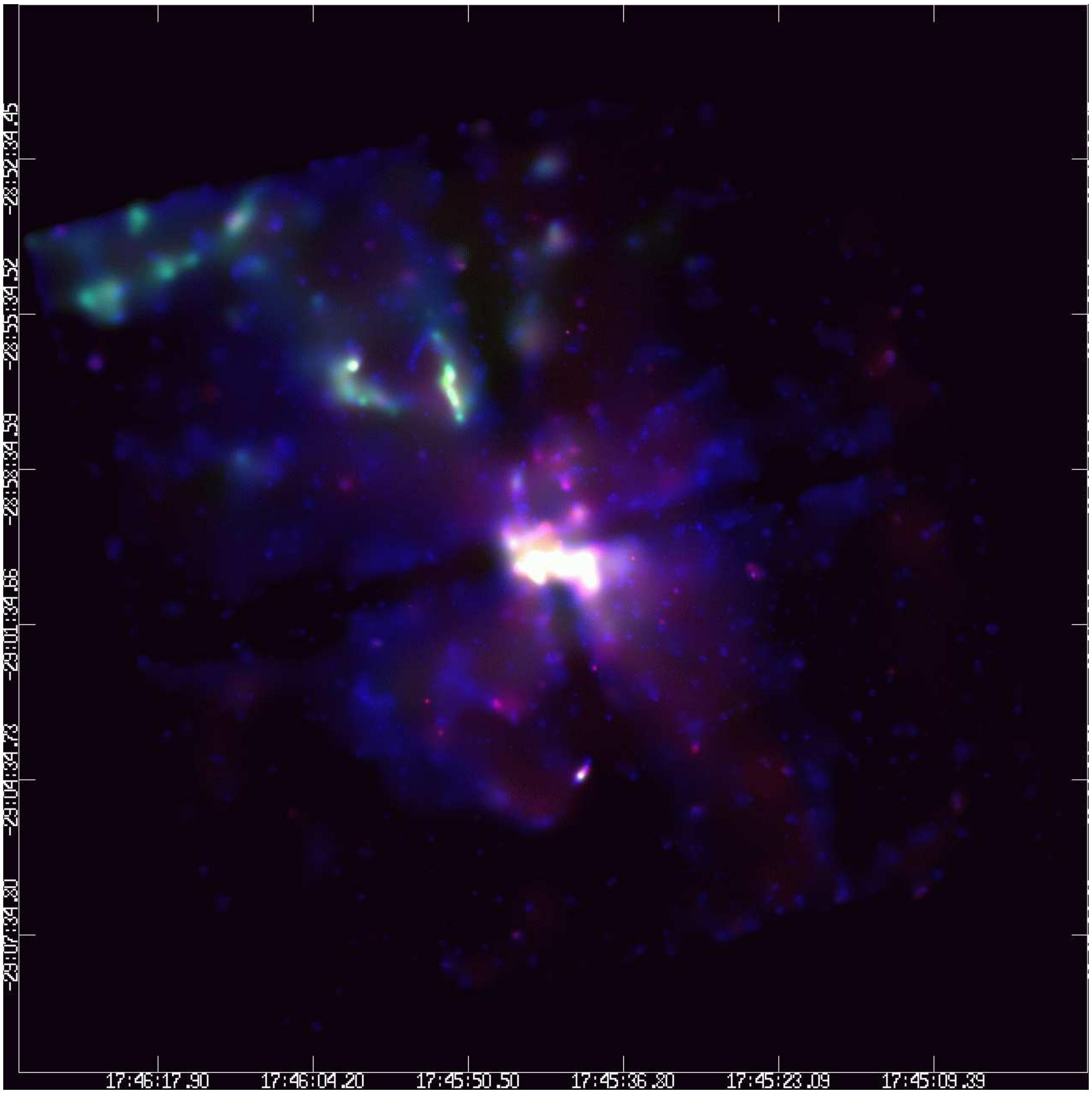

Figure 5.1: Three-color image of the central $17' \times 17'$ region of our Galaxy with *Chandra* ACIS. Red (6.50−7.07 keV) represents hot plasma components, Green (6.30−6.50 keV) represents fluorescent emission from neutral Fe-Kα, and Blue (3.42−6.30 keV) represents continuum-dominated emission. Point sources are removed then the holes are filled with an extrapolation of nearby emission.

image; 3.42−6.30 keV, 6.30−6.50 keV, and 6.50−7.07 keV. The highest and middle energy band contains, He/H-like and neutral Fe-Kα line, respectively. Therefore, the highest band image should represent emission from hot plasma, while the middle band image should trace the cold matter distribution, such as X-ray reflection nebulae reported by Murakami et al. (2000, 2001a,b). On the other hand, no significant emission lines exists within the lowest energy band, hence, only in the band, it is possible for faint nonthermal emissions to dominates without being distracted by thermal emission lines. An image smoothing is performed in order to make diffuse features visible clearly. Before the smoothing process, we removed the all point sources detected from the merged image file. The excluding region for each point source is an ellipse. As a center coordinate and major/minor radii of the excluding region, we applied the peak position and three-sigma width which was determined by a two-dimensional gaussian fitting for the profile of each detected point source. Then, we filled the hole of each excluded region with an extrapolation of the X-ray emission around the region. After these procedure, the "hole-filled" image was adaptively smoothed by *csmooth* routine. Minimum and maximum S/N ratio of the signal under the kernel are set to 3 and 5 sigma, respectively.

Finally, we merged three different energy band images which were adaptively smoothed into the composite three-color image shown in Figure 5.1.

5.2 Jet-like Structures

In Figure 5.1, we can see diffuse hot gas represented by red color, which seems pervade around the Galactic center region. In addition, a number of small scale X-ray features shown in blue color are resolved elsewhere. Among them, in this section, we focused on three X-ray linear structures running out from the GC to the north-northwest direction.

Figure 5.2 gives the close up X-ray view of the northwest region of the Galactic center. The image size is $3.4' \times 4.1'$ and the selected energy band is 3.0–8.0 keV. To construct the image, we merged eleven *Chandra* ACIS-I data sets same as Figure 5.1 Then an adaptive smoothing and a correction for exposure variations were performed.

We identify three prominent features in Figure 5.2 (marked them as knot 1, 2, and 3). Knot 1, 2, and 3 are not only on the straight line (described as the dashed-line of Figure 5.2), but also elongated to the same direction of the line. In addition, Their angular scale is almost the same with major and minor axes of $\sim 6''$ and $\sim 1.5''$, respectively.

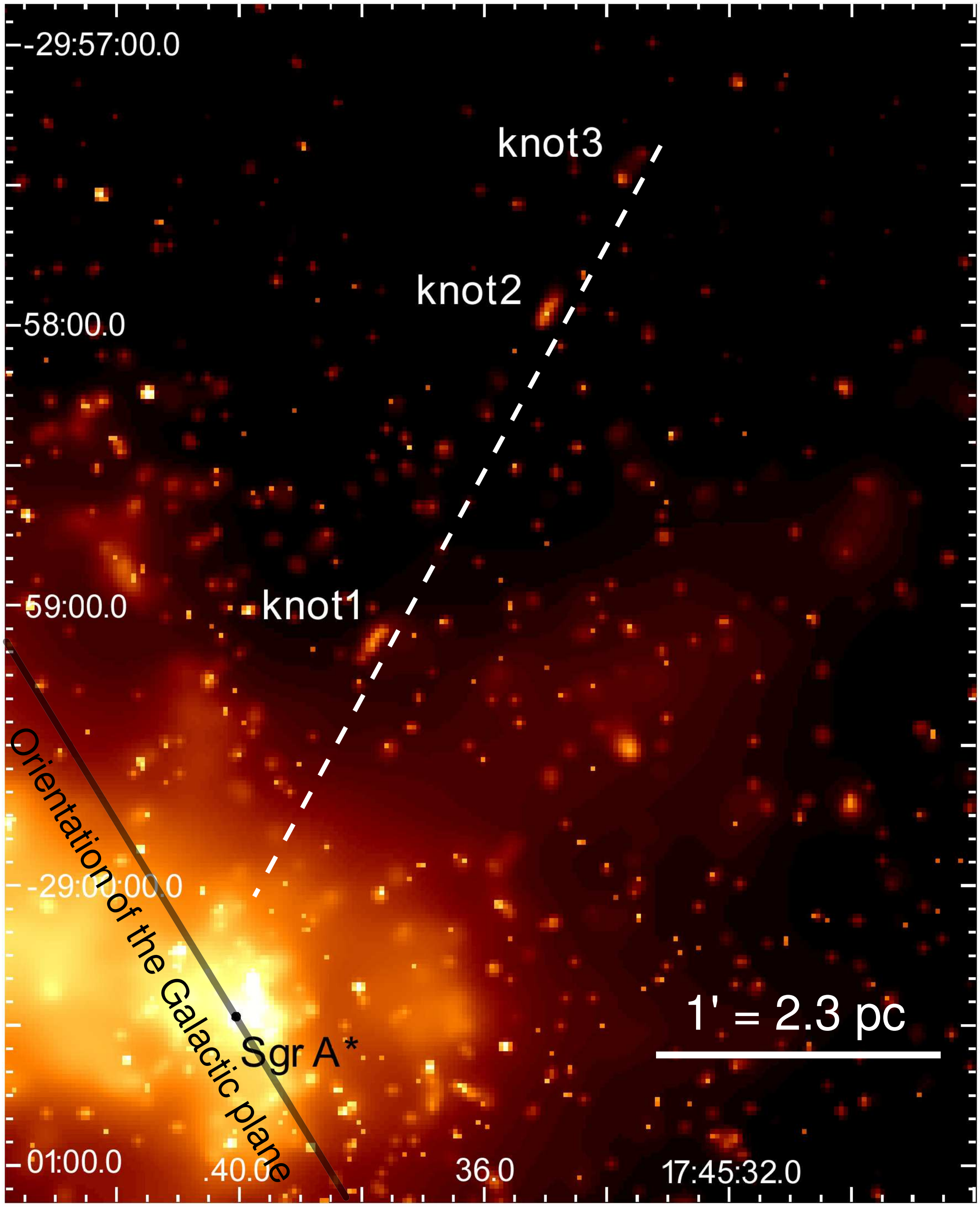

Figure 5.2: An adaptively smoothed 3.0−8.0 keV image of the northwest region of the Galactic center with *Chandra* ACIS. An adaptive smoothing and a correction for exposure variations were performed.

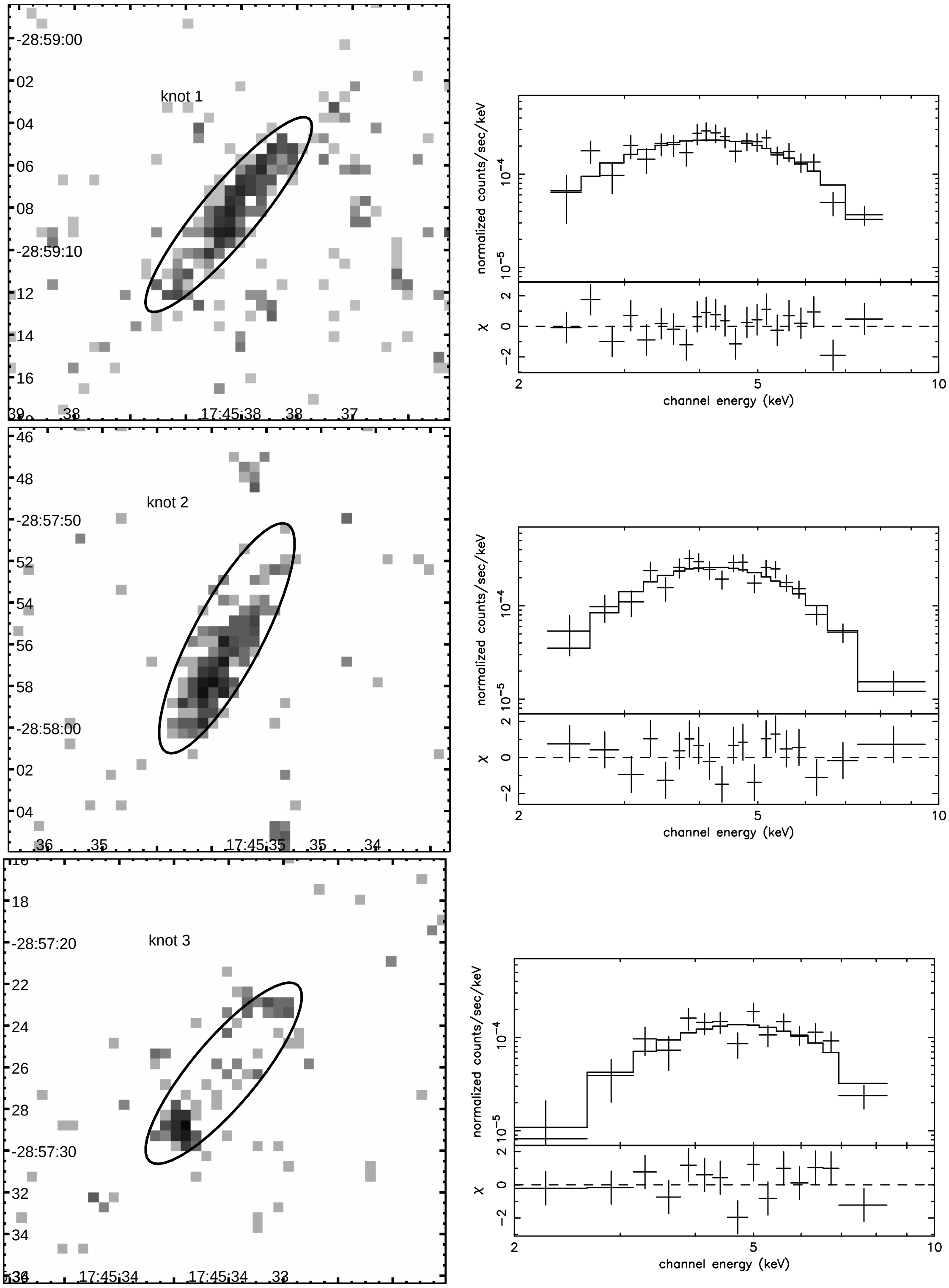

Figure 5.3: X-ray images (left panels) and spectra (right panels) of the jet-like structures (knot 1–3) with *Chandra* ACIS. Left panels: The images shows 3.0–8.0 keV X-ray photons from 3 to 300 count par pixel with a logarithmic scale. All of detected point source is excluded from the image. Right panels: Source photons of each spectrum (solid crosses) within the solid elliptical region shown in the corresponding left panel. Solid line represents the best-fit power-law model with ISM absorption. Parameters are shown in Table 5.2.

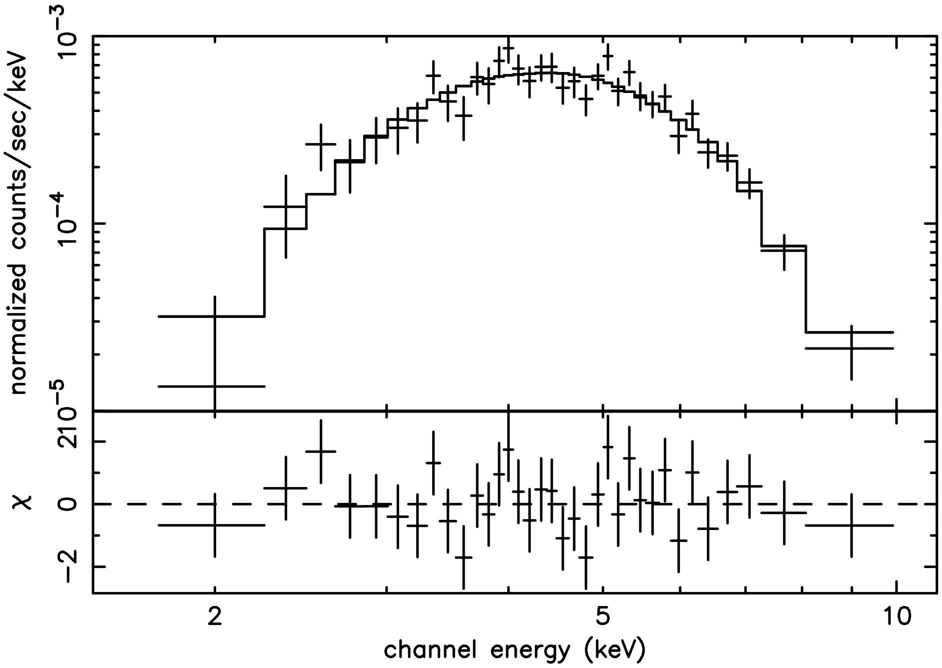

Figure 5.4: Merged X-ray spectrum of knot1–3. The best-fit power-law model convolved with interstellar absorption is given in solid line. The best-fit parameters are shown in Table 5.2.

5.2.1 X-ray spectra

As a source region for spectral analyses of knot1–3, we applied elliptical region along the enhancement of each knot as shown in left panels of Figure 5.3. While background photons of each knot are extracted from surrounding con-central elliptical annular region whose minimum and maximum radii correspond with 1 and 3 times of that of source ellipse. To avoid contaminations by point sources, all of the point source region were eliminated beforehand.

The background-subtracted spectrum presented in the right panels of Figure 5.3 exhibits no emission lines. Hence, we fitted the X-ray spectrum of each knot with a power-law model convolved with the effect of interstellar absorption. Best-fit parameters are shown in Table 5.2. Then we made the merged X-ray spectrum of three knots (as shown in Figure 5.4) then performed fitting with the same model. The result shows a beautiful power-law profile with a photon index of ~ 1.5 (Table 5.2). Although we tried fitting each spectra with a thin-thermal plasma model (MEKAL model; Mewe et al. (1985, 1986); Kaastra (1992); Liedehl et al. (1995)), best-fit value of a plasma temperature was determined to be > 70 keV, which is too high for the temperature of a thermal plasma. Therefore we thought that the application of a thermal model is not realistic. The best-fit column density of each knot exhibit almost same value of $N_{\rm H} \sim 1.0 \times 10^{23}$ cm^{-2}, which is consistent with the value when they are located at the distance of GC. The possibility that these knots are foreground object is robustly rejected. These results lead us to conclude that knot 1–3 are a nonthermal X-ray sources located near the Galactic center. Moreover, not only column density, but the photon index of each knot exhibits almost same value (Table 5.2). These spectral properties support the idea that they should have the same origin, which is already inferred from the linear alignment of them.

5.2.2 Radio counterparts

As shown in a dashed line of Figure 5.2, we can see three X-ray knots are aligned with a straight line from the direction of the Galactic center to north-northeast direction. Assuming that X-ray emission of the knots is nonthermal origin, the existence of synchrotron radio emission is also expected. Therefore we try to comparing X-ray and radio continuum intensity map. The result are given in Figure 5.5. The 6 cm and 20 cm radio contour maps are created from VLA archival data taken from NCSA/ADIL [3].

[3] http://adil.ncsa.uiuc.edu/

Table 5.2: Best fit parameters for the straight-line X-ray knots fitted with a power-law model

	Source Counts photons	Column Density ($N_{\rm H}$) 10^{22} H cm^{-2}	Photon Index (Γ) $N(E) \propto E^{-\Gamma}$	X-ray flux ^{a} ergs cm^{-2} s^{-1}
knot 1	501	8.5 (4.3–14)	1.3 (0.3–2.2)	4.1×10^{-14}
knot 2	485	16 (9.1–21)	2.3 (1.7–3.1)	3.4×10^{-14}
knot 3	295	10 (5.3–23)	1.8 (0.3–2.7)	3.8×10^{-14}
merged	1281	12 (9.5–15)	1.5 (1.1–2.0)	1.0×10^{-13}

All the errors given in parentheses indicate the 90% confidence limits.
[a] An absorbed X-ray flux of 2−10 keV.

Both X-ray color and radio contours are shown in logarithmic scale. Note that the 20 cm contour map around Sgr A* is saturated.

6 cm radio continuum counterparts were found at the position of the knot 1−3. Although knot 2 and 3 have only marginal counterparts in the radio band, knot 1 has a clear correlation between X-ray and radio continuum (both 6 cm and 20 cm; Figure 5.5).

Interestingly, when the alignment of the knots extrapolates toward the direction of the GC, it is smoothly connected to the "northern arm" of the radio structure called Sgr A West, which is comprised of three spiral-like arm features (Seen in the left panel of Figure 5.5). In projection, Sgr A* is located near the intersection of the three "arms" extended to east, west, and north directions. These arms consist of ionized gas, which exhibits emission lines in the radio and infrared bands (Ekers et al., 1983). Recent measurements of both proper motion in the continuum band and radial velocity in the H92α radio recombination line suggest that ionized gas of "northern arm" has a large variation in the velocity distribution which cannot be expected from Keplerian motion. This means that the "northern arm" is not bound to the gravitational potential of the Galactic nucleus (Yusef-Zadeh et al., 1998; Yusef-Zadeh, 2000).

Although the origin of Sgr A West is still a matter of debate, there remain a possibility that both "northern arm" of Sgr A West and knot1-3 are the relics of some mass-ejection activities of the the Galactic nucleus Sgr A*.

5.2.3 Proper motion measurements

A measurement of a proper motion is the best method for proving whether these X-ray knots originated from mass ejection activities of the Galactic nucleus (Sgr A*). To

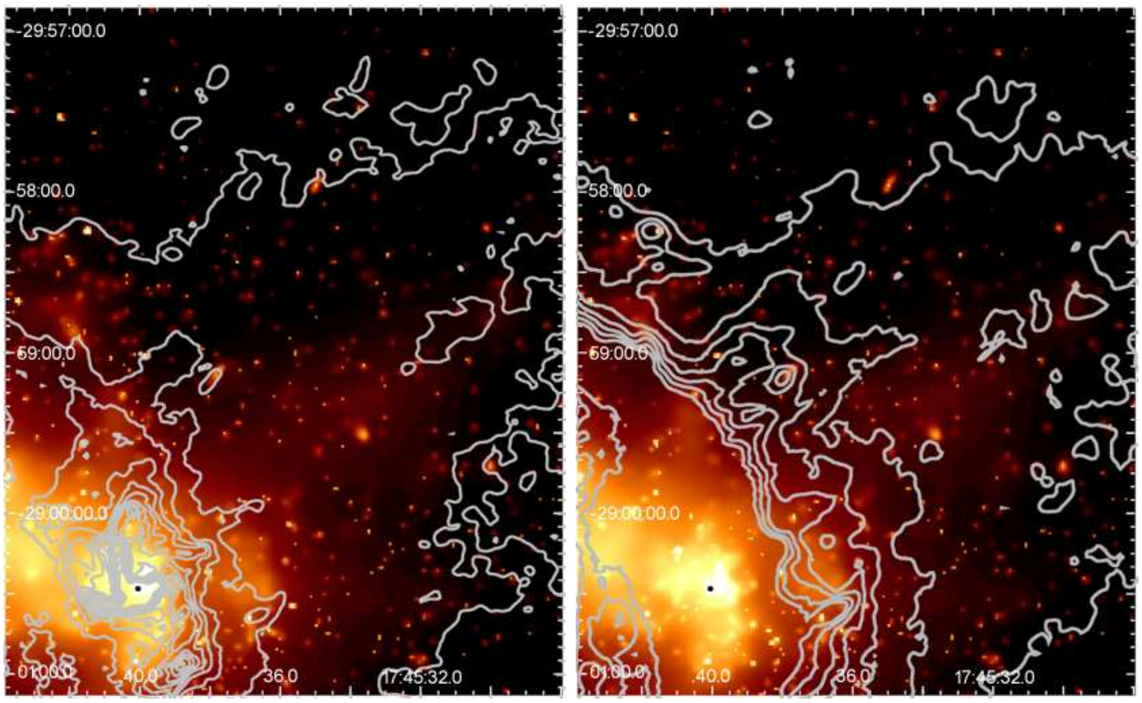

Figure 5.5: The adaptively smoothed 3.0−8.0 keV image of the northwest region of the Galactic center with *Chandra* ACIS. Overlayed contours indicate radio continuum intensities of 6 cm (left) and 20 cm (right) band obtained with VLA. The black point of each image represents the position of Sgr A*.

search for the proper motions, we examined a *Chandra* data. As listed in Table 5.1, *Chandra* had continually observed GC region for about 2.7 years; from Sep. 1999 to Jun. 2002. At first, we divided the all data sets into the early and the recent periods and merged as follows;

- Period 1: Sep. 1999 − Oct. 2000
- Period 2: May. 2002 − Jun. 2002

Second, We took surface brightness profiles projected to the line (white dashed line in Figure 5.2). The projection width from which we accumulate the photon is $6''$. The result is shown in Figure 5.6. Comparing peak positions of each knot profile of Period 1 and Period 2, we estimated the proper motion of these knots for about 2 years intervals by fitting each peaks of gaussians, however, no significant proper motion is detected. A typical statistical error of the position offset is $\pm$ 0.5 arcsec. It corresponds to $\pm$ 0.06 light years, assuming that the distance from the GC to us is 8.0 kpc (McNamara et al., 2000). From the above estimation, the upper limit of the projected velocity of the knots' proper motion is determined to be $\sim 0.03c$.

On the other hand, it is interesting that the knot1 has a slight but significant offset ($\sim 3''$) from its radio counterpart(Figure 5.5). The VLA observation was performed in 1985 by Yusef-Zadeh (Yusef-Zadeh & Morris, 1987), it means that there is an interval of about 15 years between the radio and X-ray observations. If the offset is due to the proper motion of the knot1, its projection velocity is estimated to be $0.025c$, which is the consistent with the upper limit shown in the above estimation.

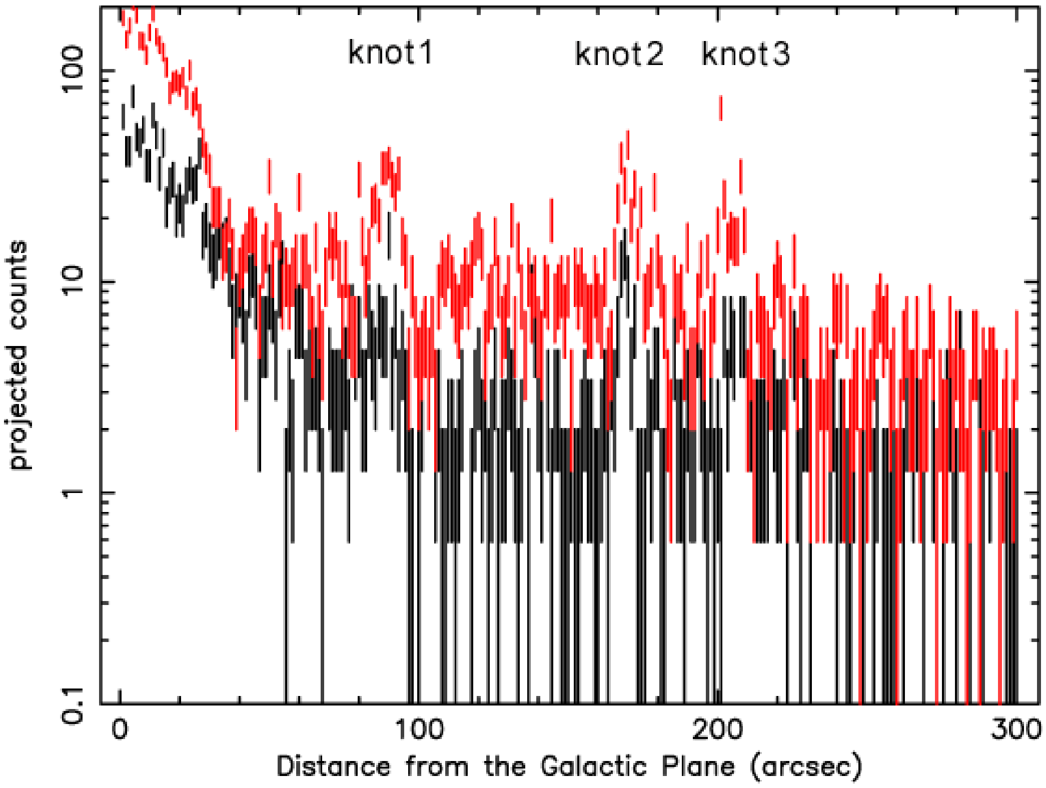

Figure 5.6: Linear profile of knot1–3 made from 3–8 keV photons. Red data shows represents the profile of Period 1, while black dat represents the profiles of Period 2.

5.3 Outflow Structures in the Southeast Region

In contrast to the several jet-like features in the northwest direction of the Galactic center, the southeast region exhibits an X-ray enhancement which seems outflow-like structure as if ejected from Sgr A* (Figure 5.1). We presented the X-ray analysis of the southwest region in the following subsections.

5.3.1 Radial profiles

As shown in Figure 5.1, there are two components in the southwest outflow, pervasive hot gas (shown in red) and two rim-like features (shown in blue). The X-ray morphology of both the inner and the outer rim indicate that they are the part of the shell centered on the Galactic center. In addition, hot diffuse gas (shown in red) seems fill the region within outer rim. These morphological features leads us to suspect that the southeast outflow has possible relation with some activities of the central compact object.

A radial profile shown in the right panel of Figure 5.8 supports the above relation. The profile is taken from the sector whose center is on the position of Sgr A*. The angular width of the profile is 56° with minimum and maximum angle of $205.1° < \theta < 261.1°$, which is adjusted with the angular size of rims.

5.3.2 X-ray spectra

We extracted X-ray spectra from the three different regions; "Outer rim", "Inner rim", and "Whole outflow" region . Source regions of two rims are taken from partial annuli along with shape of each enhancement. For the purpose of determining the radial width of source annulus region of each rim, we performed a gaussian fitting of two peaks, which are correspond with the enhancement of Inner and Outer rim as is shown in Figure 5.8). As the width of source region for each rim, 1 σ value of the best-fit gaussian applied, while the width of the background region is selected from $1\ \sigma < r < 3\ \sigma$ of the surroundings from corresponded source region. These source and background regions are shown in Figure 5.7.

"Outer rim" shows featureless spectrum, hence we tried to fit it with a power-law model convolved with a interstellar absorption effect then successfully reproduceed the spectrum. The best-fit result is shown in Figure 5.9 and Table 5.3. The best-fit value of the column density $N_{\rm H} \sim 10^{23}$ H cm^{-2} is consistent with an assumption that "Outer rim" is the source situated at the distance of Galactic center.

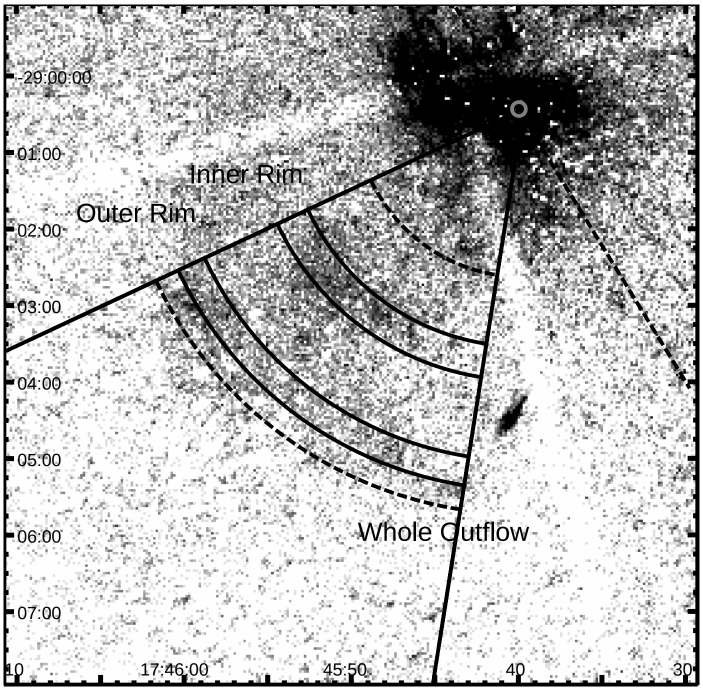

Figure 5.7: *Chandra* ACIS-I image of the Southeast outflow region in logarithmic. Energy band is 3.42–6.30 keV and all detected point sources are excluded from the image. A center of the small gray circle indicates the position of Sgr A*.

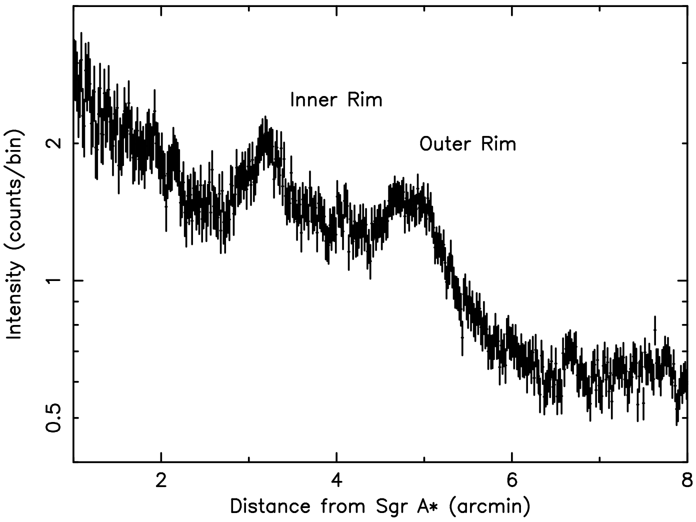

Figure 5.8: The radial profile of the southeast outflow region, which are extracted from a sector described with solid lines in Figure 5.7. The inner and outer annuli in the sector represent the source region of "Inner rim" and "Outer rim", while an annulus between dashed-lined arcs is that of "Whole outflow".

Although we also try to apply a thin thermal model (MEKAL) and it can also yield an acceptable fit. The lower limit of an electron temperature is determined to be 11.2 keV, which is even too high for the temperature of the hot component of the GC plasma (e.g. Koyama et al. (1996); Muno et al. (2004)). Then we tried to fit the spectrum of "Inner rim" with the same model of "Outer rim", however, we can recognize no significant difference between power-law model and MEKAL model in terms of a chi-square estimation due to the large systematic error of high background emission. Thus we cannot determine whether the X-ray emission of "Inner rim" is thermal or nonthermal from our analysis.

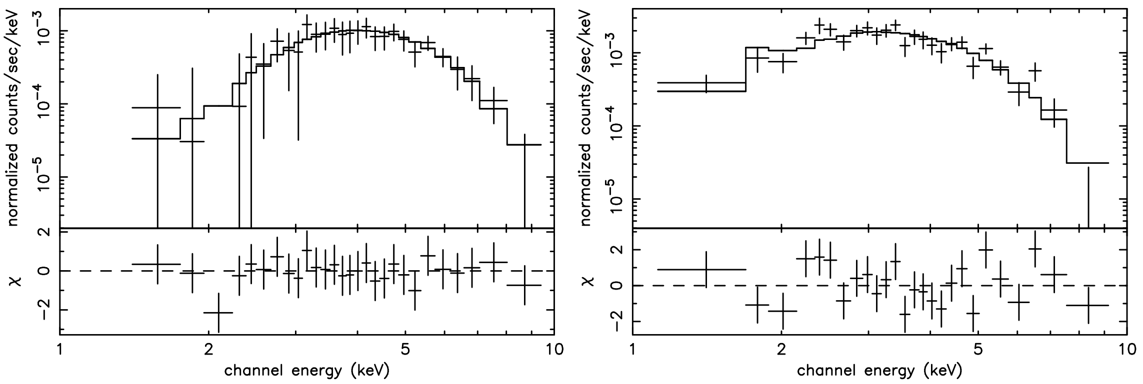

Figure 5.9: X-ray spectra of the Outer rim (left) and Inner rim (right) in the southeast outflow. Solid line in the upper panel of each image indicates the power-law model with the best fit parameters shown in Table 5.3.

Table 5.3: Best fit parameters for the outer and inner rims of the southeast outflow with different models

Parameter	Unit	Outer rim	Inner rim
Power-law			
Photon Index	Γ	2.2 (1.2–3.9)	2.8 (2.3–3.4)
$N_{\rm H}$	10^{22} cm^{-2}	11.8 (7.1–21.1)	6.2 (5.0–7.7)
Flux[a]	ergs s^{-1} cm^{-2}	1.2×10^{-13}	1.4×10^{-13}
χ^2/d.o.f.	—	10.1/25	33.3/23
MEKAL[b]			
kT	keV	35.5 (> 11.2)	2.8 (2.1–4.0)
$N_{\rm H}$	10^{22} cm^{-2}	8.4 (6.1–11.4)	5.5 (4.6–6.7)
χ^2/d.o.f.	—	12.0/25	33.7/23

All the errors given in parentheses indicate the 90% confidence limits.
[a] An observed flux of 2−10 keV.
[b] The metal abundance is fixed to a solar value.

On the other hand, An X-ray spectrum extracted from the "Whole outflow" (except for the source regions of the two rims) exhibits apparent emission lines from highly ionized Si, S, Ar, Ca, and Fe. The spectral profile qualitatively shares the characteristic of the GC pervasive hot plasma (Koyama et al., 1996; Muno et al., 2004). Hence we applied the two temperature thermal model plus a 6.4-keV gaussian to reproduce the observed spectrum. As a model of the X-ray spectrum, we employ two different models to reproduce the result; Case of collisional ionization equilibrium (MEKAL model) and non equilibrium of ionization (NEI model). The best-fit result for each fitting is shown in Figure 5.10 and Table 5.4. Both model cannot be reproduce the spectrum of "Whole outflow", perhaps because of the complexity of spatial distribution of plasmas. To obtain an acceptable fit, we must put into more parameters such as a filling factor for each component or another temperature components. However, it is not important for us to determine a physical condition of "Whole outflow" itself here. The essential result is that the X-ray spectral property of "Outer rim" (and maybe also "Inner rim") is clearly different from that of "Whole outflow", in spite of their spatial proximity.

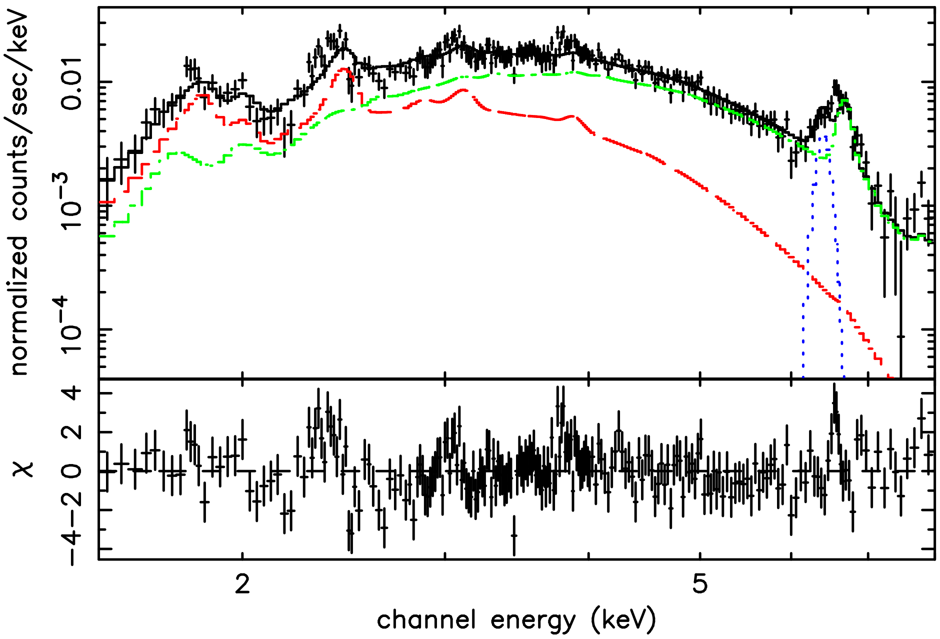

Figure 5.10: X-ray spectrum of the whole region of the Southeast Outflow. X-ray Emissions from inner and outer rims are excluded. Dashed lines in the upper panel of the image indicate the 2-kT NEI (red and green) + 6.4-keV Gaussian (blue) model with the best-fit parameters shown in Table 5.4. While the lower panel shows residuals from the model.

Table 5.4: Best fit parameters for the southeast outflow with thermal models

Parameter	Unit	Value
2-kT MEKAL + 6.4-keV Gaussian[b] model		
kT_1	keV	0.22 (0.21–0.24)
Z_1	solar	0.43 (0.1–1.0)
kT_2	keV	1.7 (1.6–2.0)
Z_2	solar	0.5 (0.4–0.6)
$N_{\rm H}$	10^{22} cm^{-2}	12.9 (11.7–13.7)
Flux[a]	ergs s^{-1} cm^{-2}	1.6×10^{-12}
χ^2/d.o.f.	—	321.3/217
2-kT NEI + 6.4-keV Gaussian[b] model[c]		
kT_1	keV	1.2 (0.9–1.4)
Z_1	solar	0.43 (fixed)
$(n_{\rm e}t)_1$	s cm^{-3}	1.9 (1.2–6.4) $\times 10^{11}$
kT_2	keV	4.3(3.7–5.8)
Z_2	solar	0.5 (fixed)
$(n_{\rm e}t)_2$	s cm^{-3}	3.9 (>0.09) $\times 10^{13}$
χ^2 / d.o.f.	—	344.4/217

All the errors given in parentheses indicate the 90% confidence limits.

[a] An observed flux of 2−10 keV.

[b] The center energy and line width are fixed to 6.40 keV and zero, respectively.

[c] $N_{\rm H}$ and metal abundance are fixed to the best fit value obtained with 2-kT MEKAL + 6.4-keV Gaussian fitting.

5.4 GC "Fishhook": A Nonthermal/6.4-keV Clump

With *Chandra* observation we have resolved clumpy X-ray structures in about $7'$ of northeast direction from the Sgr A*. it shows curious morphology such as fishhook, hence we named the X-ray structure GC "Fishhook". We divided the GC "Fishhook" into four different region named "Top", "Middle", "Bottom", and "East" as given in Figure 5.11. Interestingly, in the continuum band (3.42–6.30 keV), we can recognize all four components. In the neutral Fe-K band image (6.30–6.50 keV), on the other hand, "Top" component is quite dim while the rest three components exhibit clear enhancement.

This sharp contrast is also apparent in their X-ray spectra (Figure 5.12). The "Fishhook-Top" exhibits featureless spectrum. On the other hand, spectrum extracted from the rest of three region exhibit strong emission line at the energy near 6.4-keV, which indicates an existence of cold matter is embedded with the X-ray emitting region. If 6.4-keV emission is originated from fluorescence Kα of neutral iron, then Fe Kβ line emission is also expected. Hence, in order to reproduce their spectra, we employed a model of a power-law plus two Gaussians with taking absorption of ISM into account. The Center energy of the two Gaussians are fixed to 6.40 keV (Fe-Kα) and 7.06 keV (Fe-Kβ), respectively. The width of the both Gaussians are fixed to zero.

The fitting results are shown in Table 5.5. All but "Fishhook-Top" exhibit very strong 6.4-keV emission with equivalent widths of larger than 1 keV. In addition, "Fishhook-Bottom" exhibit 7.06-keV line whose intensity is weaker than 6.4-keV by an order of magnitude. The observed line ratio of 6.40 keV/7.06 keV is fully consistent with that of Kα/Kβ of neutral iron. They also have large absorption column in common except for "Fishhook-Top". Even the lower limit of their column density ($\geq$ (1–2) $\times$ 10^{23} cm^{-2}) is larger than that of interstellar column by twice or more. These result indicates that X-rays from the three part of GC "Fishhook" are come from deep interior of cold molecular cloud, as the case of Sgr B2 (Murakami et al., 2001b).

The best-fit result for "Fishook-Top",in contrast, rejected the existence of both emission line of 6.40 keV and 7.06 keV. Absorption column is also rather smaller than the rest part of GC "Fishhook".

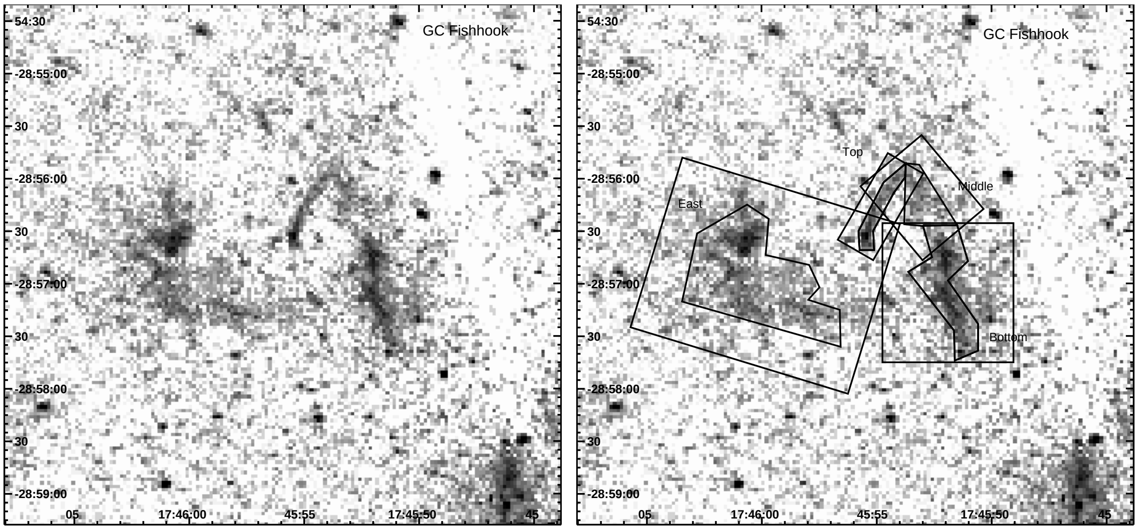

Figure 5.11: *Chandra* ACIS-I image of the GC "Fishhook" in logarithmic scale. Energy band is 3.42–6.30 keV. Source and surrounding background regions for the spectra shown in Figure 5.12 is shown with solid lines.

Table 5.5: Best fit parameters for the GC "Fishhook" with a power-law + two Gaussians model

Parameter	Unit	Top	Middle	Bottom	East
Photon Index	Γ	2.1 (1.6–3.0)	2.0 (0.3–3.5)	1 (0.5–1.8)	1.3 (0.7–1.6)
EW^a (6.40 keV)	eV	—	1180	1170	1040
EW^a (7.06 keV)	eV	—	—	103	—
$N_{\rm H}$	10^{22} cm^{-2}	8.8 (6.0–13.2)	17.7 (10.0–37.2)	24.9 (21.9–28.1)	16.0 (11.2–19.0)
Flux^b	ergs s^{-1} cm^{-2}	5.2×10^{-14}	7.7×10^{-14}	4.8×10^{-13}	7.3×10^{-13}
χ^2/d.o.f.	—	21.6/20	25.7/54	94.5/79	92.6/95

All the errors given in parentheses indicate the 90% confidence limits.

^{a} Equivalent width of the line. ^{b} An observed flux of 2−10 keV.

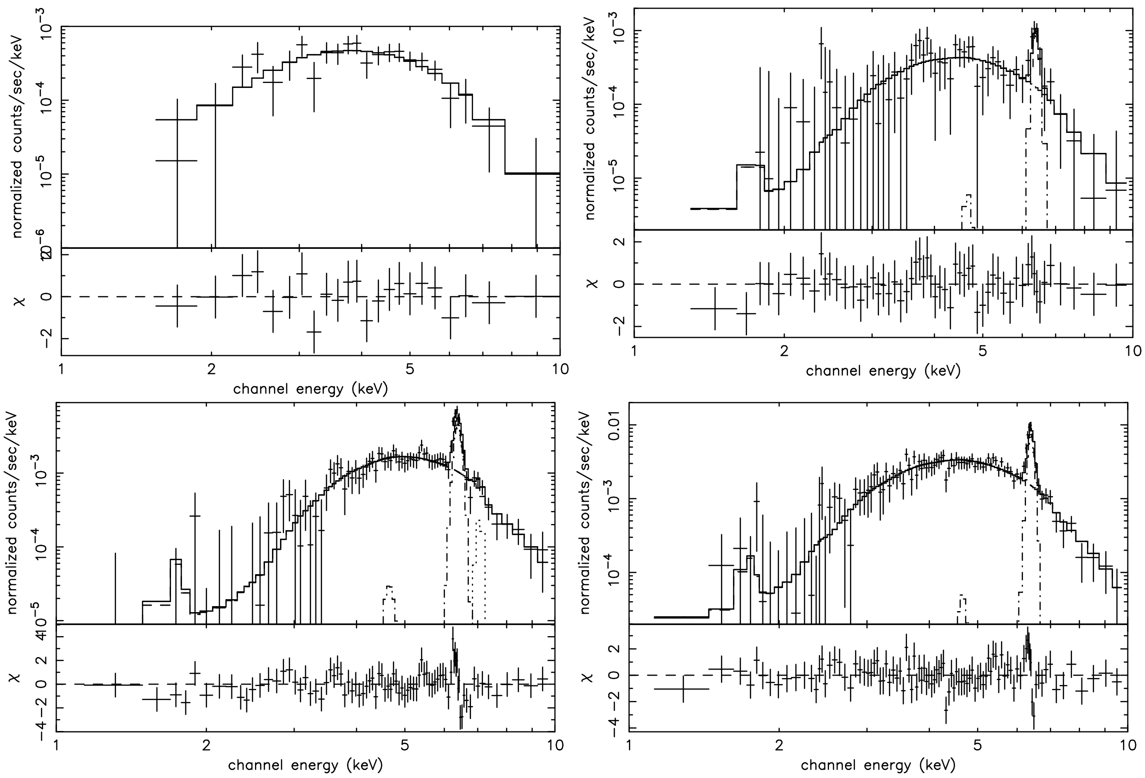

Figure 5.12: X-ray spectra of the "Fishhook" region. Top (upper left panel), Middle (upper right), Bottom (lower left), and East (lower right) is presented. Solid, dashed, and dotted-dashed line represent the fitting model with the best parameters shown in Table 5.5.

5.5 Other Nonthermal Structures

Our detailed analyses have discovered faint X-ray features near the Galactic center. In this section, we present brief results of X-ray analyses of another five linear X-ray features (named knot4, 5, 6, 7, and 8) which should be new nonthermal X-ray knots. For X-ray imaging and spectral analyses of these knots, we follow the same procedure which we applied for knot1–3. Figure 5.13 gives the spatial distribution of these knots. Figure 5.14, 5.15, 5.16, and 5.17 present close-up view of the each knot and the accumulated X-ray spectrum. The best-fit results of spectral fitting are summerized in Table 5.6.

Table 5.6: Best fit parameters for the Nonthermal X-ray Filaments fitted with a power-law model

	Source Counts[a] photons	Photon Index (Γ) $N(E) \propto E^{-\Gamma}$	Column Density ($N_{\rm H}$) 10^{22} H cm^{-2}	Flux[b] ergs cm^{-2} s^{-1}
knot4	800	1.8 (1.3–2.1)	12.9 (8.8–16.6)	5.3×10^{-14}
knot5	562	3.2 (2.2–4.6)	21.4 (15.6–30.2)	3.7×10^{-14}
knot6	782	3.1 (2.8–4.3)	8.7 (6.0–12.5)	3.4×10^{-14}
knot7	183	-2.4 (< 1.5)	1.1 (< 37.0)	5.2×10^{-14}
knot8	419	0.9 (-0.4–1.2)	10.2 (7.0–18.6)	3.7×10^{-14}

All the errors given in parentheses indicate the 90% confidence limits.
[a] Total counts from the source region after subtracting background counts. The subtracted background counts are normalized with an angular size of the region. [b] An absorbed X-ray flux of 2.0–10.0 keV.

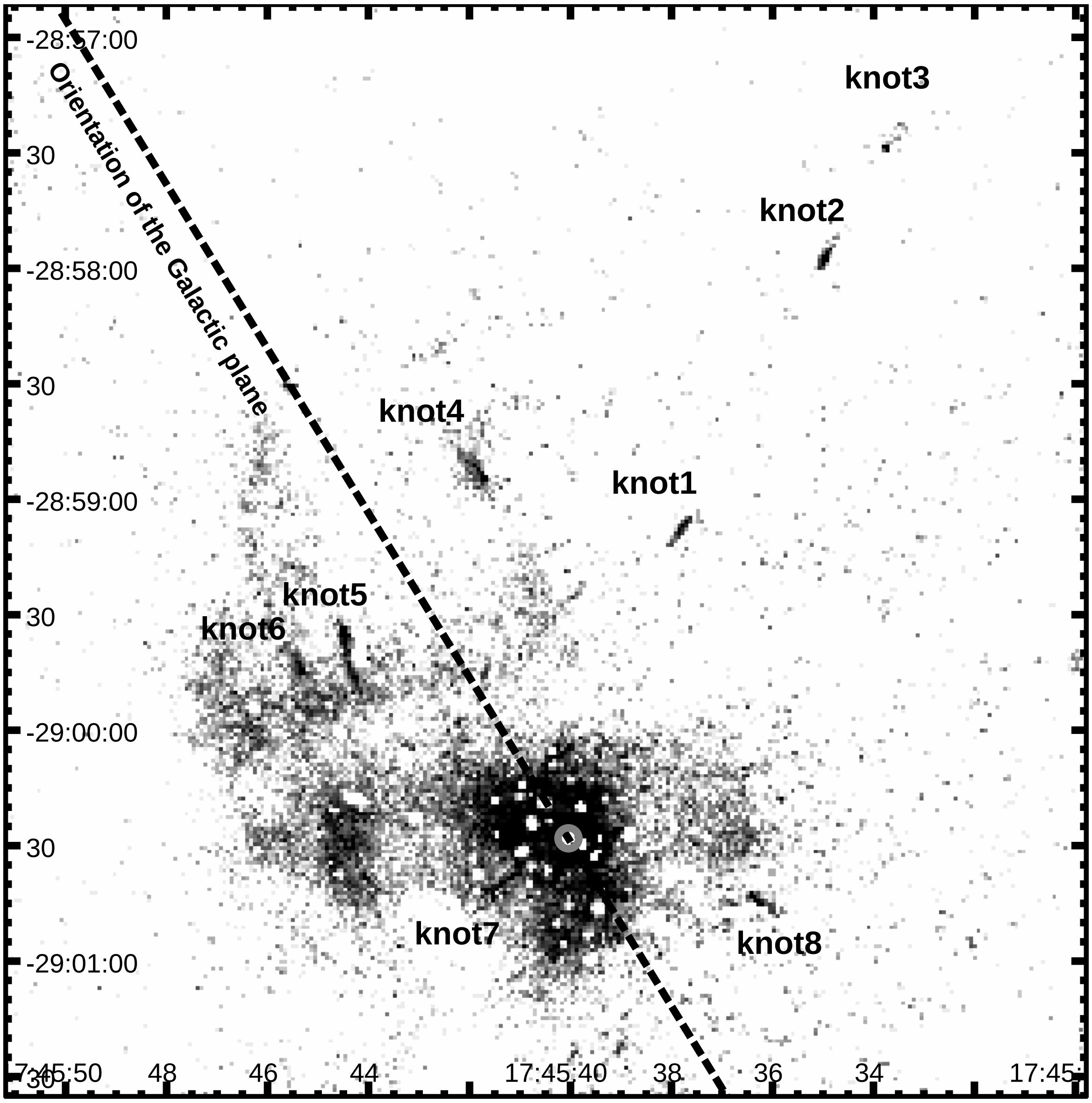

Figure 5.13: The spatial distribution of the X-ray knots discovered near the Galactic center with *Chandra* ACIS-I. The gray scale represents intensity of 3.42–6.30 keV photons in logarithmic scale. The detected point sources are all excluded from the image (see the section 5.1). The center of the gray circle indicates the position of Sgr A*.

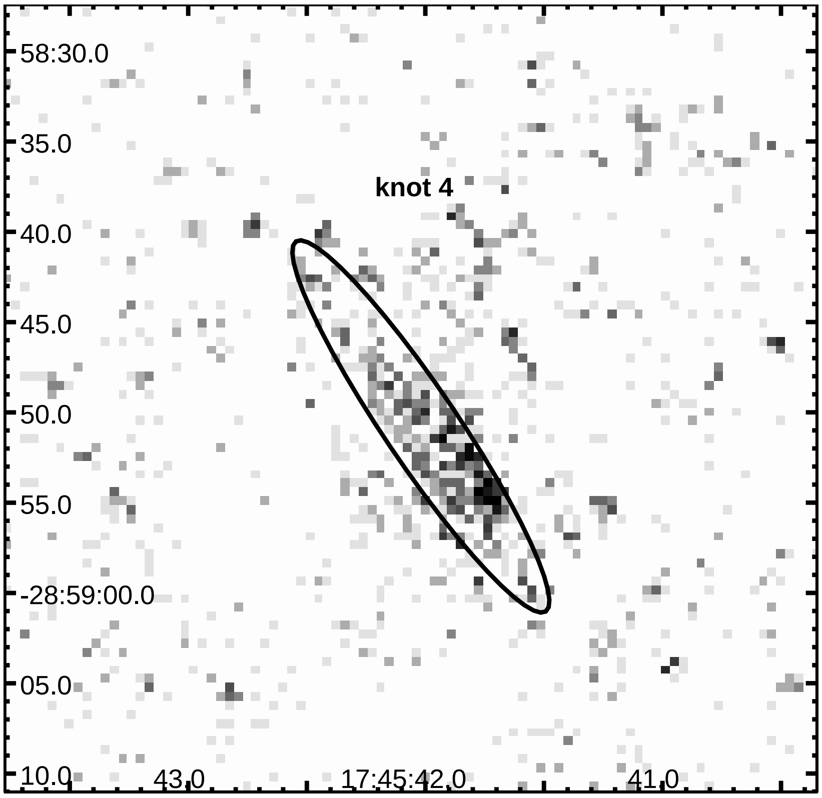

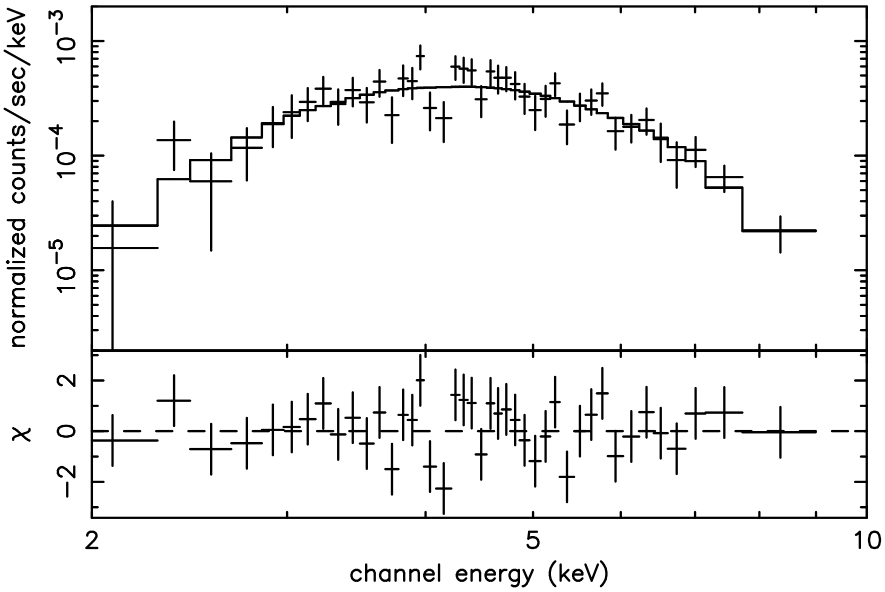

Figure 5.14: Close up X-ray image (top) and X-ray spectrum (bottom) of knot4 with *Chandra* ACIS-I. Top: The X-ray image are constructed from 3.0–8.0 keV X-ray photons from 3 to 300 counts par pixel with a logarithmic scale. The detected point sources are excluded from the image. Source photons of the spectrum shown in bottom are accumulated within the solid line ellipse. Bottom: Crosses and a solid line in the upper panel show data points and best-fit power-law model, respectively. while crosses in the lower panel give residuals from the best-fit model.

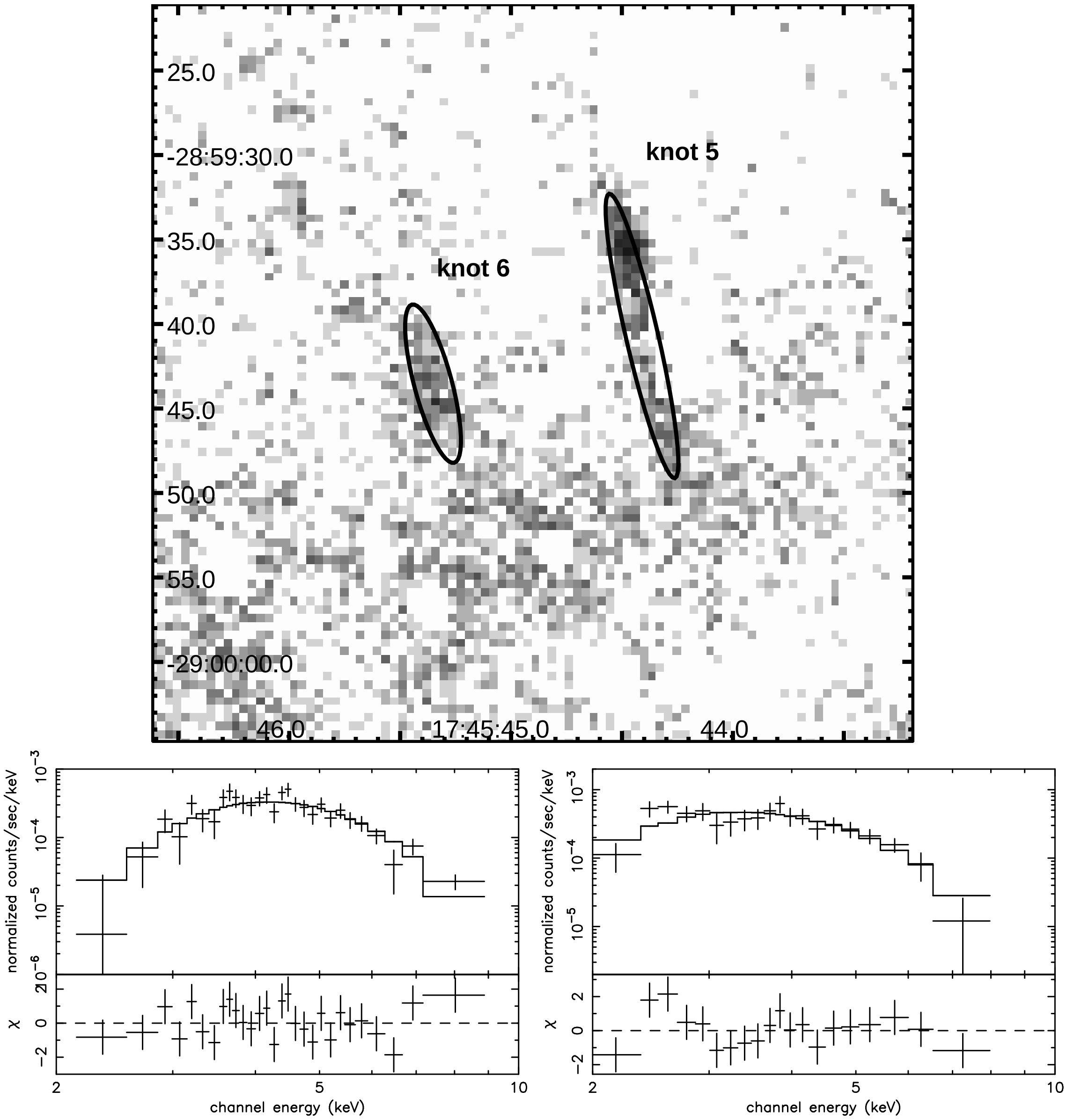

Figure 5.15: Close up X-ray image (top) and X-ray spectra (bottom) of knot5 and 6 with *Chandra* ACIS-I. Top: The X-ray image are constructed from 3.0–8.0 keV X-ray photons from 3 to 300 counts par pixel with a logarithmic scale. The detected point sources are excluded from the image. Source photons of the spectrum shown in bottom are accumulated within the solid line ellipse. Bottom: X-ray spectra of knot5 (left) and knot6 (right). Crosses and a solid line in the upper panel show data points and best-fit power-law model, respectively. while crosses in the lower panel give residuals from the best-fit model.

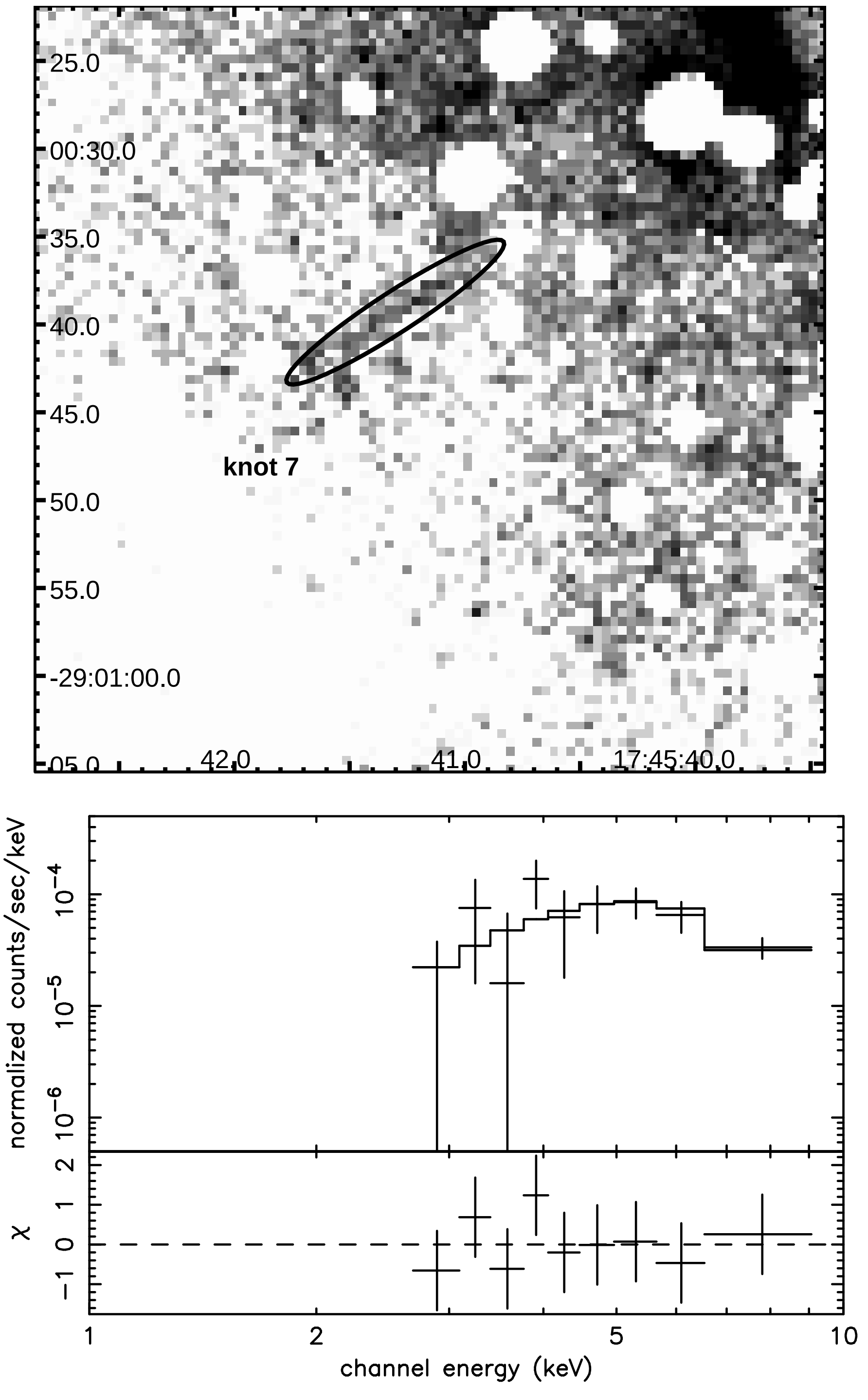

Figure 5.16: Close up X-ray image (top) and X-ray spectrum (bottom) of knot7 with *Chandra* ACIS-I. Top: The X-ray image are constructed from 3.0–8.0 keV X-ray photons from 3 to 300 counts par pixel with a logarithmic scale.The detected point sources are excluded from the image. Source photons of the spectrum shown in bottom are accumulated within the solid line ellipse. Bottom: Crosses and a solid line in the upper panel show data points and best-fit power-law model, respectively. while crosses in the lower panel give residuals from the best-fit model.

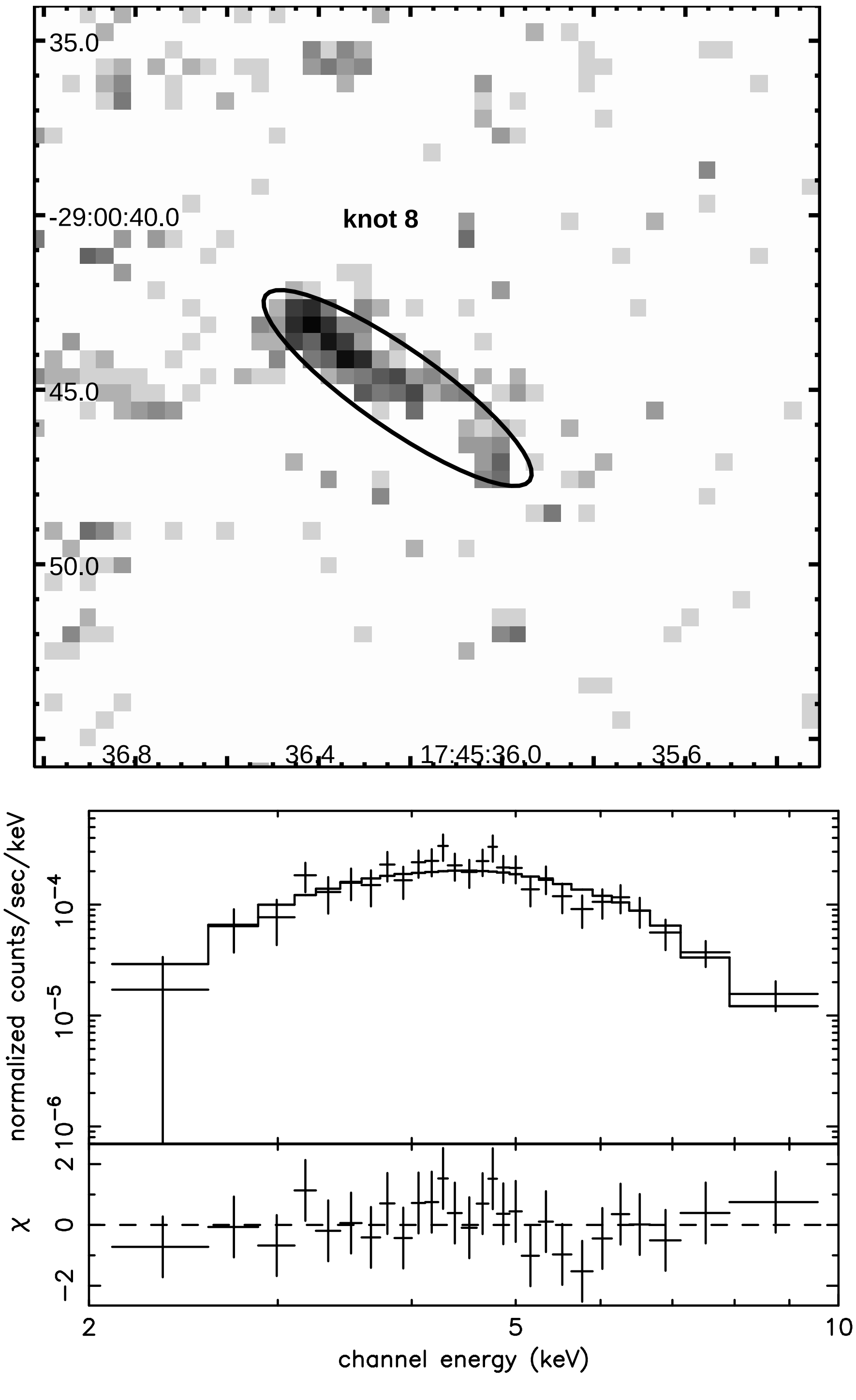

Figure 5.17: Close up X-ray image (top) and X-ray spectrum (bottom) of knot8 with *Chandra* ACIS-I. Top: The X-ray image are constructed from 3.0–8.0 keV X-ray photons from 3 to 300 counts par pixel with a logarithmic scale. The detected point sources are excluded from the image. Source photons of the spectrum shown in bottom are accumulated within the solid line ellipse. Bottom: Crosses and a solid line in the upper panel show data points and best-fit power-law model, respectively. while crosses in the lower panel give residuals from the best-fit model.

Chapter 6

Discussion

6.1 Brief Summary of the Results

In previous sections, we have presented the X-ray analyses of the small scale diffuse structures discovered near the GC.

G0.570−0.018 has a small diameter shell in X-rays, and the emission spectrum is well reproduced by a thin thermal hot plasma of NEI. The significantly small ionization parameter of the NEI model and X-ray morphology lead us to suspect that G0.570−0.018 is a very young supernova remnant which has not reached the adiabatic phase (so-called Sedov phase), but is still in the free expansion phase.

The X-rays from G359.8−0.3 are detected from the position coincident with the central region of a radio shell. Unlike the nonthermal property of the surrounding radio shell, the X-ray spectrum shows thermal feature; strong emission lines from the Si, S, Ar, Ca, and Fe. The X-ray and radio properties of G359.8−0.3 can be understood within the framework of Mixed-Morphology SNR scenario proposed by (Rho & Petre, 1998). Although the emission mechanism of a MMSNR is still debatable, their observational characteristics (rather old (t $\geq 10^4$ year), tendency to be distributed along the Galactic plane) support the idea that G359.8−0.3 is a MMSNR. In fact, other X-ray SNRs previously observed near the GC (G359.1−0.5 and Sgr A East) are classified with MMSNRs.

In addition to these thermal structures, we have discovered a number of Nonthermal X-ray structures within $40' \times 40'$ parsecs of the GC. They exhibit various shape such as a knot-like feature (knot1–8), rim-like feature (inner and outer rim of the southeast region), and a part of the nonthermal/6.4-keV clump ("Fishhook-Top"). Among them, the spatial distribution and X-ray spectra of knot1–3 indicate that they have a possible association to past activities of Sgr A* in the recent past.

6.2 Contribution to the GC Diffuse Emission

Now we resolved two thermal discrete sources and tens of nonthermal structures in the GC region. We at first evaluate how many portions of Galactic diffuse emission can be attributable to these discrete sources.

We estimated the X-ray luminosities of the newly found thermal structures, G0.570−0.018 and G359.8−0.3 to be 1.3×10^{34} ergs s^{-1} and 1.6×10^{35} ergs s^{-1}, respectively. (2–10 keV, unless otherwise mentioned, from here on). In addition, the contribution of Sgr A East, SNR near the Galactic center (8×10^{34} ergs s^{-1}) (Maeda et al., 2002), the integrate X-ray luminosity from discrete SNR candidates is 2×10^{35} ergs s^{-1}.

On the other hand, integrated luminosities of nonthermal X-ray knots (knot1–8) are amount to 5.1×10^{33} ergs s^{-1}. Other nonthermal structure of "Outer rim" of the southeast outflow and "Fishhook-Top" have luminosities of 2.0×10^{33} ergs s^{-1} and 1.3×10^{32} ergs s^{-1}, respectively. In addition, The detection of three nonthermal X-ray features are reported until now; G359.89−0.08 (1.0×10^{34} ergs s^{-1}; Sakano et al. (2003)), G359.54+0.18 (2.4×10^{33} ergs s^{-1}; Lu et al. (2003)), and G0.13−0.11 (3.2×10^{33} ergs s^{-1}; Wang et al. (2002)). Thus, the total X-ray luminosity of nonthermal components from the Galactic center can be estimated to $\sim$ (2–3) $\times 10^{34}$ ergs s^{-1}.

According to the *ASCA* observations (Koyama et al., 1996), the X-ray luminosity of the diffuse emission within central $1^\circ \times 1^\circ$ region of our Galaxy is estimated to $L_X \sim 10^{37}$ ergs s^{-1}. Early phase of *Chandra* observations resolved thousands of point sources from the $17' \times 17'$ field of the GC region. The integrated luminosity of these point sources is up to 1×10^{35} ergs s^{-1}. which contributes only 5 % of the X-ray luminosity of the GC (Muno et al., 2003). Although a point-like flaring source which spatially coincident with Sgr A* is detected, the X-ray luminosity of its quiescent state is as faint as $\sim 2 \times 10^{33}$ ergs s^{-1}. Assuming that the luminosity ratio of diffuse and integration of point sources almost constant whole the GC region, the *ASCA* estimation of the diffuse intensity is essentially not changed.

As a result, the detected SNR contribute 2% of the diffuse component of central $1^\circ \times 1^\circ$ (150 pc $\times$ 150 pc) region, and the contribution of detected nonthermal components turns out to be only 0.2%. This means that unresolved thermal diffuse X-rays dominate the luminosity of the GC.

As for nonthermal structures, however, their spatial distribution tends to be concentrated on the central region. For example, we identified 9 nonthermal X-ray knots from inner $r < 20$ pc of the Galactic center, but all of the knots are actually located within 10 pc from Sgr A* in a projected distance. Within the central $r < 20$ pc region of our Galaxy, the X-ray luminosity from diffuse component is amount to 2×10^{36} ergs s^{-1}, therefore nonthermal X-rays contribute $\sim$ 1%.

6.3 Emission Mechanism of Nonthermal Structures

The discrete nonthermal X-ray structures which we found in the Assuming that nonthermal X-rays are originated from synchrotron emission from high energy electrons, the characteristic photon energy and energy-loss time scale can be described as follows;

$$E_{\rm ph} \sim 2.0 \times (\frac{B}{1{\rm mG}})(\frac{E_{\rm e}}{10{\rm TeV}})^2 \ [{\rm keV}] \tag{6.1}$$

$$\tau_{\rm loss} \sim 1.3 \times (\frac{B}{1{\rm mG}})^{-2}(\frac{E_{\rm e}}{10{\rm TeV}})^{-1}[{\rm year}] \tag{6.2}$$

Since observed strength of the magnetic field in the GC region is extremely high, typically $B \sim 1$ mG (e.g., (Morris, 1994)), electron energy which emits synchrotron X-rays is roughly estimated to $\sim$ 10-100 TeV. This results in extremely short lifetime of nonthermal X-ray structures, which is about $\sim$ 1–10 year. The observed X-ray knots exhibits no significant variation on flux level during our observations with *Chandra*, spaced by a time interval of 2.7 year, which indicate that particle acceleration has been ongoing in the central several dozen pc region of our galaxy.

6.4 Possible Relation to the Galactic Nucleus

6.4.1 Spatial distribution of nonthermal structures

The nonthermal X-ray structures discovered through this work are located at the closest position to Sgr A* in all known nonthermal diffuse structures, including nonthermal radio filaments (NTRFs). Table 6.1 gives the summary of the X-ray properties of the

Table 6.1: The summary of X-ray properties of Nonthermal X-ray knots

	distance[a] parsecs	Size[b] arcsec	Inclination[b] degree (θ)	Direction[c] degree (ϕ)	Spectral Index $I(E) \propto E^{-\alpha}$	Luminosity[d] ergs s^{-1}
knot1	3.3	11.8 × 2.6	19	39	0.3(−0.7–1.2)	4.6×10^{32}
knot2	6.4	12.4 × 3.4	31	35	1.3(0.7–2.1)	5.4×10^{32}
knot3	7.8	11.0 × 3.2	19	34	0.8(−0.7–1.7)	3.8×10^{32}
knot4	3.9	24.8 × 4.0	93	74	0.8(0.3–2.1)	7.7×10^{32}
knot5	2.9	17.2 × 2.0	111	71	2.2(1.2–4.6)	1.3×10^{33}
knot6	3.2	8.8 × 2.4	109	64	2.1(1.8–3.3)	6.3×10^{32}
knot7	0.8	14.8 × 2.4	2	3	−3.4(<0.5)	5.4×10^{32}
knot8	2.1	9.2 × 2.2	24	46	−0.1(−1.4–0.2)	5.5×10^{32}
G359.89−0.08[†]	9.3	18 × 8	21	59	1.0(0.1–2.1)	1.0×10^{34}
G0.13−0.11[‡]	27	58 × 14	0	70	0.8(0.4–1.5)	3.2×10^{33}
G359.54+0.18[⋆]	70	27 × 10	15	60	~ 1	2.4×10^{33}

[a] Projected distance from Sgr A* to the center of a source region assuming it is located at the distance of the GC ($D = 8.0$ kpc).

[b] Length and width are length of major and minor axes of elliptical source region, while inclination indicates the angle of major axis with respect to the normal of the Galactic plane.

[c] The angle of the line from Sgr A* to the center of a source region with respect to the normal of the Galactic plane.

[d] Absorption-corrected 2–10 keV Luminosity.

[†] Values are quoted from Sakano et al. (2003).

[‡] Values are quoted from Wang et al. (2002).

[⋆] Values are quoted from Lu et al. (2003).

Table 6.2: Summary of radio properties of NTRFs / NTRF candidates detected at the GC region

Name	Size (arcmin)	Plane angle[a] (degree)	Flux Density (mJy)	Spectral Index[c] α ($S_\nu \propto \nu^{-\alpha}$)
Nonthermal Radio Filaments				
Radio Arc	32.0 × 4.0	5	24000	−0.3
G0.08+0.15[⋆]	21.1 × 0.3	0, 10[b]	4990	0.6 ± 0.1
Sgr C filament	11.5 × 0.2	15	4680	0.55 ± 0.4[d]
G359.79+0.17	8.3 × 0.5	35	2540	0.6 ± 0.1
G359.1−0.2[†]	22.7 × 0.4	0, 10[b]	1540	−0.3 − 0.8[e]
G359.96+0.09[⋆⋆]	12.5 × 0.4	15	1450	0.04 ± 0.03
G359.54+0.18	6.5 × 0.8	25	1420	0.8 ± 0.1
G0.087−0.087	2.5 ×0.3	5	390	—
G358.85+0.47[‡]	3.2 × 0.8	90	106	0.6[f]
Candidates of Nonthermal Radio Filaments				
G359.88−0.07	1.6 × 0.2	5	930	
G0.39−0.12	10.1 × 0.3	5	731	
G359.12+0.66	15.6 × 0.2	35	647	
G359.22−0.16	1.8 × 0.5	55	269	
G359.43+0.13	2.4 × 0.3	0, 90	265	
G0.39+0.05	4.1 × 0.3	5	232	
G359.40−0.07	1.7 × 0.3	40	229	
G0.02+0.04	2.0 × 0.3	0	228	
G359.66−0.11	3.5 × 0.5	20	226	
G359.86−0.24	8.1 × 0.2	35	205	
G359.59−0.34	2.3 × 0.2	25	188	
G359.85−0.02	1.8 × 0.2	90	173	
G0.06−0.07	2.1 × 0.2	15	163	
G359.90+0.19	2.4 × 0.2	35	129	
G0.37−0.07	1.1 × 0.3	5	128	
G359.40−0.03	1.8 × 0.2	5	93.8	
G359.99−0.54	8.6 × 0.2	30	88.8	
G359.33−0.42	2.4 × 0.2	55	81.0	
G359.36+0.09	2.5 × 0.2	60	65.2	
G0.43+0.01	1.6 × 0.3	5	43.9	

Size, angle, and flux density of all sources are quoted from VLA results Nord et al. (2004) except for G0.087−0.087 (Effersberg 100 m observation; Reich (2003)). [a] Angle of the NTRF with respect to the normal to the Galactic plane.

[b] Shows significant kinks, therefore they have two orientations.

[c] Mean spectral index of 90−20 cm quoted from (Anantharamaiah et al., 1991) unless otherwise mentioned.

[d] 90−18 cm spectral index quoted from (Anantharamaiah et al., 1991).

[e] 20−6 cm spectral index quoted from (Gray et al., 1995).

[f] 90−20 cm spectral index quoted from (Lang et al., 1999).

[⋆] Also named "Northern thread". [†] So called the "Snake".

[⋆⋆] Also named "Southern thread". [‡] So called the "Pelican".

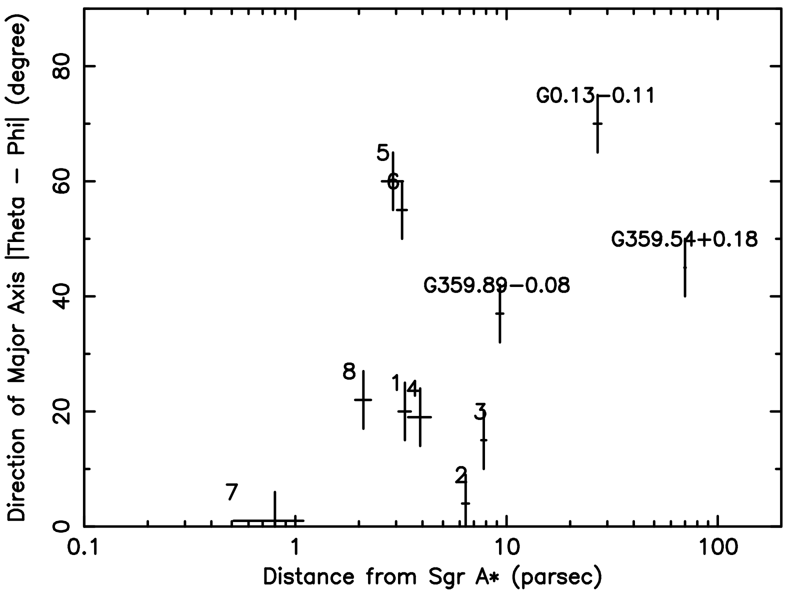

Figure 6.1: The Angle of major axis with respect to the Sgr A*–knot line ($|\theta - \phi|$)is described by a function of the distance from Sgr A*. The definition of θ and ϕ is shown in the Table 6.1. The number above black crosses represent knot ID.

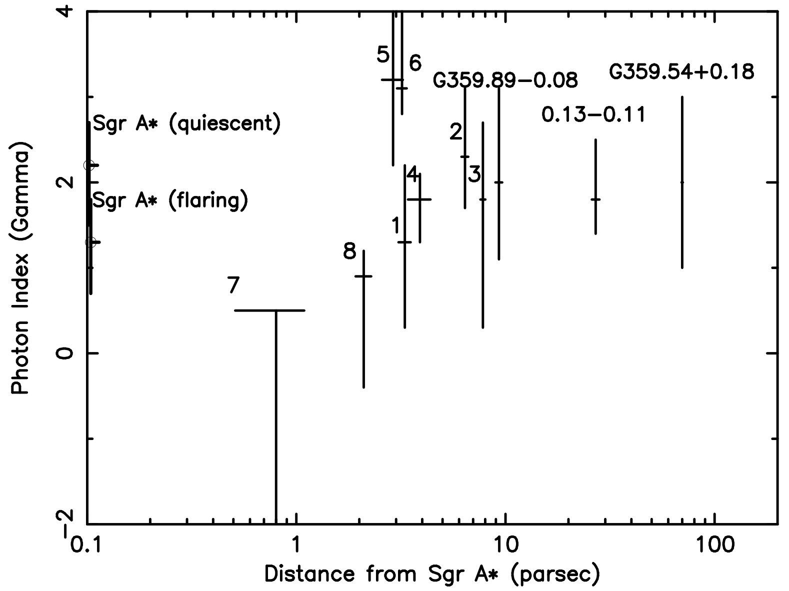

Figure 6.2: Photon index of each knot is described by a function of the distance from Sgr A*. The number above black crosses represent knot ID.

nonthermal X-ray knots. The nearest structure is located only 0.8 pc from Sgr A* in projection (knot 7), which is the closest nonthermal structure near the Galactic nucleus so far. On the other hand, a number of detection of NTRFs has been reported. Table 6.2 summarizes the radio properties of NTRFs /NTRF candidates. As was shown in Figure 2.11, NTRFs are distributed at least $1^\circ\times$ 1.2° (140 pc $\times$ 170 pc) region. In addition, Their spatial distribution shows no clear tendency to gather in the central region, which contrast starkly with that of the nonthermal X-ray structures.

Moreover, there is another contrast between the spatial distribution of X-ray and radio nonthermal structures. As shown in Figure 2.11 and Table 6.2, almost all of the radio filaments aligned perpendicular to the Galactic plane. This can be interpreted as the evidence for the existence of poloidal magnetic field of the GC region (Morris & Serabyn, 1996). On the other hand, X-ray knots seem radiate from the position of Sgr A*. Figure 6.1 show a plot of angles of major axes with respect to the Sgr A*–knot line ($|\theta - \phi|$ in Table 6.1) by a function of the distance from the Galactic nucleus. For the nearest knot, the value $|\theta - \phi|$ is almost zero. On the other hand, $|\theta - \phi|$ has a tendency to become larger as a distance increases.

Interestingly, the nonthermal X-ray knots which are moderately distant from Sgr A* have clear radio counterparts, such as G359.89$-$0.08 (d = 9.3 pc) and G0.13$-$0.11 (d = 27 pc), on the other hand, X-ray knots which are closer (d < 7 pc) to Sgr A* have marginal or no radio counterparts and vice versa. These indicate that the energy of high energy particles is declined as a distance from the Galactic nucleus increases. This support the scenario that particles are accelerated in the vicinity (r < 10 pc) of or/and at the Galactic nucleus. Near Sgr A*, electrons may have enough energy ($\sim$ 10-100 TeV) to emit synchrotron X-rays because they have been "fleshly" accelerated not yet reach their extremely short (< 1-10 yr) lifetime. On the other hand, as the distant from the site of the particle acceleration up to a hundred pc, the electrons have lost their initial energy down to $\sim$ GeV order, and emit via synchrotron process only in radio band. The existence of the clear radio counterparts for G359.89$-$0.08 and G0.13$-$0.11 can be understood as the middle-point of the above two cases.

It should be noted that the detection limit of the faint radio structures as another possibility for the lack of radio counterparts near the Galactic nucleus. The background radio emission is extremely high near the Sgr A* especially within r < 10 pc region (Figure 5.5), where the synchrotron emission of the shell of young supernova remnant Sgr A East, which make it difficult to resolve faint structures.

6.4.2 Implication on past activities of the Galactic nucleus

The concentration of X-ray knots on the GC region lead us to suspect that their origin is closely related to the high energy activities of Sgr A*. Figure 6.2 gives the photon indices of the X-ray knots as a function of the distance from Sgr A*. Although statistical errors are rather large, photon index of each knot is similar to that of Sgr A* in the flaring state. Without some exceptions (knot 5 and 6), we also see the tendency that index become steep as the distance increases.

One explanation for the origin of X-ray knots are originated from jets ejected from Sgr A*. As already presented in Section 5.2., knot1–3 is most plausible source as the jets. Our *Chandra* 2.7 year measurements of proper motion of knot1–3 give an upper limit of these knots of $\sim 0.03c/\sin\,\Theta$, where Θ is the angle between our line-of-sight and moving direction of the knots. On the other hand, projected distance from Sgr A* to each knots are 11, 21, and 25 light year, respectively. Therefore we can infer that knot1–3 had been ejected from Sgr A* about $(400–900)/\sin\,\Theta$ years ago. It is interesting that the XRN model predicts that Sgr A* is as luminous in X-rays as 10^{39} ergs s^{-1} about 300 years ago from observation of nearby molecular clouds (Murakami et al., 2001b). In addition, Maeda et al. (2002) claimed that high density blast wave of the SNR A East passed over Sgr A* about 10^3 years ago, which triggered mass accretion on the central massive black hole. These time-scale are coincident with our estimation of timing when knot1–3 had been ejected.

If the above scenario is true, this may be the first detection of the jet structure from Sgr A*. For further confirmation, however, monitoring X-ray observation by *Chandra* and detection of positive proper motion are required.

Chapter 7

Conclusion

The main conclusion of our X-ray spatial and spectral study of thermal and nonthermal structures in the GC region are summarized as follows.

- Using the data acquired with *Chandra*, with the help of *ASCA* and *XMM-Newton*, we have newly discovered two thermal structures named G0.570−0.018 and G359.8−0.3, and eleven nonthermal structures/candidate nonthermal structures from the GC region.

- G0.570−0.018 has been found to be extraordinary high temperature ($kT \sim$ 6 keV), small diameter (less than 1 pc) X-ray shell-like source. The physical conditions can be well understood with the scenario of an extremely young supernova remnant (SNR) before reaching adiabatic expansion phase (Sedov phase).

- The X-rays of G359.8−0.3 have been found from the central region of nonthermal radio shell. The observable parameters consistently explained in the frame work of the "mixed-morphology" SNR with the total energy and age of $E_{\mathrm{thermal}} \sim 1 \times 10^{50}$ ergs and 1.3×10^{4} year.

- Nonthermal structures exhibit various shape such as a knot-like feature (knot1–8), rim-like feature (inner and outer rim of the southeast region), and a part of the nonthermal/6.4-keV clump ("Fishhook-Top"). They all show hard X-ray photon indices of $\Gamma \sim< 2$.

- The spatial distribution and photon index distribution of X-ray/radio nonthermal structures, indicate that the particle acceleration has been ongoing in the vicinity of the Galacitic nucleus. Jet-like X-ray nonthermal structures also imply that they have a possible association with the past activities of the Galactic nucleus (Sgr A*) which have been predicted by past X-ray observations of giant molecular clouds near the GC.

Bibliography

Aharonian et al., 2004, *Astron. Astrophys.* , 425, L13

Anantharamaiah, K. R., Pedlar, A., Ekers, R. D., & Goss, W. M., 1991, *Monthly Notices Roy. Astron. Soc.* , 249, 262

Anders, E., & Grevesse, N., 1989, *Geochim. Cosmochim. Acta.*, 53, 197

Aschenbach, B., 1985, *Rep. Prog. Phys.*, 48, 579

Aschenbach, B., 1991, *Rev. Mod. Astron.*, 4, 173

Backer, D. C., & Sramek, R. A., 1999, *Astrophys. J.*, 524, 805

Baganoff, F. K., Bautz, M. W., Brandt, W. N., Chartas, G., Feigelson, E. D., Garmire, G. P., Maeda, Y., Morris, M., Ricker, G. R., Townsley, L. K., & Walter, F. 2001, *Nature*, 413, 45

Baganoff, F. K., Maeda, Y., Morris, M., Bautz, M. W., Brandt, W. N., Cui, W., Doty, J. P., Feigelson, E. D., Garmire, G. P., Pravdo, S. H., Ricker, G. R., & Townsley, L. K., 2003, *Astrophys. J.*, 591, 915

Balick, B. & Brown, R. L., 1974, *Astrophys. J.*, 194, 265

Bamba, A., Yokogawa, J., Sakano, M., & Koyama, K., 2000, *Publ. Astron. Soc. Japan* , 52, 259

Bamba, A., Tomida, H., & Koyama, K., 2000, *Publ. Astron. Soc. Japan* , 52, 1157

Borkowski, K. J., Lyerly, W. J., & Reynords, S. P., 2001, *Astrophys. J.*, 548, 820

Borkowski, K. J., Rho, J., Reynords, S. P., & Dyer, K. K., 2001a, *Astrophys. J.*, 550, 334

Burrows, D. N., et al., 2000, *Astrophys. J.*, 543, L149

Case, G. L., & Bhattacharya, D., 1998, *Astrophys. J.*, 504, 761

Chakrabarty, D., & Saha, P., 2001, *Astron. J.* , 122, 232

Chandran, B. D. G., 2001, *Astrophys. J.*, 562, 737

Diehl, R., Dupraz, C., Bennett, K., Bloemen, H., Knödlseder, Lichti, G., Morris, D., Ryan, J., Scönfelder V., Steinle, H., Strong, A., Swanenburg, B., Varendorff, M., & Winkler, C., 1995, *Astron. Astrophys.* , 298, 445

Diehl, R., Knödlseder, J., Lichti, G. G., Kretschmer, K., Schanne, S., Schönfelder, V., Strong, A. W., von Kienlin, A., Weidenspointner, G., Winkler, C., & Wunderer, C., 2003, *Astron. Astrophys.* , 411, L451

Eckart, A., & Genzel, R., 1997, *Monthly Notices Roy. Astron. Soc.* , 284, 576

Ekers, R. D., Goss, W. M., & Schwarz, U. J., 1975, *Astron. Astrophys.* , 43, 159

Ekers, R. D., van Gorkom, J. H., Schwarz, U. J., & Goss, W. M., 1983, *Astron. Astrophys.* , 122, 143

Enomoto, R., et al. 2002, *Nature*, 416, 823

Falke, H., & Markoff, S., 2000, *Astron. Astrophys.* , 362, 113

Freeman, P. E., Kashyap, V., Rosner, R., & Ramb, D. Q., 2002, *Astrophys. J. Suppl.* , 138, 185

Genzel, R., Hollenbach, D., & Townes, C. H., 1994, *Rep. Prog. Phys.* 57, 417

Genzel, R., Pichon, C., Eckart, A., Gerhard, O., & Ott, T., 2000, *Monthly Notices Roy. Astron. Soc.* , 317, 348

Ghez, A. M., Klein, B. L., Morris, M., & Becklin, E. E., 1997, *Astrophys. J.*, 509, 678

Ghez, A. M., Salim, S., Hornstein, S. D., Tanner, A., Lu, J. R., Morris, M., Becklin, E. E., & Duchêne, G. 2005, *Astrophys. J.*, 620, 744

Giacconi, R., et al., 1979, *Astrophys. J.*, 230, 540

Goldwurm, A., Brion, E., Goldoni, P., Ferrando, P., Daigne, F., & Decourchelle, A., 2003, *Astrophys. J.*, 584, 751

Gray, A., Nicholls, J., Ekers, R. D., & Cram, L., 1995, *Astrophys. J.*, 448, 164

Green, D. A., 2004, A Catalogue of Galactic Supernova Remnants, 2004 January version. Available at http://www.mrao.cam.ac.uk/surveys/snrs/

Hartman, R. C., et al., 1999, *Astrophys. J. Suppl.* , 123, 79

Hess, V. F., 1911, *Phys. Zeits.*, 12, 998

Hess, V. F., 1912, *Phys. Zeits.*, 13, 1084

Jansky, K. G. 1933, *New York Times*, Vol. LXXXII, No. 27495 (May 5), 1

Johnson, W. N., Harnden, F. R., & Haymes, R. C., 1972, *Astrophys. J.*, 172, L1

Jones, T. W., 1974, *Astron. Astrophys.* , 30, 37

Kaastra, J.S., 1992, An X-Ray Spectral Code for Optically Thin Plasmas (Internal SRON-Leiden Report, updated version 2.0)

Khokhlov, A., & Melia, F., 1996, *Astrophys. J.*, 457, L61

Kellogg, E., Gursky, H., Murray, S., Tananbaum. H, & Giacconi, S., 1971, *Astrophys. J.*, 169, L99

Kinzer, R. L., Milne, P. A., Kurfess, J. D., Strickman, M. S., Johnson, W. N., & Purcell, W. R., 2001, *Astrophys. J.*, 559, 282

Kosack et al., 2004, *Astrophys. J.*, 608, L97

Koyama, K., Awaki, H., Kunieda, H., Takano, S., Tawara, Y., Yamauchi, S., Hatsukade, I., & Nagase, F., 1989, *Nature*, 339, 603

Koyama, K., Petre, R., Gotthelf, E. V., Hwang, U., Matsuda, M., Ozaki, M., & Holt, S. S., 1995, *Nature*, 378, 255

Koyama, K., Maeda, Y., Sonobe, T., Takeshima, T., Tanaka, Y., & Yamauchi, S. 1996, *Publ. Astron. Soc. Japan* , 48, 249

Koyama, K., Kinugasa, K., Matsuzaki, K., Nishiuchi, M., Sugisaki, M., Torii, K., Yamauchi, S., & Aschenbach, B., 1997, *Publ. Astron. Soc. Japan* , 49, L7

Lang, C. C., Anantharamaiah, K. R., Kassim, N. E., & Lazio, T. J. W., 1999, *Astrophys. J.*, 521, L41

LaRosa, T. N., Kassim, N. E., Lazio, T. J. W., & Hyman, S. D. 2000, *Astron. J.* , 119, 207

LaRosa, T. N., Nord, M. E., Lazio, T. J. W., & Kassim, N. E., 2004, *Astrophys. J.*, 607, 302

Lesch, H., Schlickeiser, R., & Crusius, A., 1988, *Astron. Astrophys.* , 200, L9

Liedahl, D.A., Osterheld, A.L., & Goldstein, W.H., 1995, *Astrophys. J. Lett.* , 438, 115

Lis, D. C., & Carlstrom, J. E., 1994, *Astrophys. J.*, 424, 189

Liszt, H., & Spiker, R., 1995, *Astrophys. J. Suppl.* , 98, 259

Lu, F. J., Wang, Q. D., & Lang, C., 2003, *Astron. J.* , 126, 319

Maeda, Y., Koyama, K., Sakano, K., Takeshima, K., & Yamauchi, S., 1996, *Publ. Astron. Soc. Japan* , 48, 417

Maeda, Y., 1998, PhD Thesis, Kyoto University

Maeda, Y., Baganoff, F. K., Feigelson, E. D., Morris, M., Bautz, M. W., Brandt, W. N., Burrows, D. N., Doty, J. P., Garmire, G. P., Pravdo, S. H., Ricker, G. R., & Townesley, L. K., 2003, *Astrophys. J.*, 570, 671

Mayer-Hasselwander, H. A., et al., 1998, *Astron. Astrophys.* , 335, 161

McGee, R. X., Bolton, J. G., 1954, *Nature*, 173, 985

McNamara, D. H., Madsen, J. B., Barnes, J., Ericksen, B. F. 2000, *Publ. Astron. Soc. Pacific* , 112, 202

Mehlinger, M., Yusef-Zadeh, F., Palmer, P., & Goss, W. M., 1992, *Astrophys. J.*, 401, 168

Mehlinger, M., Palmer, P., Goss, W. M., & Yusef-Zadeh, F., 1993, *Astrophys. J.*, 412, 684

Melia, F., 1992, *Astrophys. J.*, 387, L25

Melia, F., Fatuzzo, M., Yusef-Zadeh, F., & Markoff, S. 1998, *Astrophys. J. Lett.* , 508, L65

Melia, F., & Falke, H., 2001, *Annu. Rev. Astron. Astrophys.*, 39, 309

Mewe, R., Gronenschild, E. H. B. M., & van den Oord, G. H. J., 1985, *Astron. Astrophys. Suppl.* , 62, 197

Mewe, R., Lemen, J.R., & van den Oord, G.H.J. 1986, *Astron. Astrophys. Suppl.* , 65, 511

Mezger, P. G., Duschl, W. J., & Zylka, R., 1996, *Astron. Astrophys. Rev.*, 7, 289

Morris, M., & Yusef-Zadeh, F., 1985, *Astron. J.* , 90, 2511

Morris, M., 1994, in the Nuclei of Normal Galaxies, ed. R. Genzel & A. I. Harris (NATO ASI Ser. C, 445; Dordrecht: Kluwer), 185

Morris, M., & Serabyn, E., 1996, *Annu. Rev. Astron. Astrophys.* 34, 645

Muno, M. P., et al., 2003, *Astrophys. J.*, 589, 225

Muno, M. P., et al., 2004, *Astrophys. J.*, 613, 326

Murakami, H., Koyama, K., Sakano, M., Tsujimoto, M., & Maeda, Y., 2000, *Astrophys. J.*, 534, 283

Murakami, H., Koyama, K., Tsujimoto, M., Maeda, Y., & Sakano, M., 2001, *Astrophys. J.*, 550, 297

Murakami, H., Koyama, K., & Maeda, Y., 2001, *Astrophys. J.*, 558, 687

Narayan, R., Mahadevan, R., Grindlay, J. E., Popham, R. G., & Gammie, C., 1996, *Astrophys. J.*, 492, 554

Naya, J. E., Barthelmy, S. D., Bartlett, L. M., Gherels, N., Leventhal, M., Parsons, A., Teegarden, B. J., & Tueller, J., 1996, *Nature*, 384, 44

Nord, M. E., Lazio, T. J. W., Kassim, N. E., Hyman, S. D., LaRosa, T. N., Brogan, C. K., & Duric, N., 2004, *Astrophys. J.*, 128, 1646

Oka, T., Hasegawa, T., Hayashi, M., Handa, T., & Sakamoto, S., 1998a, *Astrophys. J.*, 493, 730

Oka, T., Hasegawa, T., Sato, F., Tsuboi, M., & Miyazaki, A., 1998b, *Astrophys. J. Suppl.* , 118, 455

Ostriker, J. P., & McKee, C. F., 1988, Rev. Mod. Phys., 60, 1

Park, S., Burrows, D. N., Garmire, G. P., Nousek, J. A., McCray, R., Michael, E., & Zhekov, S, 2002, *Astrophys. J.*, 567, 31

Park, S., Zhekov, S. A., Burrows, D. N., Garmire, G. P., & McCray, R., 2002, *Astrophys. J.*, 567, 31

Pavlinsky, M. N., Grebenev, S. A., & Sunyaev, R. A., 1994, *Astrophys. J.*, 425, 110

Pedlar, A., Anantharamaiah, K. R., Ekers, R. D., Goss, W. M., van Gorkom, J. H., Schwarz, U. J., & Zhao, J., 1989, *Astrophys. J.*, 342, 769

Piddington J. H., & Minnett, H. C., 1951, *Aust.J. Sci. Res. A*, 4, 459

Porquet, D., Predehl, P., Aschenbach, B., Grosso, N., Goldwurm, A., Gokdoni, P., Warwick, R. S., & Decourchelle, A., 2003, *Astron. Astrophys.* , 407, L17

Prantzos, N., & Diehl, D., 1996, *Phys. Rep.*, 267, 1

Purcell, W. R., et al. 1997, *Astrophys. J.*, 491, 725

Reich, W., Sofue, Y., Wielebinski, R., & Seiradakis, J. H., 1988, *Astron. Astrophys.* , 191, 303

Reich, W., 2003, *Astron. Astrophys.* , 401, 1023

Reid, M. J., Readhead, A. C. S., Vermeuren, R. C., & Treuhaft, R. N., 1999, *Astrophys. J.*, 524, 816

Rho, J., & Petre, R., 1998, *Astrophys. J.*, 503, L167

Reid, M. J., Readhead, A. C. S., Vermeulen, R. C., & Treuhaut, R. N., 1999, *Astrophys. J.*, 524, 816

Ryter, Ch. E., 1996, *Astrophysics and Space Science*, 236, 285

Sakano, M., et al., 1999, Proc. of Japanese-German Workshop on High Energy Astrophysics, ed. W. Becker & M. Itoh, (MPE Rep. 270; Garching bei Muenchen: MPE), 113

Sakano, M., 2000, PhD thesis, Kyoto University

Sakano, M., Koyama, K., Murakami, H., Maeda, Y., & Yamauchi, S., 2001, *Astrophys. J. Suppl.* , 138, 19

Sakano, M., Warwick, R. S., Decourchelle, C., & Predehl, P., 2003, *Monthly Notices Roy. Astron. Soc.* , 340, 747

Sakano, M., Warwick, R. S., Decourchelle, C., & Predehl, P., 2004, *Monthly Notices Roy. Astron. Soc.* , 350, 129

Schödel, R., et al. 2002, *Nature*, 419, 694

Seiradakis, J. H., Reich, W., Wielebinski, R., Lasenby, A. N., & Yusef-Zadeh, F., 1989, *Astron. Astrophys. Suppl.* , 81, 291

Serabyn, E., Carlstrom, J., Lay, O., Lis, D. C., Hunter, T. R., & Lacy, J. H., 1997, *Astrophys. J.*, 490, L77

Shore, N. S., & LaRosa, T. N., 1999, *Astrophys. J.*, 521, 587

Sidoli, L., & Mereghetti, S., 1999, *Astron. Astrophys.* , 349, L49

Sofue, Y., & Handa, T., 1984, *Nature*, 310, 568

Sofue, Y., 1985, *Publ. Astron. Soc. Japan* , 37, 697

Sofue, Y., Reich, W., Inoue, M., & Seiradakis, J. H., 1987, *Publ. Astron. Soc. Japan* , 39, 95

Sofue, Y., 1988, *Comments Astrophys.*, 13, 29

Struder, L., et al. 2001, *Astron. Astrophys.* , 365, L18

Tanimori, T., et al. 1998, *Astrophys. J.*, 497, L25

Teegarden, B. J., et al., 2004, to be appeared in *Astrophys. J.*, astro-ph/0410354

Townsley, L. K., Broos, P. S., Garmire, G. P., & Nousek, J., 2000, *Astrophys. J.*, 534, L139

Trümper, J., 1983, *Adv. Space Res.*, 2(4), 241

Tsuboi, M., Inoue, M., Handa, T., Tabara, H., & Kato, T., 1985, *Publ. Astron. Soc. Japan* , 37, 359

Tsuboi, M., Inoue, M., Handa, T., Tabara, H., Kato, T., Sofue, Y., & Kaifu, N., 1986, *Astron. J.* , 92, 818

Tsuboi, M., Kawabata, T., Kasuga, T., Handa, T., & Kato, T., 1995, *Publ. Astron. Soc. Japan* , 47, 829

Tsuboi, M., Handa, T., & Ukita, N., 1999, *Astrophys. J. Suppl.* , 120, 1

Tsuchiya et al., 2004, *Astrophys. J.*, 606, L115

Turner, M., et al. 2001, *Astron. Astrophys.* , 365, L27

Wang, Q. D., Lu, F., & Lang, C., 2002, *Astrophys. J.*, 581, 1148

Wang, Q. D., Gotthelf, E. V., & Lang, C. C., 2002, *Nature*, 415, 148

Yuan, F., Markoff, S., & Falcke, H., 2002, *Astron. Astrophys.* , 383, 854

Yuan, F., Quataert, E., & Narayan, R., 2003, *Astrophys. J.*, 598, 301

Yamauchi, S., Kawada, M., Koyama, K., Kunieda, H., & Tawara, Y., 1990, *Astrophys. J.*, 365, 532

Yusef-Zadeh, F., Morris, M., & Chance, D. 1984, *Nature*, 310, 557

Yusef-Zadeh, F., Morris, M., Slee, O. B., & Nelson, G. J., 1986, *Astrophys. J.*, 300, L47

Yusef-Zadeh, F., & Morris, M., 1987, *Astrophys. J.*, 320, 545

Yusef-Zadeh, F., & Morris, M., 1987, *Astrophys. J.*, 322, 721

Yusef-Zadeh, F., & Barry, J., 1989, in IAU Symp. 136, The Center of the Galaxy, ed. M. Morris (Dordrecht: Kluwer), 197

Yusef-Zadeh, F., Wardle, M., & Parastaran, P., 1997, *Astrophys. J.*, 475, L119

Yusef-Zadeh, F., Roberts, D. A., & Biretta, J., 1998, *Astrophys. J.*, 499, L159

Yusef-Zadeh, F., Melia, F., & Wardle, M., 2000, *Science*, 287, 85

Yusef-Zadeh, F., 2003, *Astrophys. J.*, 598, 325

Acknowledgments

First, I am deeply grateful to Katsuji Koyama for his continuous guidance and encouragement throughout the five years of my graduate school period.

I also give my special thanks to Hiroshi Murakami and Aya Bamba for their continuous instruction and valuable advices. My gratitude is also for Shigeo Yamauchi, Yoshitomo Maeda, and Masaaki Sakano. Without their pioneer works, this thesis would not have been even started. I would like to express my thank to Yoshiaki Sofue and Masato Tsuboi. They provide me with radio data of the Galactic center region. I express gratitude to Ken Ebisawa for the discussion about the Galactic diffuse X-ray emission. Thanks are also due to Rhota Takahashi for the comment on the theoretical model about Sgr A^*. I wish to express my appreciation to Toru Tanimori, Shin Mineshige, Kentaro Miuchi, and Ken-ichi Imai for their careful and suggestive refereeing of this thesis. I am also grateful to Yuji Tazawa, Takeshi Tsuru, Hironori Matsumoto, Hidetoshi Kubo, Jun Kataoka, Jun Yokogawa, Kensuke Imanishi, Masahiro Tsujimoto, Akihiro Asahara, Makoto Kohno, Hideaki Katagiri, Tsutomu Nagayoshi, Shin-ichiro Takagi, Daisuke Nishida, Shio Watanabe, Hiroshi Nakajima, Atsushi Takada, Ayami Nakao, Ayako Furumori, Yuka Nakakoji, and all the members of the Cosmic-ray laboratory in Kyoto University, for their heartfelt instruction and support. I am also deeply grateful to my excellent colleagues, Masaru Ueno and Reiko Orito for their insightful comments and continuous encourgement.

This work is financially supported by Japan Society for the Promotion of Science for Young Scientists, the Hayakawa Satio Foundation of the Astronomical Society Japan, and a Grant-in-Aid for the 21st Century COE "The Center for Diversity and Universality in Physics".

Finally, I express my sincere gratitude to my family and friends, for their invisible but invaluable support.